ETP-KA/2018-17

Karlsruhe Institute of Technology

Conception and validation of test stations to electrically qualify silicon strip modules for the CMS Phase II Upgrade

Master Thesis

Roland Koppenhöfer

At the Department of Physics
Institut für Experimentelle Teilchenphysik (ETP)

Reviewer:	Prof. Dr. Ulrich Husemann
Second reviewer:	Prof. Dr. Thomas Müller
Advisor:	Dr. Alexander Dierlamm

Karlsruhe, August 6$^{\text{th}}$, 2018

This thesis has been accepted by the first reviewer of the master thesis.

Karlsruhe, August 2nd, 2018

.....

(**Prof. Dr. Ulrich Husemann**)

I declare that I have developed and written the enclosed thesis completely by myself, and have not used sources or means without declaration in the text.

Karlsruhe, August 2nd, 2018

.....

(**Roland Koppenhöfer**)

Contents

List of Figures

List of Tables

1. Introduction

To understand the composition and properties of matter in the universe, particle physicists work together in large collaborations to conduct complex experiments. One of these experiments is the currently most powerful particle accelerator in the world: the *Large Hadron Collider* (LHC) at the *European Organization for Nuclear Research* (CERN[1]) near Geneva in Switzerland. The LHC is able to accelerate protons and heavy ions in a circular storage ring in opposite directions. These particles are brought to collision within four large experiments, which are used to detect the secondary particles emerging from the interaction. Each experiment combines the information collected during the detection of those secondary particles, which allows reconstructing the nature of physical processes during the primary collision and the detection of new particles. Each of the four large detectors at the LHC is optimized to investigate a special scientific goal.

The two general purpose detectors ATLAS[2] and CMS[3] are used to test the predictions of the *Standard Model of particle physics* and to search for new physics beyond it. In 2012, these two experiments announced the discovery of the Higgs boson with a mass of 125 GeV [ATL12], [CMS12], which was until then the last undetected particle of the Standard Model. To search for new physics it is crucial to detect rare processes within the large amount of data coming from already known interactions. Therefore, the luminosity of the LHC, indicating the number of interactions per area and time, will be increased stepwise in the coming years in order to fully exploit the potential for physics discoveries. To guarantee an efficient operation of the experiments in the measurement periods at higher luminosity, the detectors need to be upgraded substantially during the coming years to withstand the higher particle rates. For the CMS and ATLAS experiments, this upgrade is referred to as Phase II Upgrade.

This thesis is written in the context of the Phase II Upgrade of the CMS Outer Tracker. Between 2024 and 2026, a new silicon tracker will be installed in the CMS experiment. The outer part of this tracker will be made of detector modules consisting of two parallel, slightly separated silicon sensors. This geometry allows on-module discrimination of bent particle tracks according to their transverse momentum, which reduces the amount of data to be read out from each tracker module. Thus, it is possible to provide track information to the *Level 1* trigger system of the CMS experiment at every bunch crossing. There will

[1] *Conseil Européen pour la Recherche Nucléaire*
[2] *A Toroidal LHC Apparatus*
[3] *Compact Muon Solenoid*

be two different types of detector modules in the CMS Outer Tracker: PS modules and 2S modules. To produce functional 2S and PS modules, the individual module components have to be tested for their quality, then assembled to 2S modules and checked for their complete functionality and finally integrated in larger structures which can be mounted in the CMS experiment. These tasks are shared among several member institutes of the CMS collaboration.

The *Institut für Experimentelle Teilchenphysik* (ETP) at the *Karlsruher Institut für Technologie* is one of the *Sensor Qualification Centers* in the CMS community and will also participate in the 2S module production. To guarantee an effective work flow and modules of the highest quality, suitable laboratory equipment needs to be developed. In the course of this thesis, two test stations have been developed to be used during the sensor qualification and module assembly process. The 2S module readout station is developed to perform functional tests with fully assembled 2S modules. Its design and performance are presented in Chapter 4 together with first functional tests using a prototype 2S module. The sensor long-term station has been designed to check the leakage current stability of 2S sensors over up to 72 hours and is presented in Chapter 5.

A short introduction to the LHC and the CMS experiment can be found in Chapter 2 including an overview of the upgrade plans for the High Luminosity LHC. Chapter 3 summarizes basics on semiconductor particle detectors and provides an overview of different interaction mechanisms of particles with matter. A detailed overview of the assembly process and the thermal concept of 2S modules can be found in Chapter 3.3.

2. The Large Hadron Collider and the Compact Muon Solenoid Experiment

Particle physicists try to understand the composition and properties of matter in the universe. To detect new particles and to investigate their properties, more and more powerful particle accelerators have been built. In this chapter the currently most powerful accelerator, the *Large Hadron Collider*, and one of its experiments, the *Compact Muon Solenoid* experiment, will be introduced.

2.1. The Large Hadron Collider

The *Large Hadron Collider* (LHC) is a particle collider for protons and heavy ions and is part of the accelerator complex at the *European Organization for Nuclear Research* (CERN[1]) near Geneva in Switzerland. It consists of a storage ring with a circumference of about 27 km in which particles travel in two beam pipes in opposite directions. It is designed to accelerate each proton beam to an energy of up to 7 TeV.

The CERN site houses several other accelerators, which are operated in an acceleration sequence before injecting the particles to the LHC storage ring. A schematic view of CERN's accelerator complex can be seen in Figure 2.1. After extracting protons from hydrogen atoms using an electric field, the *Linear Collider 2* (LINAC 2) accelerates the particles up to an energy of 50 MeV. In the *Proton Synchrotron Booster* (PSB) the energy of the protons is further increased up to 1.4 GeV before sending the beam to the *Proton Synchrotron* (PS). When the protons have reached an energy of 25 GeV, they are injected into the *Super Proton Synchrotron* (SPS), which is the last acceleration stage before the injection into the LHC ring at an energy of 450 GeV [Ben+04].

The LHC uses radiofrequency cavities to accelerate particles. In these cavities charged particles get accelerated via an oscillating electromagnetic field at a frequency of 400 MHz. Due to this acceleration principle the particles inside the storage ring are grouped into packets ("bunches") with equal energy. 1232 superconducting dipole magnets with magnetic fields of up to 8.33 T bend the particles on a nearly circular trajectory. Additional multipole magnets of higher orders form the beam profile. The radiofrequency cavities and the dipole magnets are cooled by liquid helium to 1.8 K to keep them in a superconducting state [Brü+04].

[1] *Conseil Européen pour la Recherche Nucléaire*

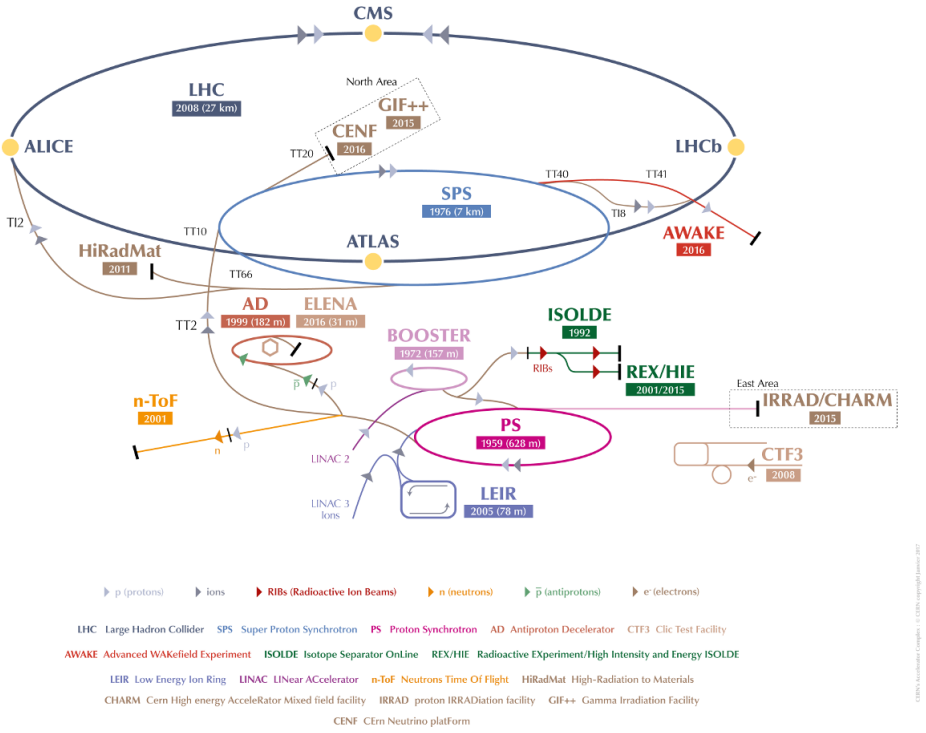

Figure 2.1.: Schematic view of the CERN accelerator complex. The acceleration chain to inject protons into the LHC consists of a linear accelerator (Linear Collider 2) and three circular accelerators (Proton Synchrotron Booster, Proton Synchrotron and Super Proton Synchrotron) [Mob16].

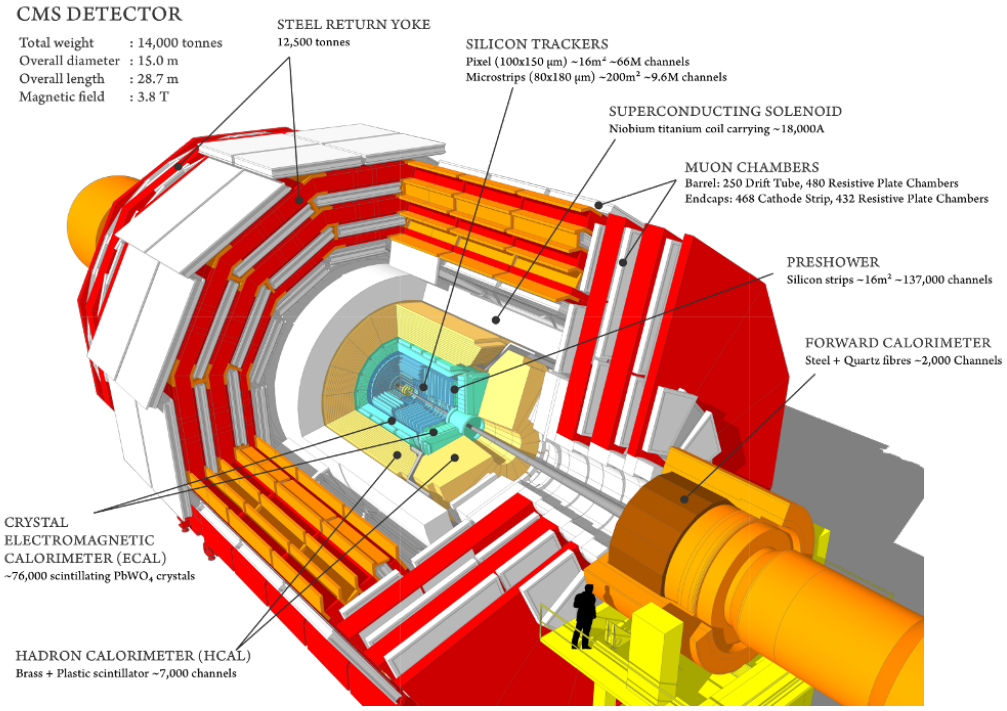

Figure 2.2.: Sectional view of the CMS experiment. The detector is arranged cylindrically around the beam pipe. The components seen from the inside are: the silicon tracker, the electromagnetic and hadronic calorimeter, the superconducting solenoid and the muon chambers embedded in the steel return yoke [Tay11].

The two beams can be brought to collision at four interaction points where the four large experiments of the LHC are located: ALICE, ATLAS, CMS and LHCb. *A Large Ion Collider Experiment* (ALICE) is designed to investigate the properties of strongly interacting matter at very high energy densities, namely the investigation of the quark-gluon plasma. *A Toroidal LHC Apparatus* (ATLAS) and the *Compact Muon Solenoid Experiment* (CMS) are two general-purpose detectors to prove predictions of the Standard Model of particle physics and to search for new physics beyond it. The *Large Hadron Collider beauty* (LHCb) experiment is specialised to study rare decays of B mesons and hence to find answers for the matter-antimatter asymmetry observable in the universe.

Besides the beam energy, a central quantity to characterize the performance of a particle collider is its luminosity $\mathcal{L}$. It is defined as the proportionality factor between the interaction rate $\dot{N}_i$ and the cross section σ_i of a certain particle interaction i

$$\dot{N}_i = \frac{\mathrm{d}N_i}{\mathrm{d}t} = \mathcal{L} \cdot \sigma_i \ . \tag{2.1}$$

Therefore, the luminosity indicates the ability of a particle collider to provide a certain number of interactions. For two colliding beams with Gaussian beam density distribution functions in the transverse plane, the luminosity can be calculated using the beam parameters by

$$\mathcal{L} = \frac{n_1 n_2 f N_b}{4\pi\sigma_x\sigma_y} \ , \tag{2.2}$$

where n_1 and n_2 are the number of particles per bunch, N_b the number of bunches, f the radial frequency and σ_x and σ_y the standard deviations of the beam profile [HM06].

The number of observable events for a process i during one measurement with duration T at a particle collider running with instantaneous luminosity $\mathcal{L}$ is

$$N_i = \sigma_i \cdot \int_0^T \mathcal{L}(t)\,\mathrm{d}t = \sigma_i \cdot \mathcal{L}_{\mathrm{int}} \ . \tag{2.3}$$

$\mathcal{L}_{\mathrm{int}}$ is called integrated luminosity and is directly proportional to N_i.

The LHC was designed to be operated at an instantaneous luminosity of $1 \times 10^{34}\,\mathrm{cm}^{-2}\mathrm{s}^{-1}$ for proton-proton collisions. By optimizing the operating parameters and installing new systems, it was possible to reach instantaneous luminosities of up to $2.06 \times 10^{34}\,\mathrm{cm}^{-2}\mathrm{s}^{-1}$ at the end of 2017, which is more than twice the design luminosity of the LHC. Throughout 2017, ATLAS and CMS registered more than $50\,\mathrm{fb}^{-1}$ of data [Pra17].

2.2. The Compact Muon Solenoid Experiment

The *Compact Muon Solenoid* (CMS) experiment is a general-purpose particle detector at the Large Hadron Collider. With a diameter of 15 meters and a length of 29 meters, it is the second largest experiment at the Large Hadron Collider, but its weight of approximately 14 000 tonnes makes it the heaviest.

Figure 2.2 shows a sectional view of the experiment. The different subdetectors are arranged in concentric layers around the beam pipe. The innermost layers are part of the silicon tracker, which measures the trajectories of charged particles passing the detectors. The following electromagnetic calorimeter is optimized to measure the energy of electromagnetically interacting particles like electrons and photons. The energy of strongly interacting particles is measured in the hadronic calorimeter. All these detectors lie inside a superconducting solenoid, which creates a 3.8 T strong magnetic field to bend the

trajectories of charged particles. The magnetic field lines are closed outside the solenoid using an iron yoke, which is equipped with muon detectors to identify the trajectories of muons coming from the interaction point [CMS08].

The information of all detector layers together allows the reconstruction of the particle properties and the identification of the original interaction in the beam pipe.

2.2.1. Silicon Tracker

The silicon tracker is used to precisely reconstruct the trajectories of charged particles coming from the interaction point and to identify secondary vertices. At the design luminosity of $1 \times 10^{34}\,\mathrm{cm}^{-2}\mathrm{s}^{-1}$, about 1000 particles originating from more than 20 proton-proton interactions pass the tracker at each bunch crossing. Therefore, it is crucial for the performance of the whole experiment to provide a fast and highly granular detector technology to correctly identify the particle tracks and to keep the occupancy small. Hence, the silicon tracker is instrumented with two different types of detectors: the innermost layers are made of silicon pixel detectors while the outer layers are equipped with silicon strip detectors. With this geometry, the tracker achieves a spatial resolution of 10 µm for tracks with high transverse momentum. At lower momenta, the resolution degrades due to multiple-scattering effects [CMS08].

Until the end of 2016, the barrel pixel detector consisted of three layers of hybrid pixel detector modules. Due to the high particle flows near the interaction point the pixel detector was exchanged during the CMS Phase I Upgrade at the end of 2016 to guarantee efficient tracking in the future. An additional fourth layer was introduced to the barrel pixel detector while the innermost layer was shifted nearer to the interaction point [Dom+12].

The silicon strip tracker covers the radii between 20 cm and 116 cm. As shown in Figure 2.3, it can be divided in four areas. The Tracker Inner Barrel and Disks (TIB/TID) consist of four barrel layers and three disk layers. Silicon micro-strip sensors with a pitch between 80 µm and 141 µm are used, which achieve a single point resolution between 23 µm and 35 µm. The Tracker Outer Barrel (TOB) surrounds the TIB/TID, which provides six additional layers with silicon sensor modules. Finally, the Tracker Endcaps (TEC) made of nine disks are used to cover the forward region [CMS08].

As silicon strip detectors can only provide limited three-dimensional resolution compared to silicon pixel detectors, the modules in the layers nearest to the interaction point in all silicon strip tracker subregions are equipped with a second micro-strip detector mounted back-to-back and slightly rotated to the top sensor. This 100 mrad stereo angle allows to achieve an improved three-dimensional resolution by combining the signals of the two sensors. In Figure 2.3, the layers using this double-sided modules are marked in blue.

Up to 2016, the silicon tracker was operated at a cooling plant set temperature of 4°C. After several improvements to reduce the dew point level during the shutdown of the LHC at the end of 2016, it is since possible to operate the silicon strip detector at a set temperature of −15°C [Vor15].

2.2.2. Calorimeters

After the particles have passed the silicon tracker, they reach the electromagnetic calorimeter. Calorimeters are used to determine the particles' energies by transforming the energy into a measurable quantity by stopping the particle in the calorimeter material. In several subsequent interaction steps, the primary particle produces secondary particles and transfers parts of its energy to those.

The electromagnetic calorimeter serves to measure the energy of electrons, positrons and photons. It is made of 61 200 lead tungstate ($PbWO_4$) crystals in the central part and

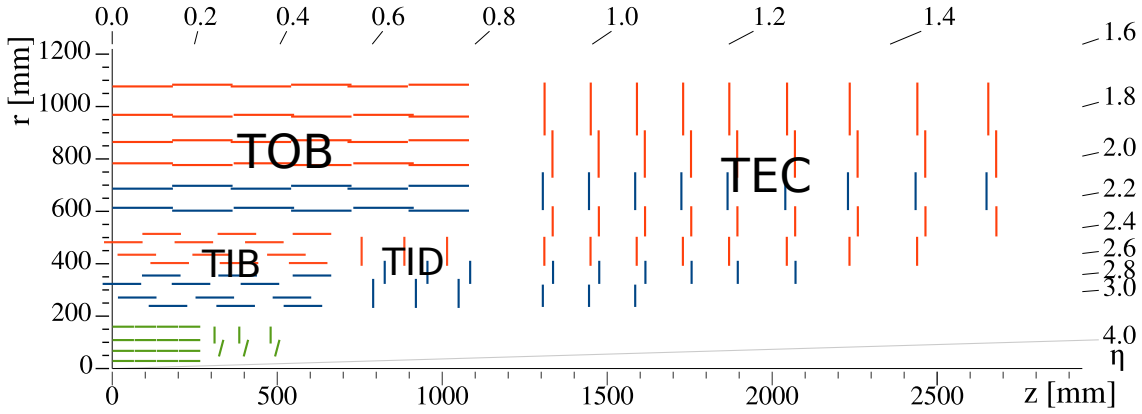

Figure 2.3.: Sketch of one quarter of the CMS Phase I tracker. Silicon pixel modules are marked in green, single-sided strip modules in red and double-sided strip modules in blue [CMS17].

7324 crystals in each of the endcaps, which act as absorber material and fast scintillators to measure the energy deposition. This material provides a short radiation length of approximately 1 cm and a small Molière radius of approximately 2 cm, which allows to build a compact calorimeter in which the particle shower of high energetic primary particles can be completely recorded. The electromagnetic calorimeter provides a depth of 26 radiation lengths to minimize the loss of particles and, therefore, energy deposition. Each crystal has a front surface of about $22 \times 22\,\mathrm{mm}^2$ which corresponds to the Molière radius and gives the calorimeter a high granularity. The scintillation light is read out via silicon avalanche photodiodes in the barrel part and via vacuum phototriodes in the endcaps [CMS97a].

The hadronic calorimeter encloses the electromagnetic calorimeter and measures the energy of strongly interacting particles. It is built of alternating layers of dense absorber material (brass and steel) and 4 mm thick plastic scintillator tiles as active material to detect the hadronic particle shower. After shifting the wavelength of the scintillation light using a thin fiber inside each plastic scintillator tile, light is collected and guided via optical cables to hybrid photodiodes [CMS97b].

2.2.3. Superconducting Solenoid

The tracker and calorimeter systems are surrounded by a superconducting solenoid made of niobium-titanium (NbTi). The solenoid produces a 3.8 T strong homogeneous magnetic field which is orientated parallel to the beam axis. Providing a homogeneous and strong magnetic field is essential to precisely determine momenta and signs of charged particles using the curvature of their trajectories caused by the Lorentz force. The solenoid is 13 m long, has an inner diameter of 5.9 m and stores an energy of 2.6 GJ at full current. It is operated at 4.5 K using a liquid helium based cooling. The magnetic field lines are closed outside the solenoid using an iron yoke in which muon detectors are embedded [CMS08].

2.2.4. Muon System

Muons are detected outside the superconducting solenoid by four detector layers within the iron yoke. Three different types of muon detectors are used: 250 drift tubes, 540 cathode strip chambers and 610 resistive plate chambers. The muon system is able to provide robust and fast muon trigger information with an efficient background suppression by using coincidences between the different types of detector concepts. By measuring the muon trajectory at four vertex points, it is possible to reach a high transverse momentum resolution. The muon momentum resolution of the muon system itself is about 9% for

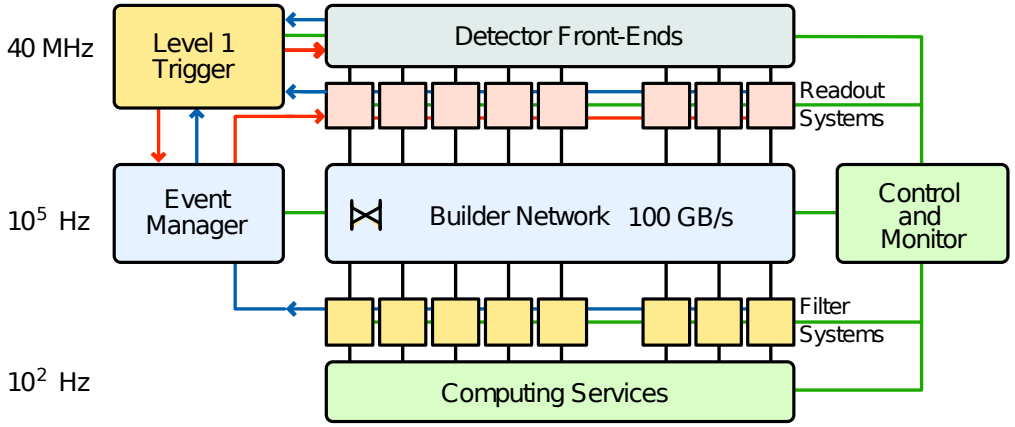

Figure 2.4.: Schematic of the CMS data acquisition system architecture. The Level 1 Trigger reduces the readout rate from the detector front-ends to 100 kHz. In a second trigger stage, the software-based High-Level Trigger processes the data of all detector systems and filters interesting events [CMS08].

transverse momenta up to 200 GeV, and between 14% and 50% at 1 TeV depending on the muon trajectory [CMS08].

2.2.5. Trigger and Data Acquisition

When the LHC is operated with proton bunches at its design luminosity of $1 \times 10^{34}\,\mathrm{cm^{-2}s^{-1}}$ and a beam cross frequency of 40 MHz, there are approximately 20 simultaneous collisions every 25 ns. To reduce the readout rate, the CMS experiment uses two trigger stages. Acquired data of each bunch crossing is stored in the detector front-end electronics and is only read out if the first trigger stage, the Level 1 (L1) Trigger, indicates it. The L1 Trigger is based on mainly programmable electronics and uses data from the calorimeters and the muon system to achieve an output rate of 100 kHz at maximum.

Data read out after the L1 Trigger signal is sent to the data acquisition system, which processes it in a second trigger stage. This second stage is the software-based High-Level Trigger (HLT). Based on data of all detector systems, the HLT can perform more complex calculations. The two trigger stages together achieve a reduction of the data rate in the order 10^6 at minimum. Figure 2.4 shows a schematic of the architecture of the CMS data acquisition system with the two trigger stages [CMS08].

2.3. Upgrade plans for the LHC and the CMS Experiment

The LHC is currently the most powerful particle accelerator in the world. In order to fully exploit its physics discovery potential, it is planned to upgrade the accelerator and its experiments in the 2020s to prepare them for the following measurement period with increased luminosity. In Chapter 2.3.1 the High Luminosity LHC will be introduced. Chapter 2.3.2 will discuss the measures to prepare the CMS Outer Tracker for the high luminosity phase.

2.3.1. The High Luminosity LHC

During the operation of the Large Hadron Collider in 2017, it was possible to deliver an instantaneous luminosity of more than twice the nominal design value to the experiments. It is planned to further increase the luminosity over the next years to ensure scientific progress in the search for new physics and to perform precision measurements. A higher

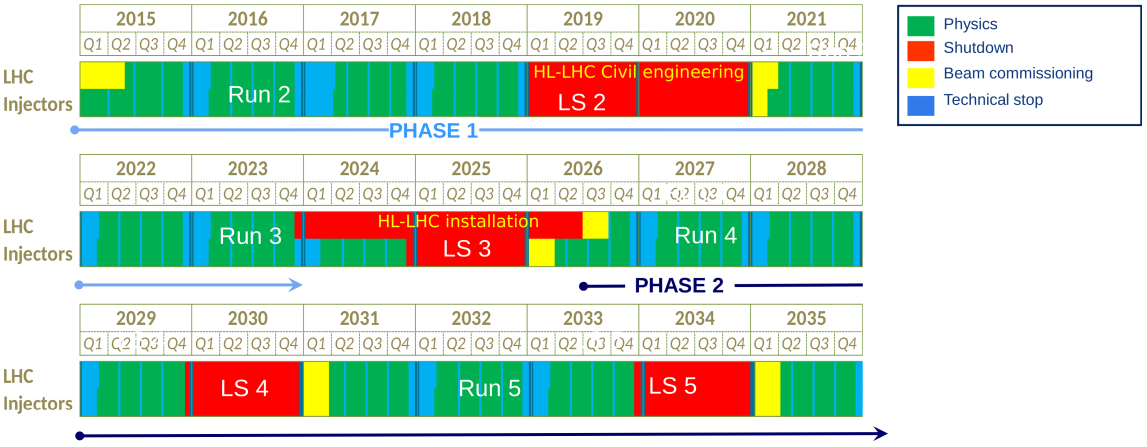

Figure 2.5.: Schedule for the LHC measurement (green) and upgrade program. During the shutdowns (red) new detector systems can be installed in the LHC experiments in order to prepare the experiments for the High Luminosity LHC [CMS17].

luminosity leads to higher particle rates and, therefore, the detector systems have to endure higher radiation levels. To guarantee efficient operation of the accelerator, upgrades for several systems of the machine and the experiments are needed. Figure 2.5 shows an overview of the planned measurement runs and the upgrade work during the shutdown phases of the LHC. The installation of the new systems will mainly be done during *Long Shutdown 3* from 2024 to 2025, some preparations will already be performed during *Long Shutdown 2* from 2019 to 2020. From 2026 on the accelerator will enter the measurement program referred to as High Luminosity LHC.

The inner triplet quadrupole magnets will be replaced by magnets made from niobium-tin (Nb_3Sn), which are less prone to radiation damage. These magnets can provide a higher magnetic field and, therefore, allow further focusing of the beams at the interaction point. Additional to the magnet system, specially developed superconducting radiofrequency cavities will form the beam profile at the interaction point to gain luminosity. A new cryogenic plant will allow the cooling of the radiofrequency cavities and the magnets with separate cooling circuits [Apo+15].

Regarding the detector systems in the experiments at the LHC, it is important that all parts can be operated efficiently in the higher radiation environment. Besides the luminosity also the number of interactions per bunch crossing, which are called pileup events, will increase substantially to up to 200 for the highest luminosity of $7.5 \times 10^{34}\,\mathrm{cm}^{-2}\mathrm{s}^{-1}$. Hence, the experiments need to provide a higher granularity to reduce occupancy, provide a high bandwidth for data readout and an improved trigger capability.

2.3.2. The CMS Phase II Outer Tracker Upgrade

In preparation for the High Luminosity LHC, several detector systems of the CMS experiment have to be improved or exchanged. This upgrade is called CMS Phase II Upgrade. The whole CMS tracker will be exchanged during *Long Shutdown 3*. The new tracker will be made of silicon pixel modules for the Inner Tracker and modules using silicon strip and macro-pixel sensors in the Outer Tracker. Figure 2.6 shows a sketch of one quarter of the upgraded tracker where the positions of the different modules are marked. The Outer Tracker will be composed of six cylindrical layers in the central region and five double-discs in the endcap region.

In the Outer Tracker there will be two different types of detector modules: PS-modules will be installed in the layers nearer to the beam pipe and 2S-modules in the outer re-

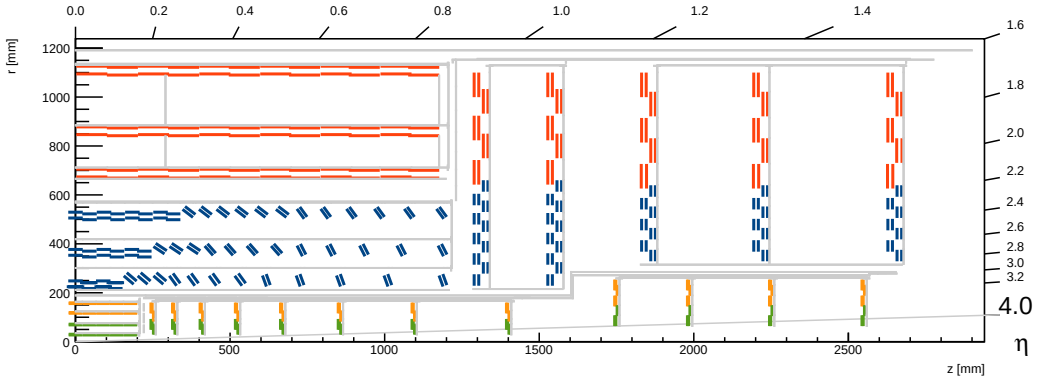

Figure 2.6.: Schematic view of one quarter of the CMS tracker after the Phase II Upgrade. The Inner Tracker with its silicon pixel modules is marked in green and orange, the two types of modules in the Outer Tracker are marked in blue (PS-modules) and red (2S-modules) [CMS17].

gions. Their design was mainly driven by the need to provide tracking information to the *Level 1* (L1) trigger. This additional information will improve the transverse momentum resolution and will help to better separate tracks in a high pileup environment at this first trigger stage. Therefore, the modules have to be able to send out self-selected information at every bunch crossing. Each of these modules are made of two single-sided silicon sensors, which are mounted in parallel, separated from each other by a small gap. The two sensors are read out by the same set of chips. Therefore, these chips can correlate hits in the two silicon sensors for each event and measure the spatial displacement between the hits. As the trajectory of charged particles is bent by the 3.8 T strong magnetic field, a particle with high momentum produces two hits with a small lateral displacement in the sensors. This principle is illustrated in Figure 2.7. For lower momenta the curvature of the particle's trajectory is larger and the hit positions in the sensors show a higher spatial displacement. Hits with a displacement smaller than a specific readout window are called *stub* and declared as an interesting event for the trigger level. By adapting the size of the acceptance window, these modules can discriminate between different transverse momenta, which is used to select particles with transverse momenta higher than 2 GeV/c. The stub information is sent to the L1 tracking system to reconstruct tracks which provides a fast trigger information [CMS17].

During the Phase II Upgrade the cooling system will be updated as well. A two-phase CO_2 cooling system will be used to operate at a nominal set point temperature of $-35°C$. Thermal studies have been performed to show that with this configuration it will be possible to operate the silicon sensors in the Outer Tracker at approximately $-20°C$ or lower [CMS17].

Additional information about the geometry, the assembly process and the thermal behavior of 2S modules can be found in Chapter 3.

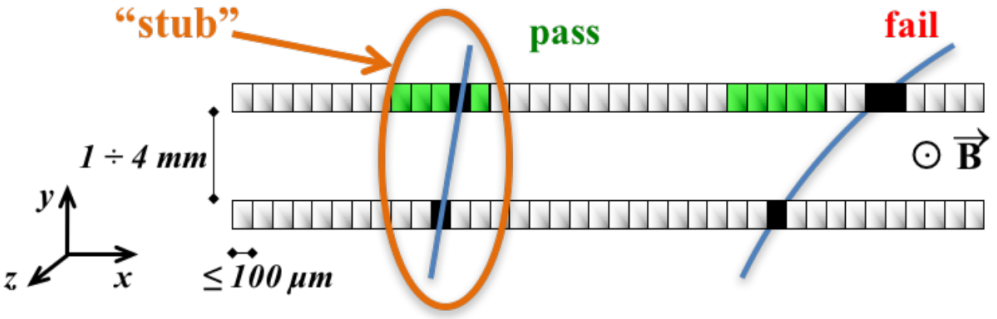

Figure 2.7.: Functional principle of the transverse momentum discrimination of the silicon sensor modules used in the CMS Outer Tracker. Only particles with a high transverse momentum have a small curvature of their trajectories in the magnetic field and thus show hits with small spatial displacement in the two parallel sensor layers of one module. By changing the size of the acceptance window (green) for this displacement, the modules can discriminate between different transverse momenta [CMS17].

3. 2S Modules for the CMS Outer Tracker

In order to build specialized and optimized tracking detectors, it is important to understand the physical properties of the detector material and the interaction mechanisms of particles with matter. The basics of semiconductor particle detectors will be introduced in Chapter 3.1 following [GM12]. Chapter 3.2 briefly discusses the major interaction processes of charged and neutral particles with matter. In Chapter 3.3 the assembly procedure and thermal behavior of 2S modules will be presented.

3.1. Basics of Semiconductor Particle Detectors

The atomic structure of semiconductors is characterized by an ordered arrangement of atoms in a crystalline lattice. To describe the electronic energy levels in solids with crystalline lattice, solid-state physics uses the energy band model. The energy levels of an electron in an isolated atom are discrete. In a solid-state, the atomic orbitals of neighboured atoms in the lattice overlap. This leads to a splitting of atomic orbitals into many discrete molecular orbitals where the discrete energy levels become quasi-continuous multiplets with nearly the same energy. Every energy band has a finite width depending on the amount of overlap between neighboured orbitals. Two energy bands are separated by a gap, which corresponds to an energy range where no electronic levels are existent.

As electrons are fermions, they obey the Pauli exclusion principle. Therefore, the filling scheme for the energy bands follows the Fermi-Dirac distribution. For $T = 0\,\mathrm{K}$ the electrons of a solid state fill up all energy levels below the Fermi energy E_F. The highest fully occupied band is called valence band. The next higher energy band is the conduction band. Depending on the position of the Fermi level with respect to the band gap between conduction and valence band, solid-states can be classified as conductors, semiconductors and insulators. For insulators and semiconductors the Fermi level lies inside the energy gap. In contrast to insulators the energy gap of semiconductors is small enough to allow electron transitions from the valence to the conduction band through thermal excitation at room temperature. This leads to a small electrical conductivity of semiconductors. For metals the Fermi level is situated inside an energy band.

3.1.1. Doping of Semiconductors and pn-Junction

To improve the electrical conductivity of intrinsic semiconductors, atoms of other elements can be introduced to the lattice. This process is called doping and there are two different

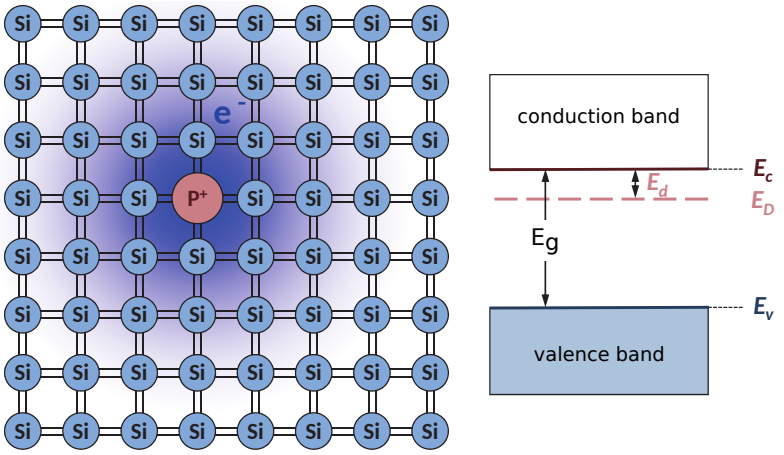

Figure 3.1.: Illustration of a n-doped silicon lattice with a phosphorus atom. Phosphorus provides one valence electron more than silicon. This electron is weakly bound and can easily travel through the lattice, thereby improving the electrical conductivity of the semiconductor. In the band model an additional donor energy level is created in the band gap below the conduction band [GM12].

types of doping which are called n-doping and p-doping.

For n-doping, atoms with a higher number of valence electrons than the intrinsic semiconductor are inserted into the lattice. These impurities are called donors because additional electrons with a small binding energy are added to the crystal, as these electrons do not contribute to the covalent bonds in the lattice. This leads to an additional energy level below the conduction band, which enhances the electrical conductivity at room temperature. Figure 3.1 illustrates n-doping of silicon with phosphorus and the effect on the band structure. Other donors for silicon are e.g. arsenic or antimony.

By inserting atoms with a lower number of valence electrons to a semiconductor, p-doping is achieved. As in this case the impurities provide fewer valence electrons to be used in the covalent bonds a so-called hole is produced in the lattice. The impurities are called acceptors because they can easily bind an electron from their neighbours and, thus, the holes can move nearly freely through the lattice. In the band model a new energy level is created above the valence band and the electrical conductivity improves. Acceptors for silicon are e.g. boron or gallium.

By combining p- and n-doped areas in a semiconductor crystal, a p-n junction forms at the contact area. The existent gradient in charge carrier concentration between p- and n-doped area leads to a diffusion of electrons from the n-doped to the p-doped side where they recombine with holes. Holes from the p-doped side diffuse in the opposite direction and recombine with electrons in the n-doped area. Thereby, an electric field is created which opposes the diffusion and leads to an equilibrium state. Thus, a depletion zone with a largely reduced number of free charge carriers develops in the interface region.

A semiconductor diode consists of a p-n junction. Applying an external voltage with positive pole at the n-doped side of a p-n junction leads to an increase of the depletion zone, as more charge carriers are withdrawn from the interface layer. Only a small temperature dependent current can be measured, the diode is operated in reverse bias mode. With opposite polarity the external power supply introduces electrons at the n-doped side and holes at the p-doped side and the depletion zone shrinks. In this case, the current can flow easily through the p-n junction and the diode is operated in forward bias mode.

The design and operation of semiconductor particle detectors are based on the working

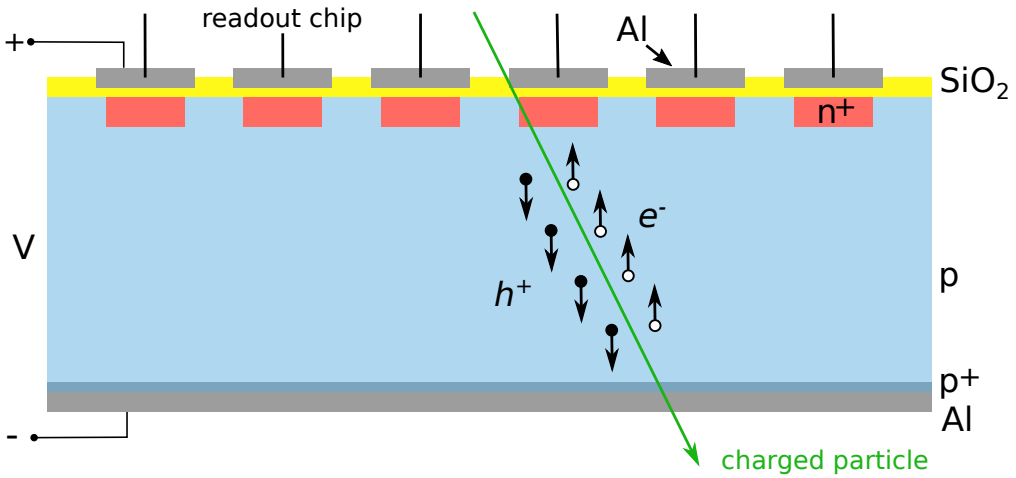

Figure 3.2.: Schematic of the geometry of a p-type and AC-coupled silicon strip sensor. A crossing particle creates electron-hole pairs in the p-doped bulk. Electrons are collected at the strongly n-doped implants which are coupled via silicon dioxide capacitively to aluminum readout strips. Holes drift to the sensor back side where a strongly p-doped silicon layer and an aluminum layer provide the negative bias potential [Dro18].

principle of p-n junctions. The next chapter presents the geometry and functionality of silicon strip detectors.

3.1.2. Silicon Strip Detectors

The basic working principle of silicon sensors is operating several parallelly arranged p-n junctions in reverse bias mode. A schematic of the geometry of a silicon detector is shown in Figure 3.2 for a p-type and AC-coupled silicon strip sensor. The sensor mainly consists of p-doped silicon called bulk. The bottom side of this p-doped bulk is covered by a thin, strongly p-doped area (typically a few hundreds of nanometers) and an aluminum layer to which the contacts for the negative pole of the biasing voltage get attached. At the top side of the bulk, strongly n-doped implants are arranged in parallel strips. To electrically insulate the n-doped implants from the parallel aligned aluminum readout strips, a silicon dioxide layer separates the strips and implants, which enables an AC-coupled readout, see e.g. [Har17].

The p-n junction between implants and bulk is operated in reverse bias mode and the depletion region enlarges with increasing voltage in the bulk volume. Silicon sensors are mainly operated with fully depleted bulk, minimizing the number of free charge carriers due to thermal excitation in the sensor volume and allowing the detection of additional electron hole-pairs created when a particle crosses the sensor. Further details concerning the different interaction mechanisms of particles with matter can be found in Chapter 3.2.

For a p-type sensor, the electrons drift to the implants following the electric field and the holes are collected at the sensor back side. By connecting the aluminum strips to a readout chip, the induced signal in the sensor can be read out.

3.2. Interaction of Particles with Matter

In order to detect particles, they have to interact with the sensor material. As the interaction mechanisms depend on many particle properties like charge, energy and momentum, it is crucial to understand all parameters in order to optimize technologies for specific

detector systems. The interaction mechanisms for charged and neutral particles will be discussed separately.

3.2.1. Charged Particles

The interaction mechanisms for heavy charged particles and light charged particles differ substantially.

Electromagnetic interactions of **heavy charged particles** are dominated by single collisions leading to ionization, atomic or collective excitation. The mean energy loss per unit length can be described by the *Bethe equation*

$$-\left\langle \frac{\mathrm{d}E}{\mathrm{d}x} \right\rangle = 4\pi N_A r_e^2 m_e^2 c^2 z^2 \frac{Z}{A}\frac{1}{\beta^2}\left[\frac{1}{2}\ln\left(\frac{2m_e c^2\beta^2\gamma^2 T_{\max}}{I^2}\right) - \beta^2 - \frac{\delta(\beta\gamma)}{2}\right] , \qquad (3.1)$$

which is valid for the energy range $0.1 \lesssim \beta\gamma \lesssim 1000$. Therefore, the energy loss depends on the properties of the incoming particle as well as the properties of the absorber material. The variables used in Equation 3.1 are the Avogadro constant N_A, the classical electron radius r_e, the electron mass m_e, the speed of light c, the charge number of the incident particle z, the atomic number and atomic mass of the absorber Z and A, respectively, the Jackson number β, the Lorentz factor γ, the maximum energy transfer to a shell electron in a single collision $T_{\max}$, the mean excitation energy of the absorber material I and the density effect correction $\delta(\beta\gamma)$. The mean energy loss minimizes for particles with $\beta\gamma \approx 3$, which are called *minimum ionizing particles* (MIPs). As the mean energy loss of MIPs is minimal, they are able to deeply penetrate matter. Further information about the Bethe equation can be found e.g. in [Tan+18].

Figure 3.3 illustrates the mean energy loss of muons in copper depending on their energy. To describe the mean energy loss of particles with $\beta\gamma \lesssim 0.1$, nuclear effects have to be taken into account and for $\beta\gamma \gtrsim 1000$ radiation effects dominate the energy loss.

For **light charged particles** like electrons the Bethe equation is not valid. For energies below approximatley 10 MeV electrons mainly lose their energy via ionization. Scattering effects like Møller (electron-electron) or Bhabha (electron-positron) scattering and positron annihilation are less important. With increasing energy the influence of the electromagnetic field of the nuclei on the incident particle gets larger and, thus, the energy losses through bremsstrahlung increase. For each material, a critical energy can be defined at which the loss rates of ionization processes and bremsstrahlung are equal, typically a few tens of MeV [Tan+18].

3.2.2. Neutral Particles

To detect neutral particles, they have to interact with the detector material to generate charged particles, which can then be measured via the interaction mechanisms presented in the last chapter. In this chapter, only interaction mechanisms of photons will be discussed. Detailed information about interaction processes of other neutral particles like e.g. neutrons can be found in [LR12].

There are three main interaction processes for photon interactions with matter. For energies below 10 keV the photoelectric effect dominates the total cross section. During this process a photon is absorbed in the interaction and transfers its total energy to a shell electron which gets emitted. At intermediate energies the Compton effect dominates the total cross section. Photons get scattered inelastically at electrons of the target material by transferring parts of their energy to the electron. If the photon energy exceeds twice the rest mass energy of an electron, it is energetically possible to create an positron-electron pair in the Coulomb field of a nucleus. Thus, for photon energies larger than 1.022 MeV, pair production is the dominant interaction process.

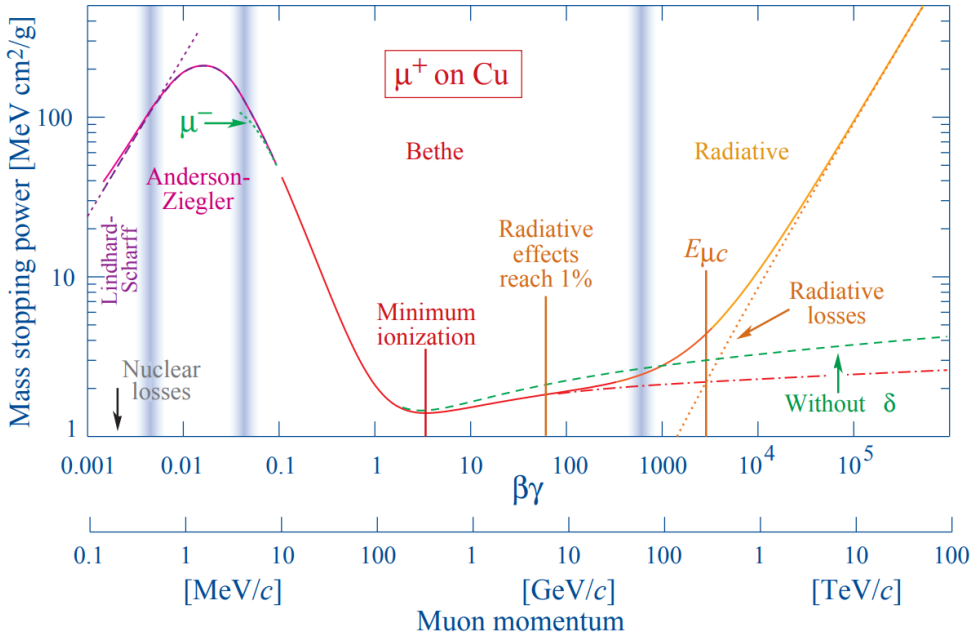

Figure 3.3.: Mean energy loss per unit length of heavy charged particles during interaction with matter. For $0.1 \lesssim \beta\gamma \lesssim 1000$ the Bethe equation is valid. At lower energies nuclear reactions get more important while for higher energies radiative effects dominate [Tan+18].

3.3. 2S Modules for the CMS Outer Tracker

The Outer Tracker of the CMS Experiment will be equipped with 2S and PS modules in order to prepare the experiment for the High Luminosity LHC. Figure 3.4a illustrates the components a 2S module is built of. The two silicon strip sensors of each module have two rows of 1016 strips each. The strips have an approximate length of 5 cm and a pitch of 90 µm. During the assembly of a 2S module, two sensors are glued back to back onto spacers made of aluminum/carbon fiber composite (Al-CF) with a thickness of 1.8 mm or 4 mm. Besides the spacing of the two sensors, these spacers allow the fixation of the module on supporting structures and act as the main cooling path for the entire module. The coefficient of thermal expansion (CTE) of Al-CF is 4 ppm/°C which matches well the CTE of silicon of 3 ppm/°C and, thus, minimizes the thermal stress inside the module [CMS17].

The strips of the silicon sensors are read out by 16 *CMS Binary Chips* (CBCs) mounted on the two front-end hybrids on two sides of the sensor. Each CBC reads out corresponding strips from the lower and the upper sensor to enable fast transverse momentum discrimination. A *Concentrator Integrated Circuit* (CIC) combines and serializes the data of the eight CBCs on each front-end hybrid and distributes clock, trigger and control signals. One service hybrid per module houses auxiliary electronics for powering and optical communication [CMS17].

3.3.1. Assembly Procedure

In total, there will be 7680 2S modules installed in the CMS Outer Tracker after the Phase II Upgrade. The production of these modules is shared among the institutes of the CMS community. The *Institut für Experimentelle Teilchenphysik* (ETP) at the *Karlsruher Institut für Technologie* is one of the 2S modules production centers and will build around 2000 modules until 2023. Figure 3.4b depicts a schematic of the assembly steps during the module production.

To continuously guarantee a good quality and functionality of the silicon sensors, five percent of all sensors used in the module production are tested as a first step in the production flow. Afterwards, the edge quality and dimensions of all sensors are checked to ensure that a well aligned module can be built. Then, three electrically insulating strips and the high voltage tails are glued onto the backplane of each sensor and an electrical connection between the tails and the sensor will be added using wire bonds. To protect the wires from mechanical damage during the further steps, they are encapsulated and the electrical contact between sensor backplane and high voltage tails is checked.

As a next step, the sensors are glued at the polyimide strips onto the aluminum/carbon fiber spacers and the result is inspected optically. The strip to strip alignment is measured with a specially designed metrology station. Afterwards, the two front-end hybrids and the service hybrid are glued to the sensors. The silicon strips are connected via wire bonds to the front-end hybrids. Before the wire bonds are encapsulated, a functional test of the entire module is performed. This test is repeated after the encapsulation procedure to ensure an immaculately assembled and fully functional module.

The two functional test steps for each assembled modules are a crucial check to reliably ensure the best possible quality of 2S modules during the whole production phase. In the course of this thesis, a concept for a test station has been developed in order to perform these functional tests under defined and reproducible conditions. The concept will be presented in Chapter 4.

3.3.2. Thermal Performance

The CMS cooling system for the High Luminosity LHC phase is designed to operate at a nominal coolant temperature of $-35°C$ with a two-phase CO_2 coolant. The coolant will be distributed in the tracking volume via cooling pipes onto which the module support structures are mounted. It is estimated that the cooling system has to remove a heat load of approximately 100 kW for the Outer Tracker. This leads to a temperature increase along the cooling circuit resulting in a maximum coolant temperature of $-33°C$ [CMS17].

Thermal simulations of a 2S module have been performed based on finite element analyses using the software framework ANSYS [ANS17]. Information about finite element analysis and the framework can be found in Chapter 4.2.1. For the simulations, a simplified geometry of the modules was used, in which features irrelevant for the thermal performance were removed. Figure 3.5a illustrates the geometry. It was estimated that the readout and auxiliary electronics introduce a heat load of approximately 5.4 W to a 2S module in operation.

When silicon sensors are irradiated, the incident particles can interact with the atomic bodies in the semiconductor lattice and, thereby, deform the lattice. This effect is called radiation damage and it leads macroscopically besides others to an increase of the leakage current in a silicon sensor. Thus, the thermal heat load of an irradiated silicon sensor scales with its irradiation level. At room temperature, the thermal heat load of an irradiated silicon sensor is given by

$$p^{RT} = \alpha \cdot \Phi \cdot V \cdot U \ , \tag{3.2}$$

where α is the damage constant, Φ the irradiation fluence in 1 MeV neutron equivalent/cm^2, V the active sensor volume and U the bias voltage [CMS17]. Equation 3.2 is used to calculate the expected heat loads of the two sensors in a 2S module.

During the operation of a 1.8 mm 2S module in the CMS experiment, it is expected to accumulate a fluence of $\Phi = 2.3 \times 10^{14}\,\mathrm{n_{eq}/cm^2}$. In order to realistically describe the leakage current rise through radiation damage for strip sensors at this fluence, a value of

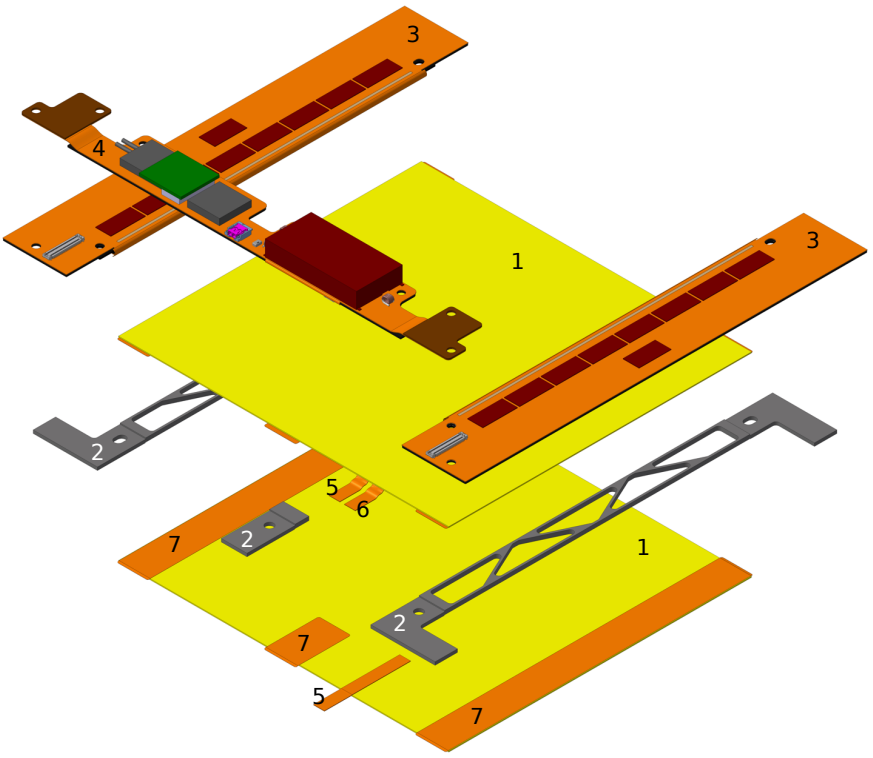

(a)

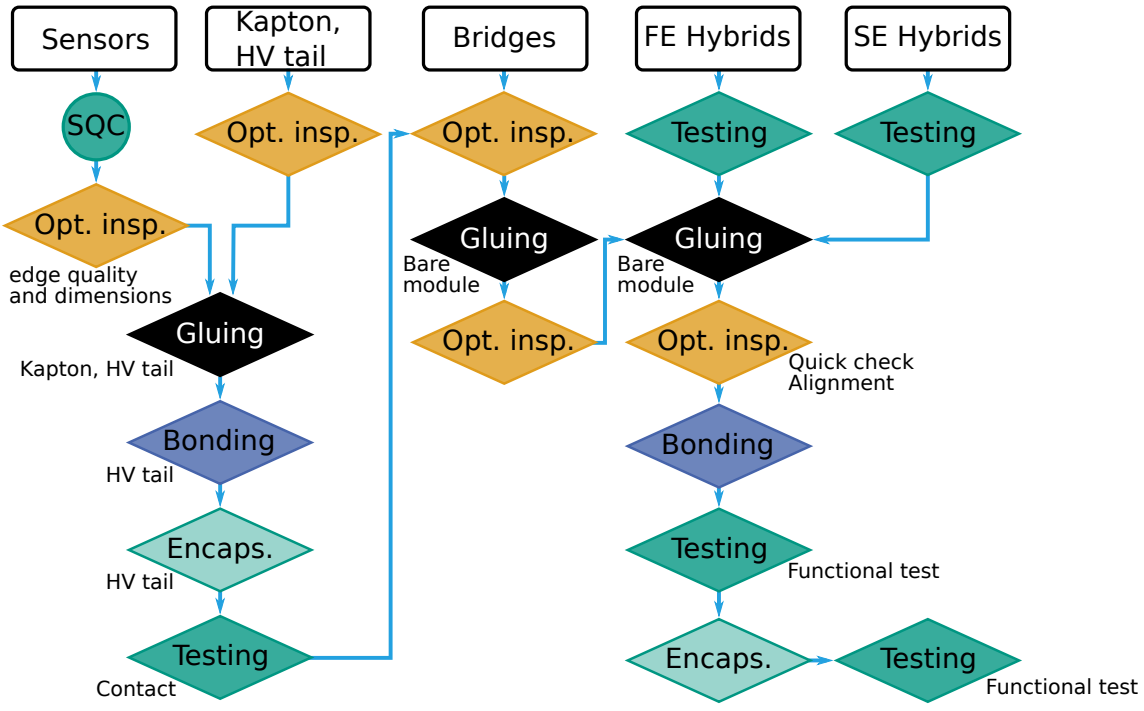

(b)

Figure 3.4.: Overview of the single components (a) and the production flow (b) of a 2S module. The module production centers in the CMS community will assemble the modules from the single components. The components are: two silicon strip sensors (1), aluminum/carbon fiber spacers (2), two front-end hybrids (3), one service hybrid (4), high voltage tails (5), a temperature sensor (6) and strips for electrical isolation (7) [CMS17].

$5.35 \times 10^{-17}\,\mathrm{Acm}^{-1}$ is assumed for the damage constant α [CMS17]. A 2S silicon sensor has an approximate active area of $90\,\mathrm{cm}^2$ and an active thickness of $200\,\mu\mathrm{m}$. Together with a maximum operating voltage of 800 V this leads to a heat load of approximate 18 W at room temperature. According to [Chi13] the current, and therefore the heat load of a silicon sensor, scales with temperature as

$$P(T) \propto I(T) \propto T^2 \cdot \mathrm{e}^{-1.21\,\mathrm{eV}/(2k_\mathrm{B}T)} \ . \tag{3.3}$$

Hence, the heat load of a 2S sensor at $-20°\mathrm{C}$ is approximately 0.3 W [CMS17].

In summary, the thermal heat load of a 1.8 mm 2S module after 10 years of nominal operation in the High Luminosity LHC is approximately 6 W. This value was inserted to the thermal simulations and studies at different temperatures of the coolant were performed. Figure 3.5b summarizes the dependence of the temperature difference between the maximum temperature of the sensors and the temperature of the CO_2 cooling system on the coolant set temperature. The more the coolant temperature rises, the larger the temperature difference between sensors and cooling structures gets. A quantity to characterize the thermal performance of a 2S module and its cooling structure is the temperature at which the cooling power is not any more sufficient to stabilize the sensor temperature. As the leakage current rises exponentially with temperature, the module enters a positive feedback loop and the sensor temperature increases substantially. This effect is called thermal runaway and is dependent on the irradiation level and the bias voltage. In order to guarantee stable detector operation, it is important to design the cooling system correctly to stabilize the temperature well below the thermal runaway temperature.

In the current design of the CMS cooling system, the coolant temperature is approximately $-33°\mathrm{C}$ for the warmest module in the cooling circuit. The simulations show that at this point (dashed line in Figure 3.5b) the modules can be operated at a stable temperature level below the thermal runaway temperature [CMS17].

3.3.3. The CMS Binary Chip

The 16 *CMS Binary Chips* (CBCs) per 2S module correlate the information of the two parallel silicon sensors in a 2S module. Each CBC provides 254 readout channels which are connected alternating to bottom and top sensor. Even channels read out the strips of the bottom sensor and odd numbers the ones of the top sensor. With this configuration, it is possible to correlate hits in both layers and measure the spatial displacement between the hits and detect stubs, as mentioned in Chapter 2.3.2. Adjacent CBCs on a front-end hybrid are connected with each other to find stubs shared between them.

Figure 3.6 illustrates the signal processing in the analog front-end for a CBC of the second iteration. The charge generated in a strip is amplified in three stages by a preamplifier, a gain amplifier and a postamplifier. To level the amplifications of different channels, the parameters V_Plus and V_dda can be modified for each channel. The amplified signal is compared with the global threshold V_CTH and a digital output is created.

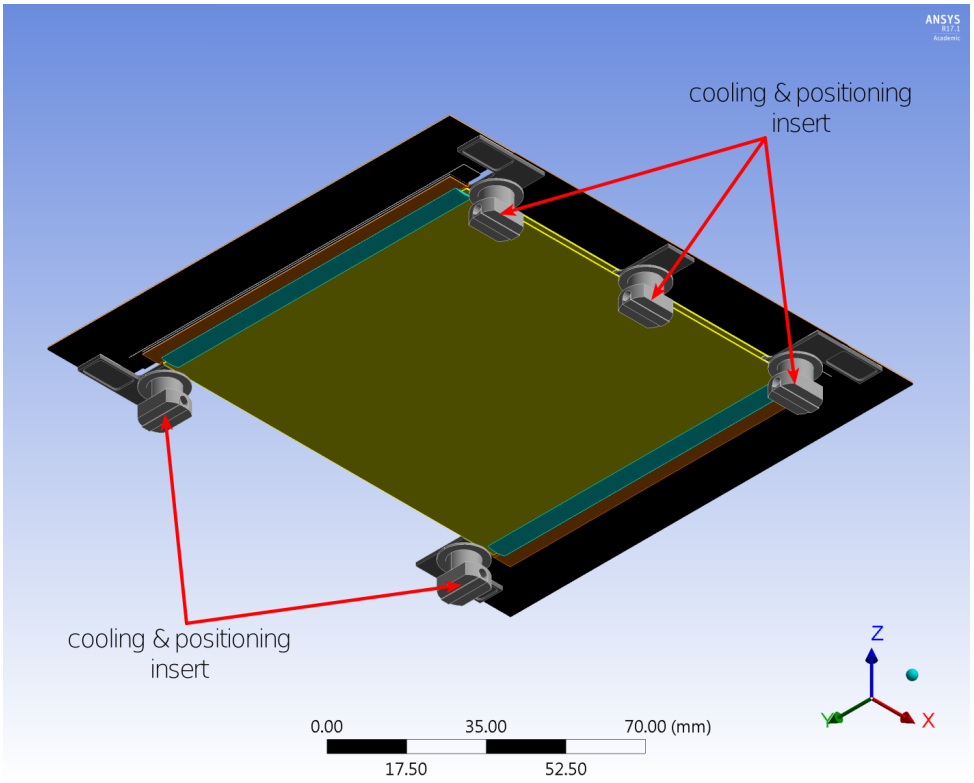

(a)

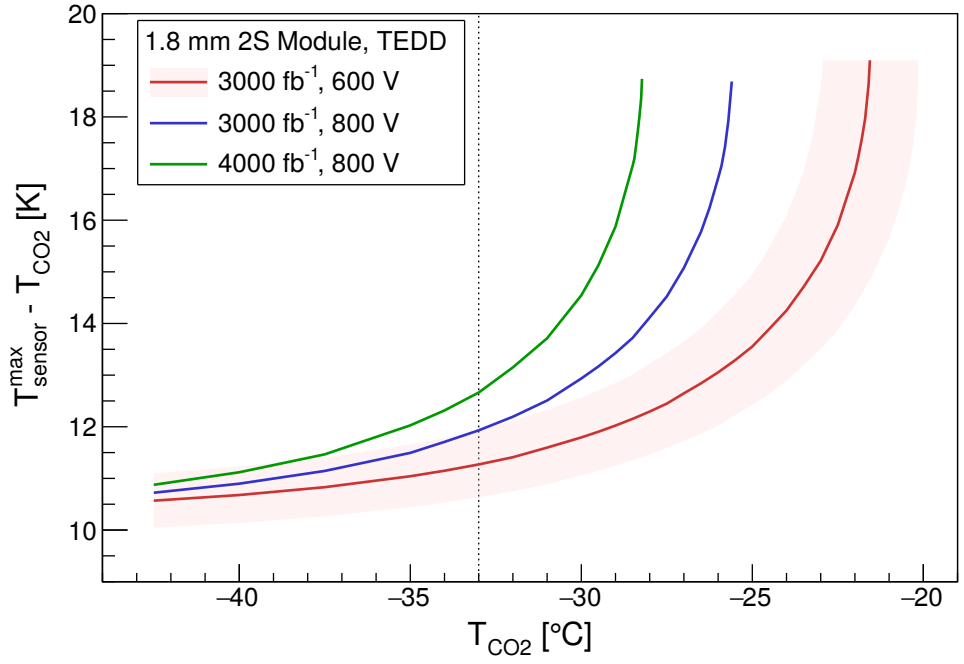

(b)

Figure 3.5.: Input geometry for thermal simulations of irradiated 2S modules with 1.8 mm sensor spacing (a) and the corresponding simulation results for the thermal runaway temperature (b) [CMS17].

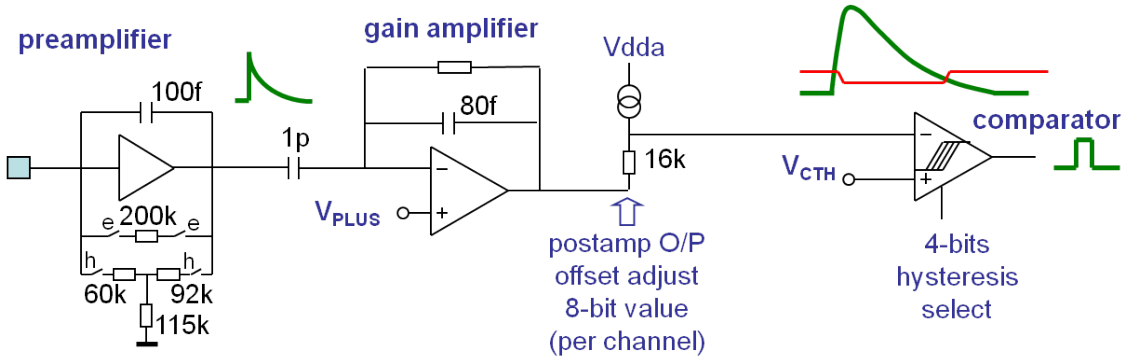

Figure 3.6.: Analog front-end of a CMS Binary Chip of the second generation. The charge generated in a silicon strip is amplified in the preamplifier, gain amplifier and postamplifier and compared to the global threshold V_{CTH} to produce a digital output [Bra13].

4. The 2S Module Readout Station

During the Phase II Upgrade of the CMS Experiment, the outer part of the silicon tracker will be replaced. The updated Outer Tracker consists of 2S and PS modules. These modules will be assembled by several institutes of the CMS community. The *Institut für Experimentelle Teilchenphysik* (ETP) at the *Karlsruher Institut für Technologie* is an assembly center for 2S modules and will manufacture about 2000 of these. The production flow for a 2S module assembly is presented in Chapter 3.3.1. As shown in Figure 3.4b, the functionality of each assembled module will be tested before and after the final encapsulation of the wire-bonds connecting the sensors and the readout chips. To guarantee a reliable and reproducible functional test allowing to characterize the quality of the production process, an appropriate test station is necessary. In this chapter, a design for a temperature stabilized 2S module readout station is presented.

Chapter 4.1 introduces the basic concepts that have driven the design of the station. During the design process some thermal simulations have been performed. These are discussed in Chapter 4.2 and compared to thermal measurements in Chapter 4.4. Chapter 4.3 presents the experimental setup. The functional tests performed in the developed station are summarized in Chapter 4.5. To easily control all test steps, a software framework with a graphical user interface has been developed, which is introduced in Chapter 4.6.

4.1. Basic Concepts

A test setup for functional tests of 2S modules has to fulfill several requirements to allow a reproducible test procedure under well defined conditions. The main features such a 2S module readout station has to provide are:

- **Easy and safe mounting:** During the production phase of 2S modules at ETP, it is planned to assemble up to eight modules per day. As each module will be tested two times for its functionality, the test station has to cope with a throughput of up to 16 modules per day. Therefore, it is desirable to provide a fixation mechanism for the modules which is easy and quick to handle. Additionally, the risk of damaging the modules during the mounting and removal processes in the station has to be minimized as much as possible. Thus, the fixation mechanism has to be designed without the usage of loose parts, e.g. screws.
- **Powerful cooling:** To allow the operation of 2S modules under the future thermal conditions in the CMS experiment, a sufficiently dimensioned cooling system

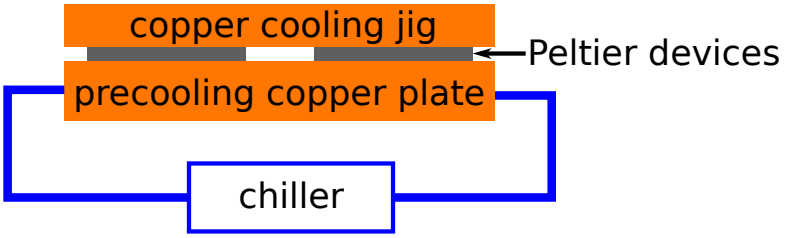

Figure 4.1.: Schematic view of the two stage cooling system for the 2S module test station. The precooling stage acts as a heat bath and stabilizes the temperature of the lower copper plate. The second cooling stage consists of Peltier devices which produce a dynamically controllable temperature difference between precooling copper plate and the copper cooling jig onto which the 2S modules will be fixed.

is needed. During the functional test procedure, the temperature should be kept constant to prevent temperature induced differences between different test results. Additionally, the desired temperatures should be reached as quickly as possible to minimize the required time for the tests during the production. Such a system also allows testing the influence of thermal stress on the module's mechanics.

- **Automation of test procedure:** In order to simplify the test procedure during the production phase, it is planned to automate as many routines as possible for the modules' functional tests.

4.2. Thermal Concept of the Cooling System

The first prototypes of 2S modules are assembled before the production phase starts. To test and validate the module concept and the assembly process, it is important to check the prototypes for their electrical functionality and their mechanical robustness. Hence, it is planned to investigate the influence of thermal stress on the modules' mechanics by performing thermal cycles between room temperature and the expected operating temperature in the CMS detector.

In order to quickly reach the desired temperatures, a two stage cooling system is used, consisting of Peltier devices and a liquid based cooling circuit. A drawing of the cooling system can be found in Figure 4.1. The first stage is formed by a chiller operating a coolant circuit with constant set temperature which stabilizes the temperature of a copper block. This precooling stage acts as a heat bath for the second cooling stage, which consists of thermoelectric coolers and a cooling jig made of copper. As the Peltier devices are mounted in between the precooling block and the cooling jig, the temperature on the cooling jig can be dynamically changed and controlled via the electric power of the Peltier devices. Thus, the temperature of 2S modules can be controlled by mounting them on the cooling jig.

To reach the temperature levels expected in the CMS detector during operation and shutdown phases, a correctly dimensioned cooling system is needed. Therefore, some thermal simulations of the two cooling stages have been performed during the design process to determine the optimal configuration. These simulations are based on finite element analysis and are carried out using the software framework ANSYS [ANS17].

4.2.1. Basics of Finite Element Method for Thermal Analysis

To analyze the thermal behavior of a system, the fundamental laws of thermodynamics have to be solved for the system's geometry. There are three different mechanisms of heat transfer, see e.g. [Dem18]:

- **Thermal conduction** describes the heat transfer in a solid, fluid or gas without any transport of mass. Thermal conduction occurs between regions with temperature gradients. The thermal energy will be transported from the warmer to the colder region. The thermal conductivity λ is used to characterize the ability of a material to conduct heat and correlates the heat flux density $\vec{q}$ with the temperature gradient via

$$\vec{q}_{\text{cond}} = -\lambda \vec{\nabla} T \ . \tag{4.1}$$

  Equation 4.1 is called Fourier's law.

- **Thermal convection** describes the heat transfer by moving particles. It can be distinguished between free and forced convection depending on the existence of an external force to drive the particle movement. Convection is the dominant heat transfer mechanism in gases and fluids and, thus, also exists at the surface between solids and gases. The heat flux $\dot{q}_{\text{conv}}$ depends on the temperature difference ΔT between the surface and the environment and can be calculated by

$$\dot{q}_{\text{conv}} = \alpha \cdot \Delta T \ , \tag{4.2}$$

  where α is the heat transfer coefficient.

- **Thermal radiation** is electromagnetic radiation emitted by all matter with a temperature larger than 0 K caused by the non-vanishing thermal movement of charged particles. To characterize the efficiency of a material to emit thermal energy via radiation at its surface, the emissivity ϵ can be used. The emissivity compares the emitted heat flux with the heat flux emitted by the surface of an ideal black body with the same temperature. An ideal black body is defined as a body which absorbs all incident electromagnetic radiation and emits radiation following Planck's law.

In order to analyze the thermal behavior of a system, the influence of these three mechanisms have to be calculated for the system's geometry. Depending on the complexity of this geometry, a large set of differential equations has to be solved to evaluate the temperature distribution at every point. This can be done numerically using finite element analysis (FEA).

As a first step in an FEA, the whole system's geometry is divided into numerous small elements with finite size. The vertices of each element are called *nodes*. During an FEA, the temperature will be exactly calculated at each node. By interpolating the temperatures of adjacent nodes, the temperature distribution inside the small elements can be approximated. Further information about the concepts of FEA can be found e.g. in [Hut04].

All simulations presented in this thesis are steady-state thermal simulations performed with the *Analysis System* (ANSYS) software framework [ANS17]. During a thermal steady-state analysis the equilibrium state is calculated at which temperature distributions and all thermal flows remain stable over time.

4.2.2. Simulation of the Cooling Jig

As shown in Chapter 3.3.2, a 2S module which is irradiated to the fluence expected for an integrated luminosity of 3000 fb^{-1} and operated at a bias voltage of −800 V generates a thermal heat load of approximately 6 W. This power has to be removed via the aluminum/carbon fiber spacers at the five fixation points of each module, where they will be fixed to the cooling inserts in the CMS experiment. At the module production centers, the fully assembled 2S modules will be mounted on an aluminum carrier at the end of the assembly process. This carrier simplifies the handling and minimizes the risk of damaging

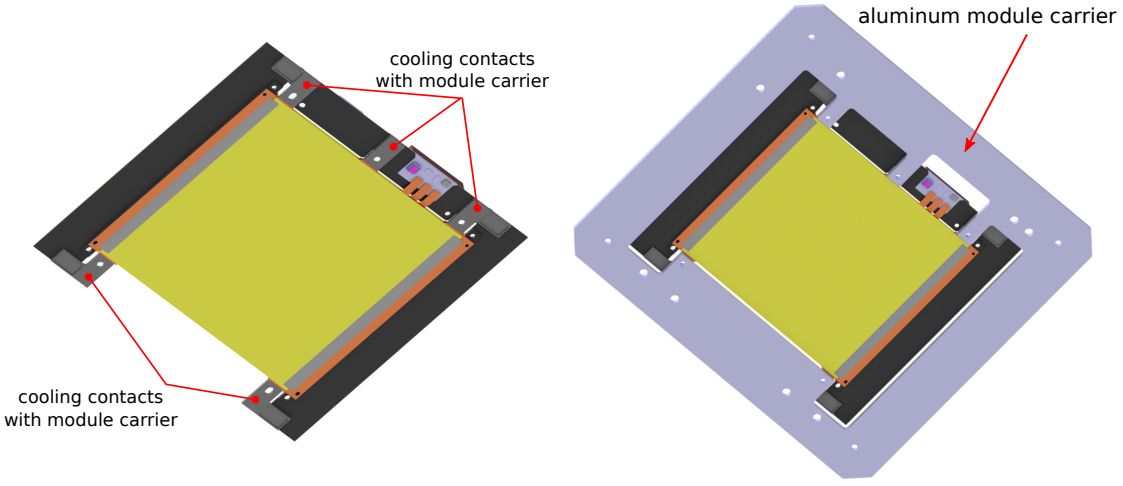

(a) (b)

Figure 4.2.: A 2S module seen from below before (a) and after (b) the mounting on an aluminum module carrier. The carriers are used in the module production centers to handle the assembled modules. The module can be cooled via the carrier at the five mounting points where the module is screwed on the carrier.

Table 4.1.: Summary of the material properties used as input parameters for the thermal simulations performed with ANSYS [ANS17]. The aluminum-magnesium alloy $AlMg_3$ is used to simulate the material of the module carrier. The cooling jigs and the precooling stage are made of copper (Cu).

Material	Isotropic Thermal Conductivity λ	Emissivity ϵ	Convection Film Coeff.
$AlMg_3$	$120\,\mathrm{Wm^{-1}K^{-1}}$	0.2	$10\,\mathrm{Wm^{-2}K^{-1}}$
Cu	$385\,\mathrm{Wm^{-1}K^{-1}}$	0.8	$10\,\mathrm{Wm^{-2}K^{-1}}$

the modules. The modules can be screwed on the carrier at the five fixation points in the spacers, which is illustrated in Figure 4.2. Therefore, the module can be cooled by cooling the carrier. This is realised in the 2S module readout station by placing the carrier on two separate copper jigs as it is depicted in Figure 4.3.

To determine the thermal power and optimal number of Peltier devices to meet the nominal set temperature of the CO_2 cooling system in the future CMS experiment, thermal simulations have been performed using the software framework ANSYS [ANS17]. The input geometry is illustrated in Figure 4.3. To model the thermal heat load of an operating 2S module, a heat source introduces a thermal power of 1.2 W to the carrier surface at each of the five module fixation points. It is planned to operate all Peltier devices in a parallel circuit. Thus, the operation of the thermoelectric coolers is simulated by removing a thermal power P_{Peltier} for each device at the bottom side of the cooling jigs. The environmental temperature is set to be 22°C and radiative and convective interactions are simulated for every non-covered surface using the material properties summarized in Table 4.1.

The simulations are performed with a total number of four, five and six thermoelectric coolers below the two cooling jigs. During each simulation P_{Peltier} is modified until the average temperature of the five module fixation points reaches equilibrium at −35°C. Table 4.2 summarizes the results of the simulations. As expected, the thermal power

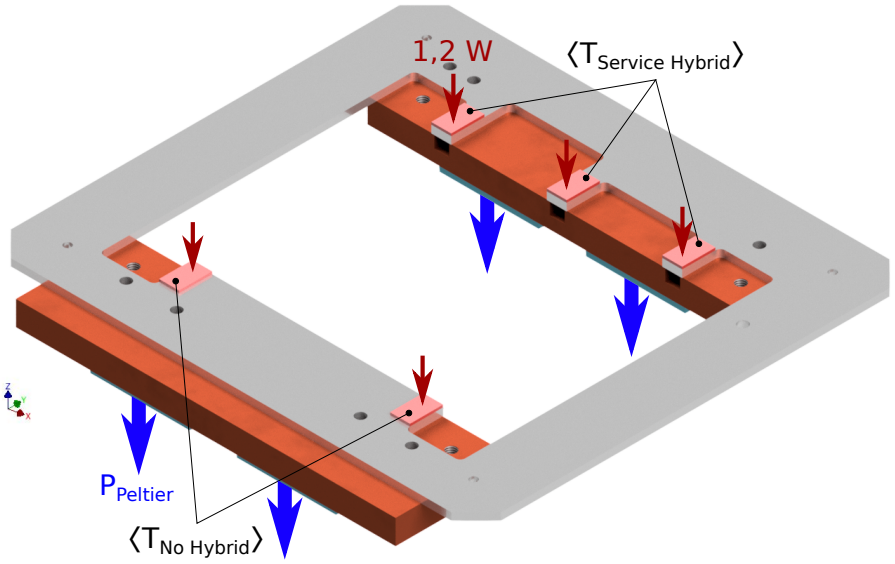

Figure 4.3.: Input geometry for the thermal simulations of the Peltier cooling stage. The aluminum module carrier is placed on two copper cooling jigs, which are cooled by Peltier devices. To simulate the heat load of a 2S module, a thermal power of 1.2 W is introduced to the carrier at each of the five module fixation points. Each Peltier device removes the power P_{Peltier} at the bottom side of the cooling jigs.

Table 4.2.: Results of the thermal analyses of the Peltier cooling stage for different configurations of the Peltier devices. In thermal equilibrium the average temperature on the support points for the 2S modules on the aluminum module carrier is measured. The nomenclature is introduced in Figure 4.3.

n_{Peltier}	$\langle T_{\text{Service Hybrid}} \rangle$ (°C)	$\langle T_{\text{No Hybrid}} \rangle$ (°C)	ΔT (°C)	P_{Peltier} (W)
4	−34.8	−35.6	0.8	9.3
5	−41.1	−28.2	−12.9	7.3
6	−35.2	−36.0	0.8	6.2

needed from each Peltier device decreases with increasing number of thermoelectric coolers. The cooling system has to be able to stabilize the temperatures at the five fixation points at approximately the same level in order to minimize the temperature gradient between the two sides of a 2S module and, therefore, to minimize the internal thermal stress on the module. A similar temperature level can only be realised with the geometries using four and six Peltier devices, where the temperature difference between the two sides is smaller than 1°C. In these configurations, the thermoelectric coolers need to provide a thermal power of 9.3 W (6.2 W) for a geometry with four (six) Peltier devices.

In order to guarantee a fast cooling process, the thermoelectric coolers have to provide a sufficient maximum thermal power. The maximum thermal power of Peltier devices is dependent on the temperature difference between their two sides and the absolute temperature T_w of the warmer side. Thus, the combination of Peltier devices and the operating temperature of the precooling stage has to be adjusted correctly. It is planned to use the Peltier devices *TEC1-12705* produced by the company *Hebei I.T (Shanghai) Co.* A

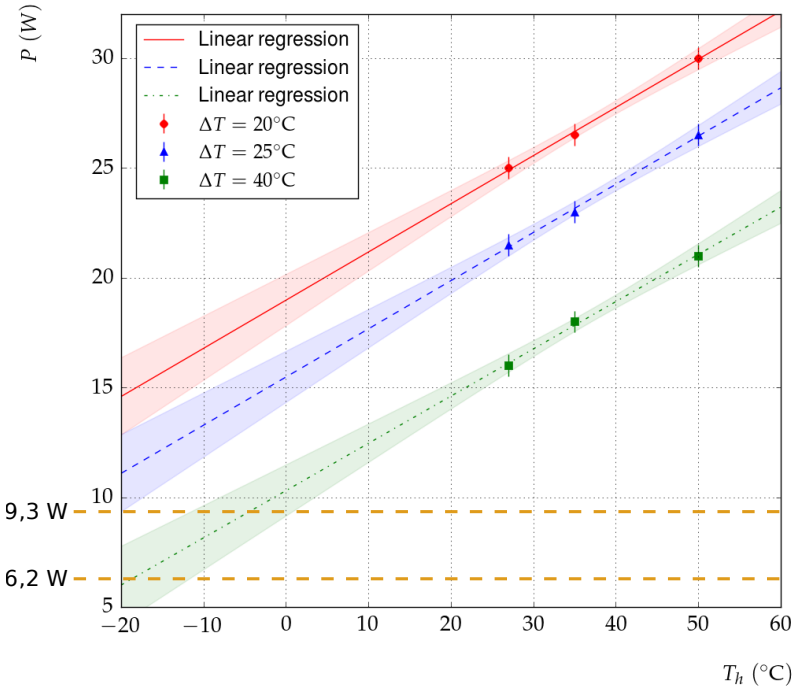

Figure 4.4.: Estimation of the maximum thermal cooling power P of the *TEC1-12705* Peltier devices as a function of the temperature on the warmer side of the devices for three temperature differences ΔT of 20°C, 25°C and 40°C. The dashed orange lines indicate the cooling power for each Peltier device needed to operate the Peltier cooling stage with four (9.3 W) or six Peltier devices (6.2 W) at a constant temperature level of −35°C.

datasheet can be found in Appendix A.3, which includes performance curves showing the thermal power as a function of temperature difference for $T_w = 50°C$, $T_w = 35°C$ and $T_w = 25°C$ [Eve]. The higher the temperature difference gets, the more the cooling power decreases. Additionally, the cooling power decreases with decreasing T_w.

To efficiently reach cooling jig temperatures of −35°C, it is necessary to operate the Peltier devices with $T_w < 10°C$. Assuming a linear decrease of the cooling power with T_w, the maximum thermal power of the thermoelectric devices can be estimated for T_w lower than shown in the datasheet. Figure 4.4 summarizes the results of the linear extrapolations for temperature differences of 20°C, 25°C and 40°C on the Peltier devices. The minimum thermal power needed to stabilize the carrier temperature at −35°C for a geometry with four and six Peltier devices is marked as dashed orange lines.

For a coolant circuit temperature of 4°C, the Peltier devices need to be operated at a temperature difference of 40°C. As their maximum thermal power at this working point is approximately 10 W, a geometry with four Peltier devices cannot provide sufficient cooling power to ensure a fast cooling process. Thus, for this coolant configuration a geometry with six Peltier devices is preferable. By lowering the coolant temperature, the maximum thermal power of the devices decreases, but the needed temperature difference decreases simultaneously. For a coolant temperature of −10°C the Peltier devices have to provide a temperature difference of 25°C to reach −35°C. The maximum thermal power of the thermoelectric coolers at $T_w = -10°C$ is approximately 13 W. Following Figure 4.4, with this coolant temperature a configuration with four Peltier devices is sufficient to provide a fast and stable cooling process.

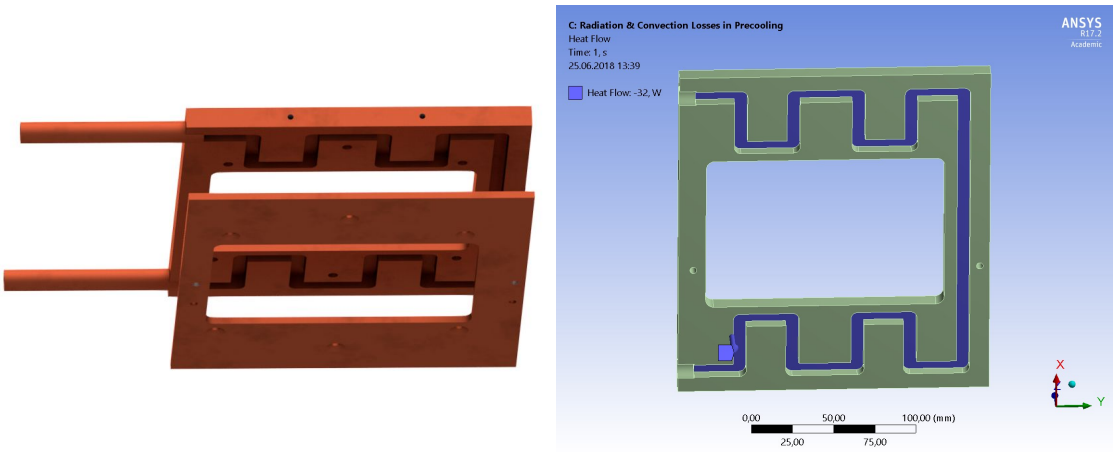

(a) (b)

Figure 4.5.: Simulation geometry to determine the thermal losses of the precooling copper block through convection and radiation at the two possible coolant set temperatures. The input geometry for the simulation is shown in (a). To simulate the heat removal by the coolant, a constant thermal power is removed from the top surface of the cooling pipe as depicted in (b).

4.2.3. Simulation of the Precooling

In order to achieve an efficient cooling system, it is important to optimally adjust the two cooling stages with respect to each other. To transfer the heat from the Peltier devices to the coolant, a copper cooling block flown through by coolant is used. To realize the coolant pipe, the block consists of two separate copper layers, as illustrated in Figure 4.5a. The cooling pipe is milled into one of the layers and afterwards the two parts are soldered together, with connector nozzles being included for the external cooling circuit.

As discussed in Chapter 4.2.2, there are two different possible configurations for the Peltier cooling stage. Either the coolant is operated at a temperature of 4°C and there are six Peltier devices below the two cooling jigs, or the coolant set temperature is −10°C and four Peltier devices are sufficient to stabilize the temperature on the cooling jigs. The chiller operating the coolant circuit has to provide enough cooling power to remove the heat produced by the Peltier devices and to compensate the thermal losses of the precooling block through convection and radiation at the two possible coolant temperatures. To determine these thermal losses, a simulation will be used.

The input geometry for the simulation is depicted in Figure 4.5a. Based on the parameters summarized in Table 4.1, radiation and convection processes are applied to all external surfaces. The environmental temperature is set to be 22°C. To simulate the heat removal through the coolant, a constant thermal power P_{coolant} is removed from the top surface of the cooling pipe as illustrated Figure 4.5b. During the simulations P_{coolant} is varied until the temperature at this surface reaches approximately 4°C or −10°C, respectively. The resulting temperature distributions on the precooling block can be found in Appendix A.2.2. To stabilize an average temperature of 4°C on the precooling, the coolant needs to absorb 18.8 W of thermal power to compensate the thermal losses through radiation and convection. To reach an average temperature of −10°C, the coolant needs to absorb 32 W.

The chiller has to provide a minimum cooling power in order to efficiently operate the precooling. This power can be calculated by summing up the thermal losses through radiation and convection and the maximum power introduced to the precooling by the Peltier devices. The maximum power of the Peltier devices is given by their electrical power

of $P_e = 5\,\mathrm{A} \cdot 12\,\mathrm{V} = 60\,\mathrm{W}$ and their maximum thermal power estimated in Chapter 4.2.2 for the two possible coolant set temperatures. Regarding the configuration with six Peltier devices and a set temperature of 4°C, each Peltier device introduces a maximum heat load of 70 W to the precooling. This leads to a total heat load of 438.8 W, which has to be absorbed by the coolant. In comparison, the configuration with four Peltier devices and a set temperature of −10°C leads to a maximum heat load of 73 W of each Peltier device and a total heat load of 324 W for the coolant.

For the production of 2S modules at the *Institut für Experimentelle Teilchenphysik* it is planned to operate two 2S module readout stations in parallel in order to enlarge the throughput of modules during their functional tests. Ideally, these two stations are operated with the same coolant circuit to minimize the amount of equipment in the laboratory. Thus, the chiller requires to provide at minimum a thermal power of 650 W at a coolant temperature of −10°C or a power of 880 W for a coolant temperature of 4°C. These performance requirements are met by the recirculating chiller *ULK 2002* of the company *Fryka-Kältetechnik GmbH*, which provides a cooling capacity of 750 W at −10°C and 1600 W at 10°C, respectively [Fry]. A datasheet can be found in Appendix A.4.

In order to minimize the thermal power which needs to be transferred from the precooling copper block to the coolant, the geometry with four Peltier devices between precooling and cooling jigs is chosen. The complete setup is presented in the following.

4.3. Experimental Setup

The geometry of the functional test station for 2S modules has been developed and optimized in an iterative process considering the results of the thermal simulations presented in Chapter 4.4 in order to fulfill all requirements mentioned in Chapter 4.1. Figure 4.6 illustrates the assembled main part of the station. The cooling stage is formed by a copper block, which can be connected to an external cooling circuit and acts as precooling for four Peltier devices. These Peltier devices are mounted on top of the precooling block and are connected on their top side with two copper cooling jigs. With this configuration, it is possible to dynamically and quickly control the temperatures of the two cooling jigs by adjusting the electrical power of the thermoelectric coolers. The geometry of the cooling jigs has been adapted to the module carrier by providing holes in the copper at the positions where screws protrude from the bottom side of the carrier.

To fix the module carrier on the cooling jigs, four spiral springs are integrated in a rotatable aluminum frame mounted above the jigs. By lowering the frame the carrier gets pressed down at four points onto the jigs to ensure a good cooling contact. This position can be fixed using a handle which prevents the frame from opening. All these parts are mounted on a common plate made of fiberglass which insulates the setup electrically to the ground.

The temperature of the cooling jigs and the precooling is measured using resistance temperature sensors made of platinum. One temperature sensor is mounted on each of the cooling jigs and the precooling block houses two sensors, which are read out by a custom circuit board via four-terminal sensing. To control the average temperature on the cooling jigs a PID algorithm is used, which will be further described in Chapter 4.6. Two additional temperature sensors mounted on one of the jigs and on the precooling allow installing a protective circuit to shut-down the Peltier cooling stage in case of overheating.

During the cooling procedure, it is crucial to stabilize the dew point of the air inside the station at a level lower than the temperatures used in the two cooling stages. Therefore, the whole setup pictured in Figure 4.6 is placed inside a custom designed aluminum box. This box is lined with temperature insulating material and additionally allows testing of the module without exposure to light and acts as shielding against radioactive and

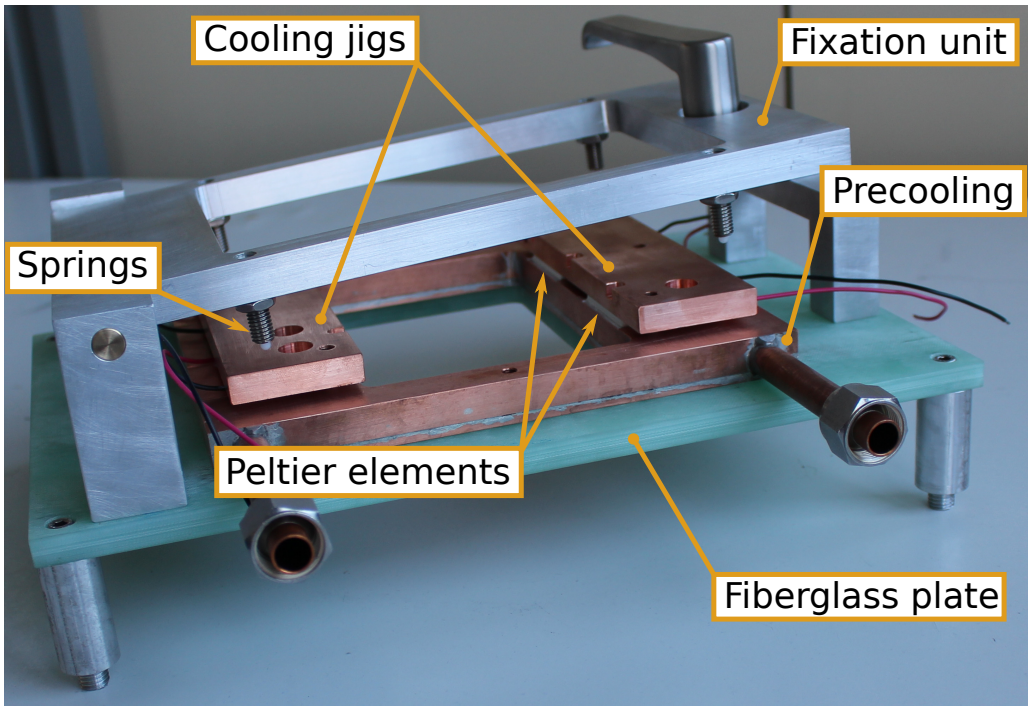

Figure 4.6.: Picture of the cooling stage with fixation unit for the 2S module functional tests. The modules are pressed with springs onto the cooling jigs to provide a good cooling contact. To test the electrical readout, charge can be introduced into the sensors by placing a radioactive source above or below the module.

electromagnetic radiation. The box is continuously flushed with a small flux of dried air to compensate leaks at the openings for cooling nozzles and electrical connections. To enlarge the air flux a remotely controllable valve can be opened to quickly lower the dew point after closing the box. To determine the dew point inside the aluminum box and the laboratory, two 1-wire sensors are used. An overview of the station and additional external equipment in the laboratory can be seen in Figure 4.7.

As determined in Chapter 4.2, the precooling will be operated at a coolant set temperature of $-10°C$. The measured average dew point in the laboratory is around $4°C$. To prevent condensation of water on the module or parts of the test station, it is necessary to warm up both cooling stages to temperatures above the current dew point level before opening the aluminum box. To warm up the precooling block, the cooling circuit can be closed outside the box by redirecting the coolant through a bypass. In total, the operator has to manually change the status of three valves to enable or disable this bypass. Before opening the bypass, it is necessary to shut down the Peltier devices to prevent them from overheating. With the bypass enabled, the coolant cannot enter the box anymore and the precooling block can be warmed up to temperatures above the laboratory dew point by opening the remotely controllable valve and flushing the box with dried air. Details on the handling of the station can be found in Appendix A.1.

In order to check the functionality of the module's readout, a radioactive source can be fixed above and below the module in the station. Thus, the two sensors can be irradiated in two directions and the produced charge can be read out via the readout chips. To test the sensors' detection efficiencies for particle crossings, a plastic scintillator with an area of $15 \times 15\,\mathrm{cm}^2$ is installed below the cooling unit. The scintillator is read out using an avalanche photodiode (APD). This allows operating the module with an external trigger signal. A detailed picture of the setup inside the aluminum box can be found in Figure A.7.

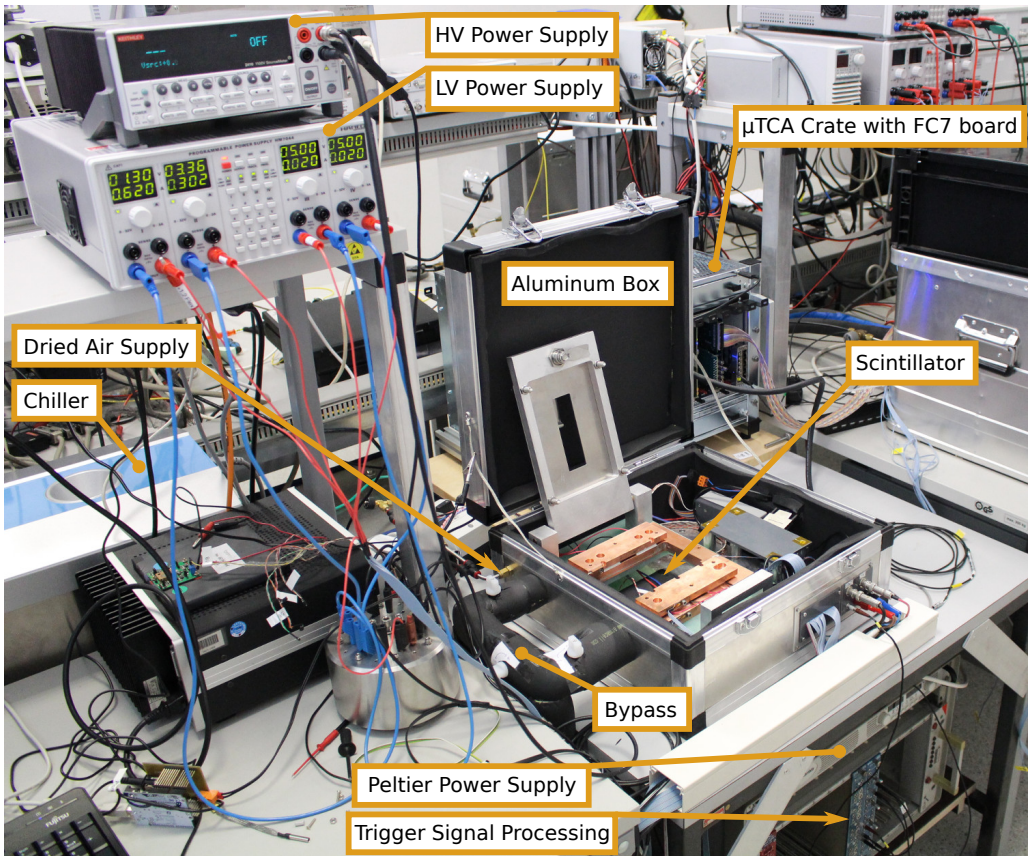

Figure 4.7.: Experimental setup of the 2S module functional test station in the laboratory. The station is placed inside an aluminum box which is continuously flushed with dried air. A bypass in the cooling circuit can be opened to warm up the precooling above the dew point in the laboratory before opening the box. A scintillator is fixed below the cooling stage.

Figure 4.7 illustrates the whole test setup in the laboratory with additional external devices. A high voltage power supply delivers the bias voltage to the sensors of a 2S module while a four channel power supply provides the voltage levels for the readout electronics. Before the APD output can be used as trigger input to the 2S module readout, it has to be discriminated and converted to the transistor-transistor logic which is done with a processing rack. To read out a 2S module, an FC7[1] board is used which can be operated inside a µTCA crate. The FC7 board can be equipped with two FMC cards, one for the communication with the module and the other for trigger input. The µTCA crate is connected to the local network and can be controlled via the *Phase 2 Acquisition and Control Framework* (Ph2_ACF), which will be introduced in Chapter 4.5.1. The arrangement of powering and ground connections is presented in Chapter 4.5.2.2.

4.4. Thermal Performance

After the assembly of the test station, some measurements are conducted to test the performance of the cooling stages and to verify the thermal simulations presented in Chapter 4.2.

[1]Flexible *Advanced Mezzanine Card* (AMC) developed by the CMS community. More information can be found at `https://espace.cern.ch/project-FC7/SitePages/Home.aspx`

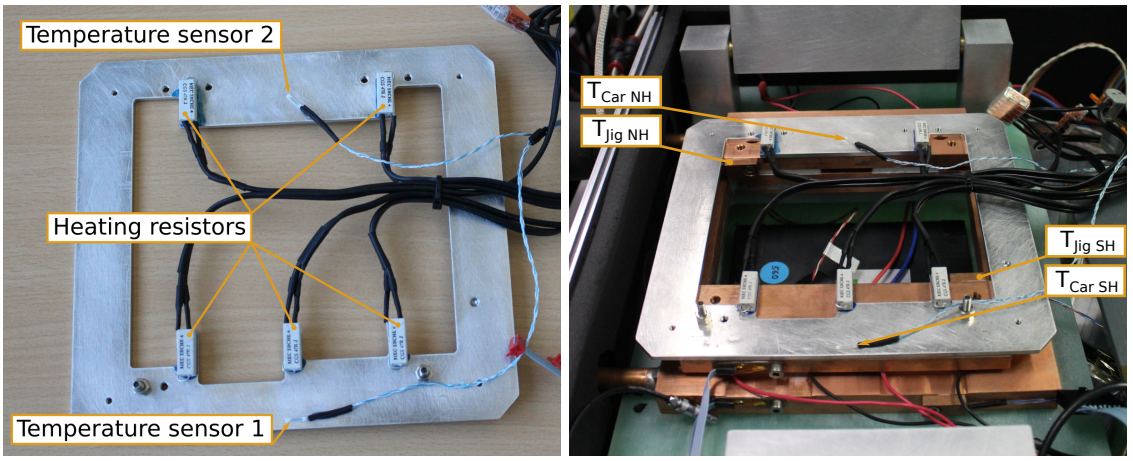

(a) (b)

Figure 4.8.: Heating resistors glued to a module carrier in order to test the thermal performance of the 2S module functional test station seen from above (a) and mounted in the station (b). The temperature is read out by two temperature sensors on the carrier.

4.4.1. Thermal Cycles

To characterize the thermal performance of the station, the minimal reachable temperature is determined by operating the Peltier devices at maximum power. Starting from 20°C, the average temperature on the two cooling jigs reaches −45°C after 16 minutes and saturates after ten more minutes at approximately −46°C. Thus, the station is able to reach the temperature levels expected for the CMS CO_2 cooling system of approximately −35°C [CMS17]. Additionally, the station allows testing the influence of thermal stress on the functionality of 2S modules during prototyping. Therefore, thermal cycles with non biased modules are performed between 20°C and −35°C on the cooling jigs. At each of these two temperatures, the temperature gets stabilized for 60 s before continuing the cycles. In this configuration one thermal cycle needs approximately twelve minutes, meaning a maximum of 120 cycles can be performed in 24 hours. The cooling process from 20°C to a stable temperature at −35°C takes approximately seven minutes.

4.4.2. Experimental Setup and Measurements with Heating Resistors

To verify the results of the thermal simulations, the cooling system is additionally validated with an active heat source to simulate an operating irradiated 2S module. Five heating resistors are glued onto the fixation points of a module carrier, as can be seen in Figure 4.8a. Two platinum resistance thermometers are used to measure the temperatures on the two sides of the carrier, where it has contact with the cooling jigs (see Figure 4.8b). The heating resistors provide a resistivity of 47 Ω each and are operated in a parallel circuit. After placing the module carrier on the cooling jigs, the rotatable aluminum frame is closed and the carrier is pressed by the four spiral springs onto the jigs. After closing the box, the cooling process is started and the temperature sensors of the station and of the carrier are read out.

When the average temperature of the cooling jigs has stabilized at −35°C, the power of the heating resistors is increased stepwise from 0 W to 6.7 W and the four temperature sensors are continuously monitored. For every step the data of each temperature sensor is averaged and plotted in Figure 4.9. The Peltier devices can provide sufficient power to stabilize an average temperature of −35°C on the cooling jigs independent of the introduced heat load. The maximum temperature difference between the two jigs is approximately 0.2°C.

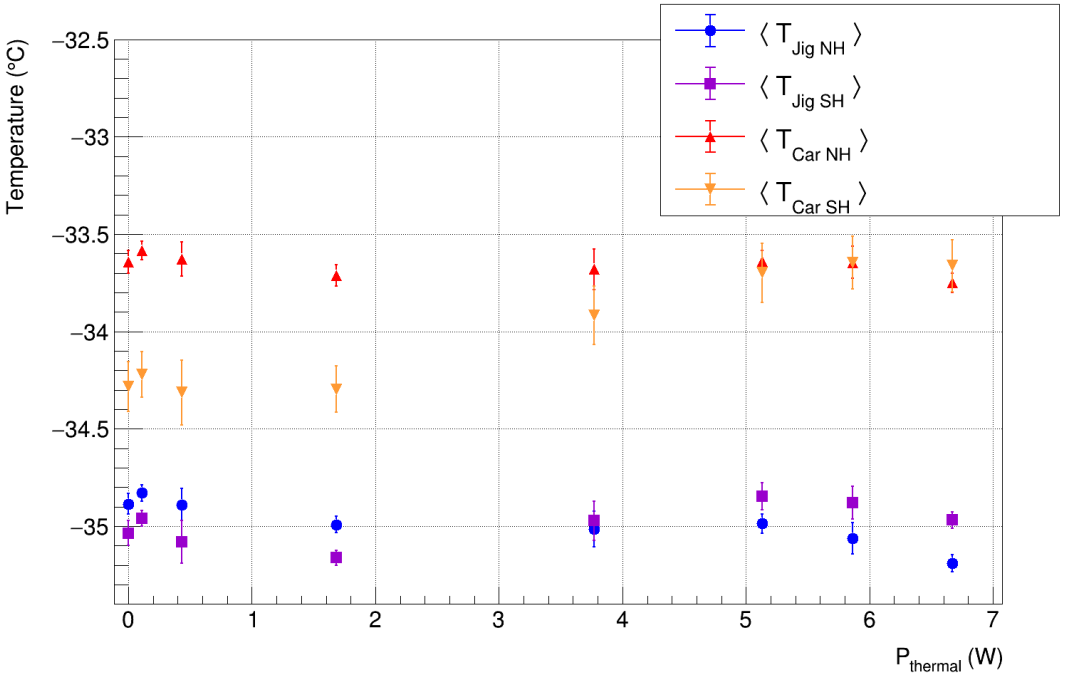

Figure 4.9.: Average temperatures measured on the two cooling jigs ($\langle T_{\text{Jig SH}} \rangle$ and $\langle T_{\text{Jig NH}} \rangle$) and on the surface of the module carrier ($\langle T_{\text{Car SH}} \rangle$ and $\langle T_{\text{Car SH}} \rangle$) for different total heat loads P_{thermal} introduced to the carrier by five heating resistors.

Nevertheless, the effect of increasing the thermal power can be observed in the data. As the arrangement of the resistors on the module carrier is asymmetric and the arrangement of Peltier devices below the two cooling jigs is symmetric, the jig below the service hybrid side of a 2S module warms up with increasing heat load relative to the opposite cooling jig. Thus, for heat loads larger than 3 W $\langle T_{\text{Jig SH}} \rangle$ gets larger than $\langle T_{\text{Jig NH}} \rangle$.

Comparing the values of the two temperature sensors on the surface of the module carrier with each other, their maximum difference is approximately 0.6°C for thermal heat loads below 3 W. This difference is slightly larger than the temperature differences measured between the corresponding sensors on the cooling jigs. This effect originates from the thermal contact between the aluminum module carrier and the copper jigs. As already mentioned, the carrier gets pressed down onto the jigs at four points by spiral springs. As neither the surface of the carrier nor the surfaces of the jigs are completely flat, the cooling contact can differ between the two carrier sides, which can lead to this slight temperature difference. With an increasing heat load this difference reduces and reaches approximately 0.1°C for a thermal power of 6 W. This, also, is a consequence of the asymmetric heat generation on the carrier.

The thermal simulations presented in Chapter 4.2.2 predicted a temperature difference of 0.8°C between the two sides of the carrier, assuming a full-faced thermal contact at the interfaces between carrier and jigs. Taking into account the non-ideal cooling contact between carrier and jigs, which leads to a measured temperature difference on the carrier of approximately 0.6°C for no thermal heat load, this experimental results can be brought into accordance with the thermal simulations.

To sum up, the two cooling stages of the functional test station are able to efficiently cool an irradiated 2S module at the thermal conditions expected in the CMS experiment. The desired temperatures can be reached quickly and are stabilized within a range of less

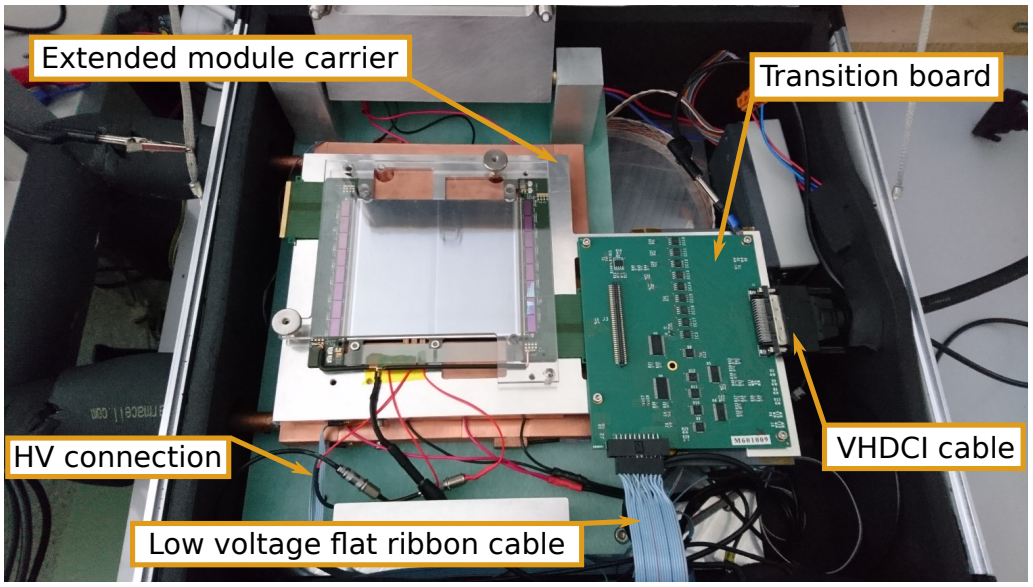

Figure 4.10.: The 2S module functional test station is suitable to test an 8CBC2 module mounted on a specially designed carrier. One hybrid can be read out at a time via the transition board screwed onto the carrier extension. The transition board is powered by a flat ribbon cable and the data from the CBCs is sent to an FMC card by the VHDCI cable.

than $\pm 0.5°C$.

4.5. Functional Tests of an 8CBC2 Module

At the time of writing this thesis, the *Institut für Experimentelle Teilchenphysik* has successfully assembled one functional 2S module. This module is equipped with two front-end hybrids housing eight CMS Binary chips (CBCs) of the second iteration, so-called 8CBC2 hybrids. To read out these hybrids they have to be connected to a transition board which provides electrical power and enables data transmission to a FMC card mounted on a FC7 board via a VHDCI cable. As can be seen in Figure 4.10, the geometry of the readout station is suitable to place one transition board inside the aluminum box to read out one front-end hybrid of an 8CBC2 module at a time. To fix the transition board with respect to the module, a specially designed aluminum carrier is used. This carrier provides an extension onto which the transition board can be screwed. In order to read out the other front-end hybrid, the module can be turned by 180° on the carrier.

4.5.1. The Phase 2 Acquisition and Control Framework

To readout a 2S module the *Phase 2 Acquisition and Control Framework* (Ph2_ACF)[2] is used, which has been developed by the CMS community. The Ph2_ACF communicates with the FC7 boards, collects and processes the data from the modules. In order to test the functionality of a 2S module, this software framework can be used to provide the following basic tools:

- A **calibration** of all CBCs on a module has to be done in order to level the response behavior of all channels. This can be achieved by adjusting the pre- and gain amplifiers of the CBC's analog front-end. Therefore, the pedestals of all channels have to be measured, which are defined as the threshold values for which the channel's

[2] `https://gitlab.cern.ch/cms_tk_ph2/Ph2_ACF`, last visited at August 2nd, 2018

occupancy reaches 50% due to noise hits. Afterwards, the pedestals can be leveled to a globally defined value (trim value) by adjusting the output of the post amplifier via the offset values per channel.

- Performing a **noise scan** allows to identify malfunctioning channels e.g. due to unconnected wire-bonds as shown in [Dro18]. Therefore, an S-curve is measured, which monitors the channel occupancies for different global thresholds V_{CTH}. With decreasing threshold a point is reached, where noise hits are registered in the channels and, thus, the occupancy rises. The noise of each channel is defined as the width σ of the S-curve. In order to determine the noise, an error function is fitted to the data following

$$F(x) = \frac{1}{2}\,\mathrm{erf}\left(\frac{x-\mu}{\sqrt{2}\sigma}\right) + c\ . \tag{4.3}$$

- To take data with a 2S module the **miniDAQ** is used. At each trigger signal, the registered hits in the strips are stored in the buffer and afterwards processed and sent out by the CBC. The Ph2_ACF stores this data in a file and provides the **miniDQM** to analyze it.

The configuration parameters to control the module's functionality and the Ph2_ACF routines are stored in a central file based on the *Extensible Markup Language* (XML). In this file, the trigger source for a measurement can be defined. The CBCs of the second iteration can be triggered with the Level-1 trigger of the CMS experiment, a constant trigger frequency, an external trigger (e.g. scintillator) or a trigger logic unit (TLU). Additionally, the CBCs can be triggered on stubs and on internal test pulses.

4.5.2. Functional Test Results

4.5.2.1. Temperature Dependent I-V Curves of 2S Sensors

The 2S module readout station provides the possibility to measure the leakage current of a fully assembled module as a function of bias voltage and temperature. During prototyping, this information is compared with the bare sensor data taken before the assembly process in order to determine the influence of the assembly on the sensor behavior. For the first assembled 8CBC2 module at the *Institut für Experimentelle Teilchenphysik*, it is possible to separately bias the top and bottom sensor. Figure 4.11 pictures the bias voltage dependence of the leakage current for each sensor at different cooling jig temperatures. For both sensors the leakage current decreases with decreasing temperature which corresponds to the expected behavior following Equation 3.3.

4.5.2.2. Noise Scan

For the operation in the CMS experiment the 2S modules' noise levels have to be minimized as far as possible in order to achieve a large signal-to-noise ratio. Therefore, the Ph2_ACF provides a noise scan to measure the noise level for all channels of a CBC in V_{CTH} units. The noise level of the system can easily be influenced by the laboratory environment during the modules' functional tests. Therefore, it is crucial to install a suitable routing scheme for the 2S module readout station in order to optimally shield the electrical connections from the environment and to use a suitable ground routing.

Figure 4.12 illustrates the electrical connection schematic used for 2S module readout station. The dashed blue lines represent the electrical connections, which provide the transition board with low voltage and the silicon sensors with high voltage. All lines

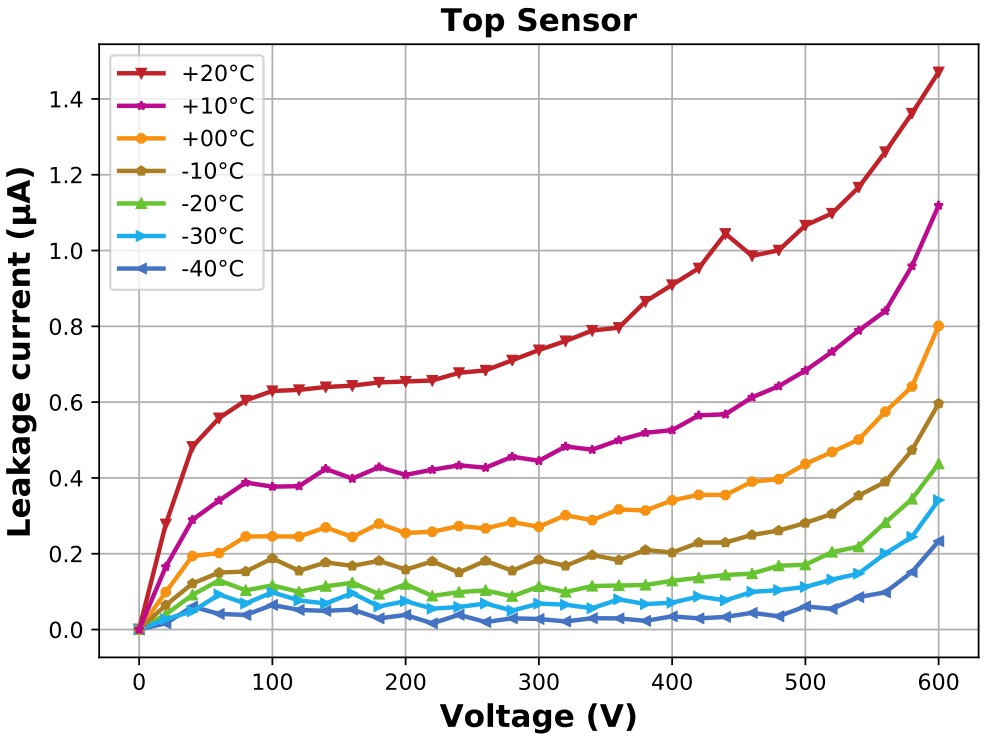

(a)

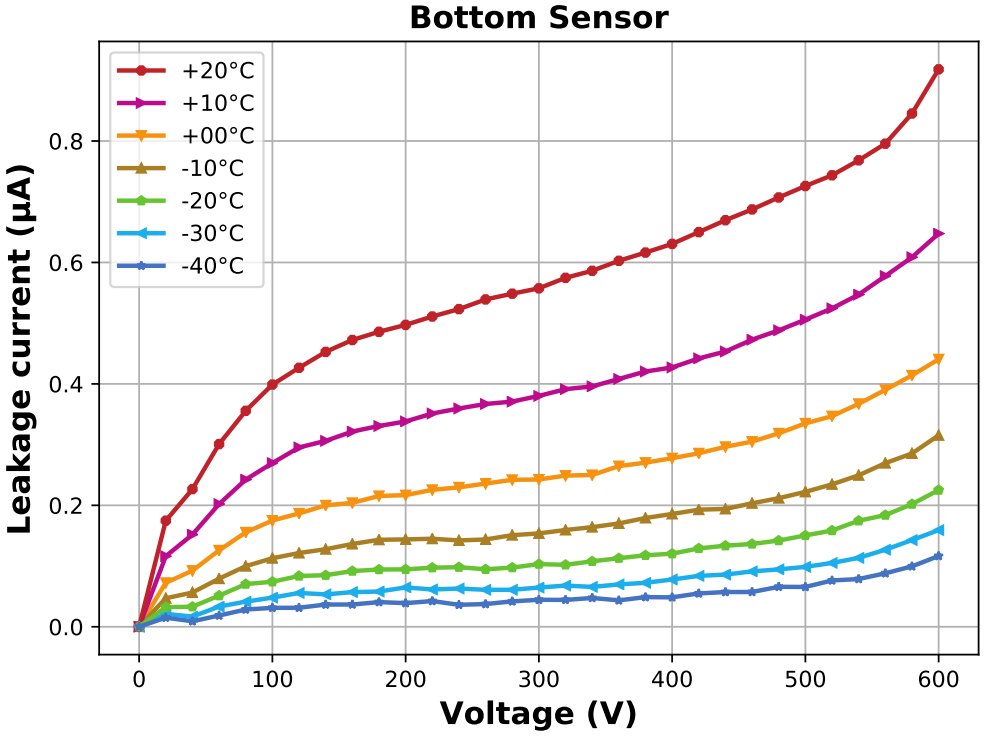

(b)

Figure 4.11.: I–V curves of the two 2S sensors used in the 8CBC2 module for different temperatures on the cooling jigs.

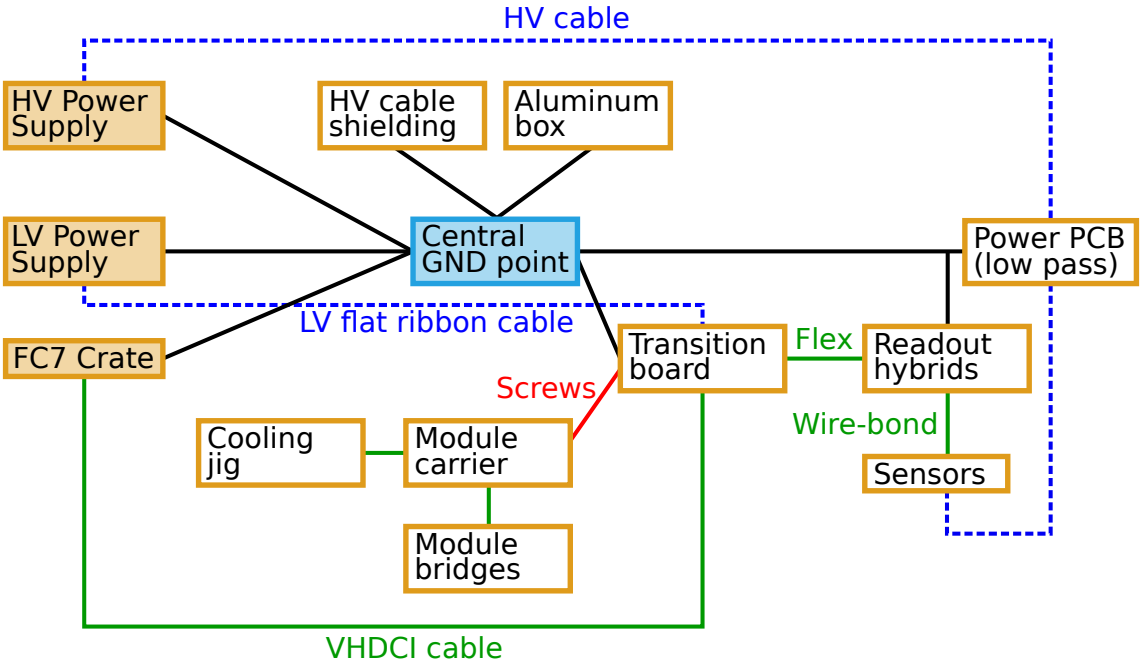

Figure 4.12.: Electrical connection schematic used in the 2S module functional test station in order to achieve low noise. Black lines symbolize grounding connections and blue lines represent high and low voltage transfer lines. Green connections cannot be changed.

marked in green symbolize fixed electrical connections which cannot be arranged differently. The black lines mark the installed grounding connections to minimize the module's noise inside the test setup. All grounding connections originate directly from one central ground point. Thus, internal loops in the schematics are avoided as far as possible, which largely reduces the noise level. Transition board and module carrier are connected via screws. For the 8CBC2 module described in this thesis, the screws are conductive which introduces an avoidable internal loop by changing to non-conductive screws. Nevertheless, it is possible to reach an average noise of $2.7\,\mathrm{V_{CTH}}$ on the eight CBCs of an 8CBC2 hybrid with this configuration. A distribution of the noise levels of all CBC channels can be found in Figure 4.13. Based on the calibration results presented in [Dee17], one V_{CTH} unit corresponds to approximately 320 electrons. Thus, the eight CBCs have an average noise of approximately 1000 electrons.

When the custom designed electronic circuit board used to read out the temperature sensors in the 2S module readout station is turned on, the noise level of all CBCs increases by approximately $0.5\,\mathrm{V_{CTH}}$. This effect has to be further investigated and eliminated to guarantee stable and reliable test procedures during the production phase of 2S modules.

The 2S module readout station allows the investigation of the temperature dependence of the readout chips' noise level. The average noise levels of all CBC channels on an 8CBC2 hybrid are summarized in Figure 4.13 as a function of the cooling jig temperature. For temperatures between $-10°\mathrm{C}$ and $20°\mathrm{C}$ the noise level slightly decreases with temperature by approximately $0.3\,\mathrm{V_{CTH}}$ and stays constant for lower temperatures. With respect to the statistical uncertainties, the noise level of the CBC does not show any large temperature dependence. Thus, it is possible to perform the temperature stabilized tests of 2S modules equipped with the second iteration of the CBC in the 2S module readout station at a low noise level over the whole temperature range expected in the CMS experiment.

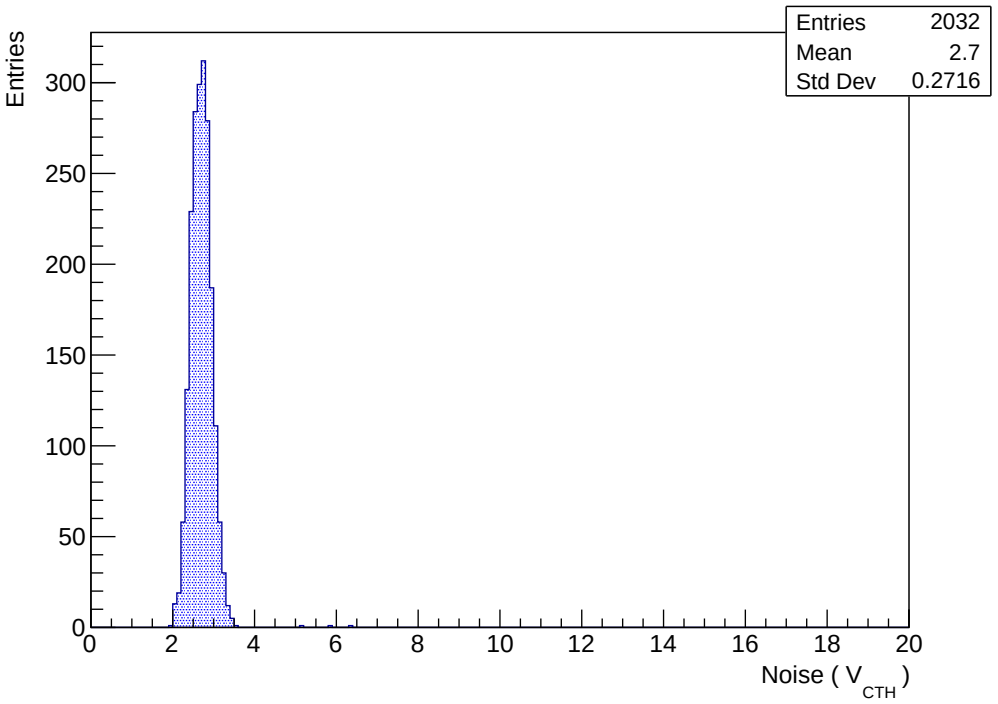

Figure 4.13.: Distribution of the measured noise levels on all channels of an 8CBC2 hybrid. The measurements are performed with the electrical connection schematic presented in Figure 4.12.

4.5.2.3. Charge Injection via a ^{90}Sr Source

A radioactive source can be used to check the functionality of the signal readout chain of a 2S module. By irradiating the module with a ^{90}Sr source, the emitted electrons generate electron-hole pairs in the two sensors. The charge can be collected at the strips and gets read out by the channels of the CBC each 25 ns. Counting the number of hits per strip during all trigger events leads to the distributions shown in Figure 4.15. Figure 4.15a summarizes the hits registered with a constant trigger rate of 1 kHz. As the radioactive source is placed above the upper sensor, the electrons interact with the top sensor material first. Thereby, they lose energy and are partially absorbed leading to a reduced hit rate in the lower sensor.

Regarding the hit pattern registered by the top sensor, three channels register substantially fewer hits than their adjacent channels. These channels provide a noise level between $4\,V_{CTH}$ and $7\,V_{CTH}$ and can be also identified in Figure 4.13. During the calibration procedure of the Ph2_ACF, these channels are registered as "noisy" channels and their offsets are set to the maximum value. Thus, these channels observe fewer hits than all other channels of the CBCs. To sum up, both test procedures (noise scan and charge readout) provide consistent results concerning the functionality of the strip readout and can be used during the production to check the functionality the modules.

As the electrons are emitted by the ^{90}Sr source inside a limited opening angle, the detected hit distribution possesses a maximum directly below the source's opening. In the adjacent strips, the number of hits decreases symmetrically as it is expected for this experimental arrangement. Regarding Figure 4.15a, the first and last two hundred strips cannot be reached by the electrons from the source. Nevertheless, these channels detect a constant number of events throughout the measurement. These events originate from two different background sources: cosmic muons traversing the module and random noise events in

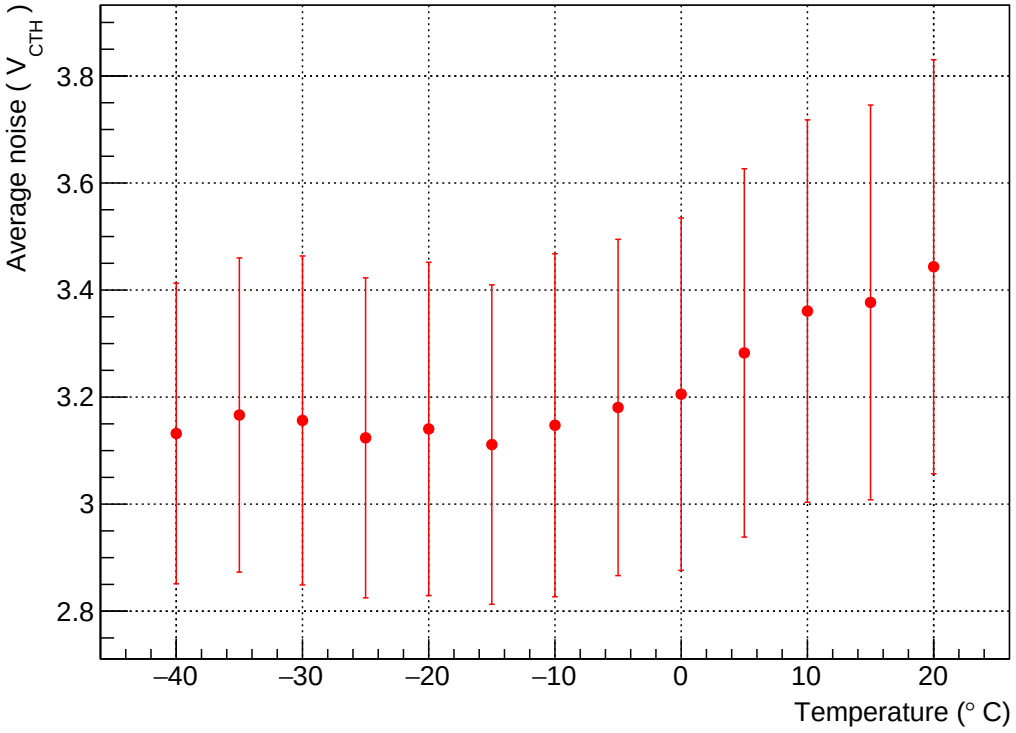

Figure 4.14.: Temperature dependence of the average noise levels on all channels of an 8CBC2 hybrid. The error bars indicate the standard deviation of the noise levels. The temperatures are measured on the copper cooling jig. The noise level is slightly increased when the electronic circuit board to read out the temperature sensors on the cooling jigs is turned on.

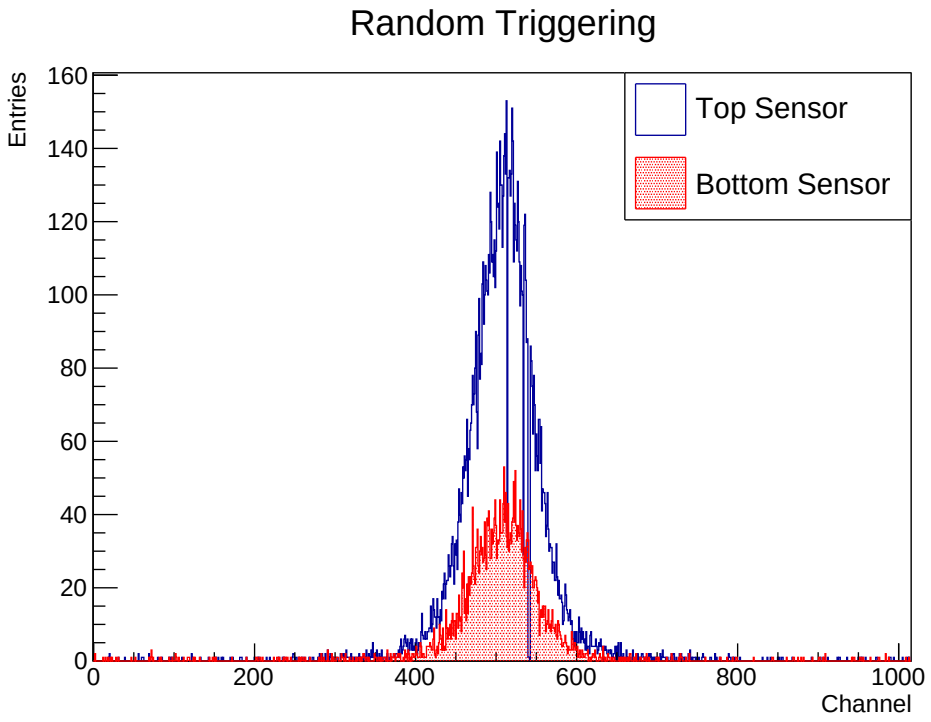

(a)

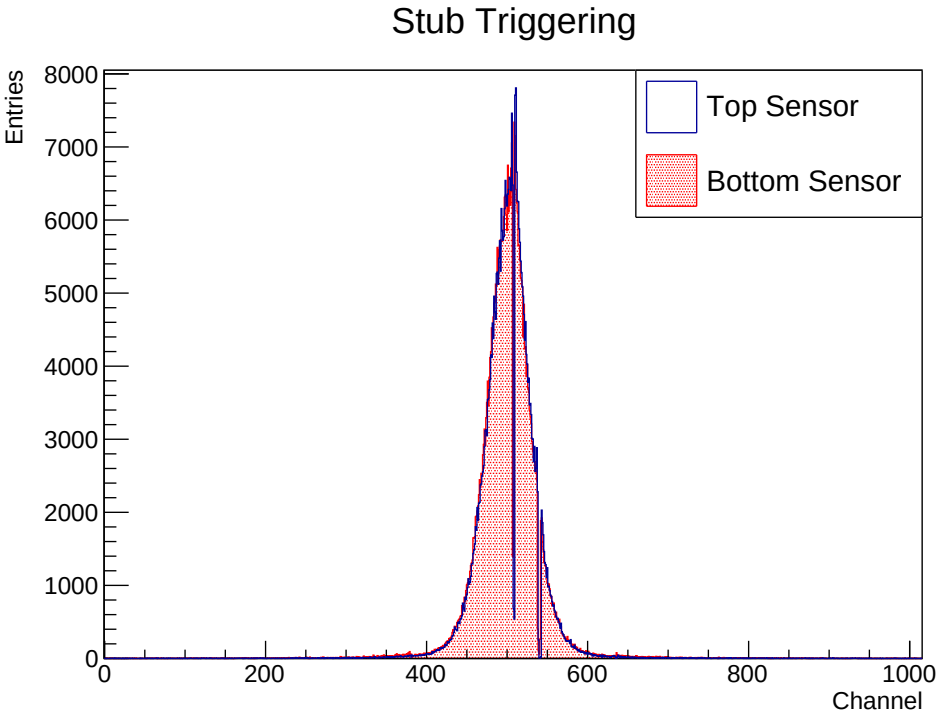

(b)

Figure 4.15.: Detected hit distribution for all channels of an 8CBC2 hybrid during irradiation with a ^{90}Sr source for different trigger sources. The readout with a constant trigger rate of 1 kHz is shown in (a). The data obtained by triggering on stubs is pictured in (b).

single strips. Compared with the signal of the ^{90}Sr electrons, the combined rate of these two processes is by a factor of approximately 70 smaller than the electron induced signal. Thus, these processes do not significantly influence the test performance to check the functionality of the strip readout.

A rudimentary test to check the performance of the CBC stub trigger can also be performed with a ^{90}Sr source. When triggered on stubs, the CBC is only read out if it has detected a stub. Therefore, the hit distributions in the two sensors shown in Figure 4.15b have the same number of events and a similar shape. The background rate is determined in the same way as before for random triggering. The background rate is by a factor of approximately 185 smaller than the ^{90}Sr signal rate. This improved separation of signal and background can be explained by the trigger mechanism as the CBC is only read out after a stub was detected. Thus, the probability to detect randomly occurring noise hits is reduced, as two of these hits have to occur in the same 25 ns long readout interval and in corresponding strips in the two sensors which lie inside the CBC acceptance window. More detailed studies about the stub trigger performance of CBCs of the second generation can be found in [Dro18].

4.6. The Module Readout and Cooling Framework

During the production of 2S modules it is necessary to simplify and automate the handling of test procedures as far as possible. Therefore, the *Module Readout and Cooling* (MoReCooling) software framework with graphical user interface (GUI) is developed to control the functionalities of the station for functional testing of 2S modules. The MoReCooling framework is developed using the Qt-5.6 development framework based on C++(11) and is accessible by members of CERN via GitLab[3].

The MoReCooling framework is organized in different subdirectories providing modules to operate the temperature control, start tests with the Ph2_ACF framework and plot, as well as a top level module to control all other modules. A short overview of the tasks of the three main subdirectories is presented in this chapter.

4.6.1. Temperature Control

The temperature on the two cooling jigs can be controlled by changing the electrical power of the Peltier devices. This needs to be a dynamic process in order to guarantee a temperature stabilization within a range of less than 1°C. Therefore, a proportional-integral-derivative (PID) algorithm is used to repeatedly calculate the voltage which will be applied to the Peltier devices. The voltage for each controlling step is calculated via

$$U(t) = K_p \cdot \Delta T(t) + K_i \cdot \int_0^t \Delta T(t')\mathrm{d}t' + K_d \cdot \frac{\mathrm{d}(\Delta T)}{\mathrm{d}t} \ , \tag{4.4}$$

where $\Delta T(t)$ is the temperature difference between the current average temperature on the two cooling jigs and the value of the previous controlling step. The combination of values of the coefficients K_p, K_i and K_d is adjusted manually in order to establish a fast temperature stabilization.

The software framework contains separate modules for the communication with the hardware devices. The temperature sensors are read out via an electronic circuit board which can be controlled by serial communication. Approximately every second this module sends its information to the PID controller which calculates the voltage for the Peltier devices. This voltage is transferred via serial communication to the power supply. The dew point is

[3] `https://gitlab.cern.ch/rkoppenh/MoReCooling`

measured using a 1-wire sensor which passes its data to the PID controller and to the module controlling the electrically controllable valve to regulate the dried air flux. A separate module is used to program and perform thermal cycles.

The status of the different devices can be controlled in the graphical user interface. The current values are displayed both as numbers and in a plot. Figure 4.16 illustrates the corresponding tab in the GUI.

4.6.2. Ph2_ACF Graphical User Interface

A graphical user interface to perform measurements with the Ph2_ACF framework has been developed and presented in [Dro18]. This stand-alone GUI is implemented with minor changes as an additional tab in the MoReCooling framework and can be used to start measurements on a 2S module and control the current status of the functional tests. Further information about the internal structure can be found in [Dro18]. In order to prepare the MoReCooling framework for the production phase, a graphical output of the Ph2_ACF test results still has to be integrated in this software module.

4.6.3. Top Level Tools

A customizable test procedure for 2S modules during the production needs the possibility to centrally control temperatures and the module readout. Thus, a top level module is implemented in the framework in order allow flexible and easy definition of measurement procedures. After defining the measurement sequence in a separate tab of the GUI, the steps are automatically processed by the program. Thus, it is e.g. possible to perform module calibrations and measurements of the leakage current at different temperatures or to check the functionality of a 2S module before, during and after thermal cycles without any need of additional human attendance. The software has to provide consistency checks of the defined measurement sequences before processing the single steps in order to guarantee reasonable and safe test procedures. This feature needs to be implemented to the software framework as soon as the functional test procedure of 2S modules during the production phase is completely defined.

Figure 4.17 illustrates the graphical implementation of the top level module in the MoReCooling framework. It is possible to save the steps of measurement sequences in configuration files and to load and combine different sequences. After starting a measurement sequence, an overview of the current status is displayed together with the output of the internal software logger. During a top level measurement the other tabs of the GUI are still accessible because the software is implemented as a multi-threading application.

In order to be used during the module production phase, the software needs an additional module to save the results of functional tests to a database.

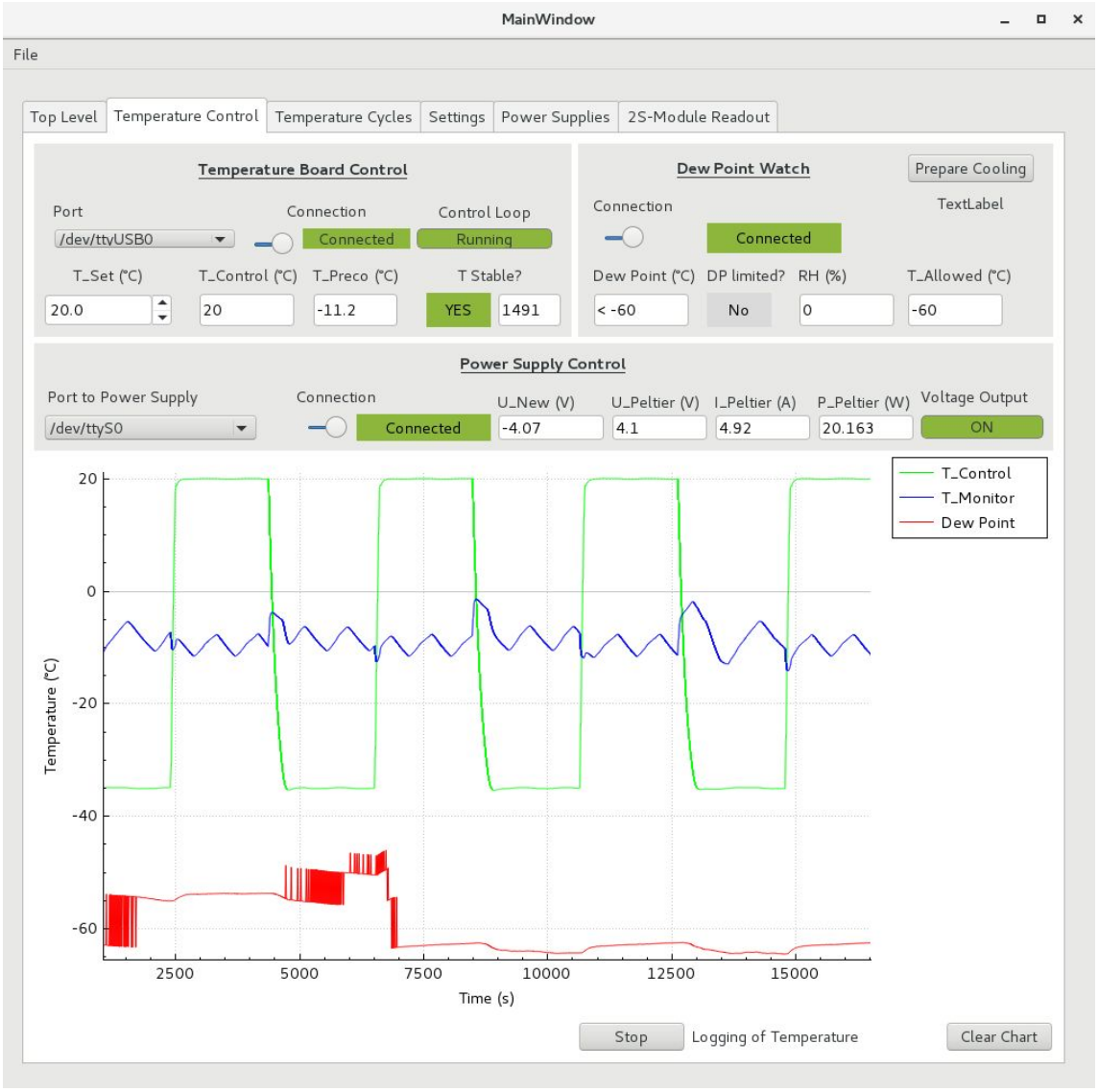

Figure 4.16.: Graphical interface to control the average temperature on the two cooling jigs of the 2S Module readout station. After successfully establishing connections to the temperature board, the 1-wire sensors and the power supply, a PID algorithm controls the voltage of the Peltier devices. The current temperatures are monitored and plotted.

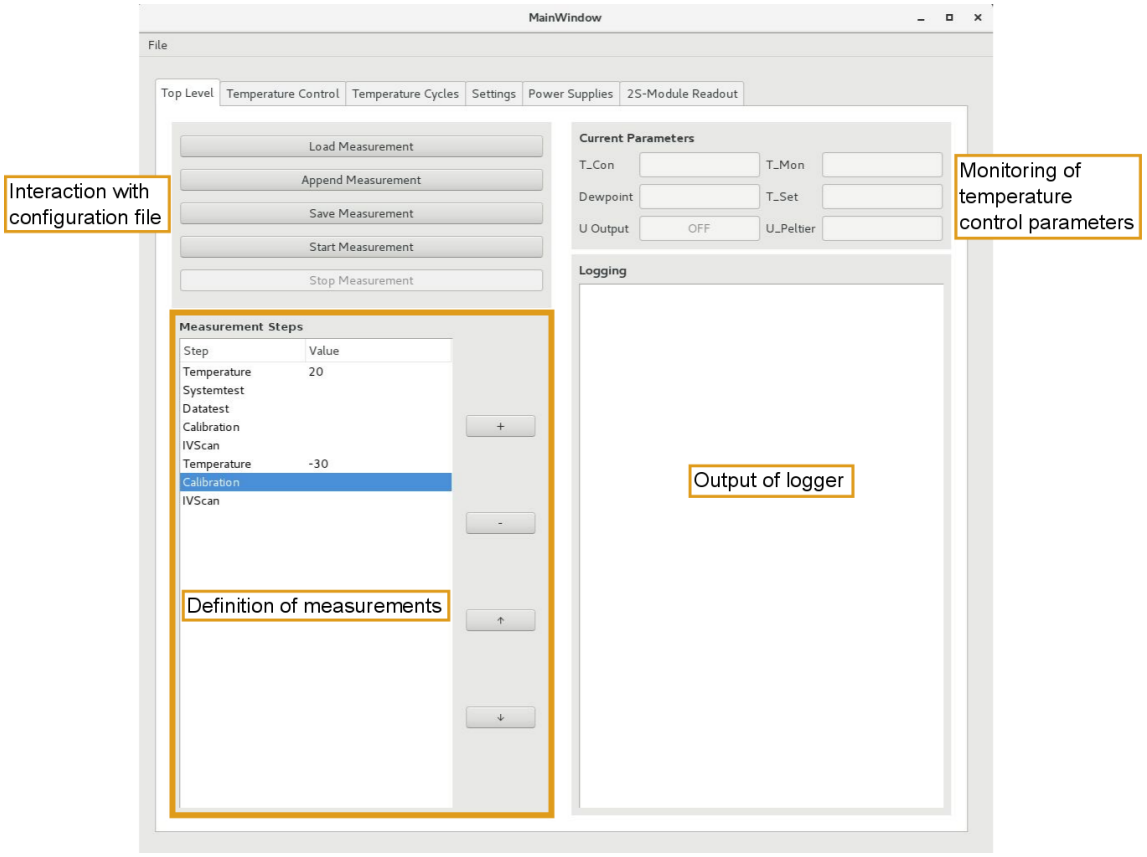

Figure 4.17.: Graphical implementation of the top level module, which allows defining a measurement sequence that will be automatically processed by the software. Measurement steps can be saved to a configuration file as well as loaded and combined. The top level module provides an overview of the current measurement status by highlighting the active step and displays logging messages.

5. The Sensor Long-Term Station

In the context of the Phase II Upgrade of the CMS experiment, the currently installed outer part of the silicon tracker will be replaced by a new one made of silicon sensor modules, called PS and 2S modules. Each of these modules consists of two parallel silicon sensors, which are used to detect particle transitions. As described in Chapter 3.1.2, these silicon sensors are operated in reverse bias mode in order to be sensitive to charge generation by interacting particles. Thus, the sensors have to be biased over the whole measurement period of the CMS detector. To guarantee stable and reliable operation, their properties and quality have to be studied in detail before the assembly process of 2S and PS modules can start. These studies are performed in the sensor qualification centers of the CMS community during the prototyping and production phase.

During the production of silicon sensor modules it is important to continuously check the quality of the sensors used in the assembly process. Therefore, one or two sensors per production batch (corresponding to about five to ten percent of the full quantity) are tested within the *Sensor Quality Control* (SQC) procedure before being used in the production process, as can be seen in Figure 3.4b. Only if these sensors have successfully passed the sensor qualification tests, the whole batch is used for module production. The CMS community has defined a preliminary set of electrical specifications in [CMS16] to qualify potential industrial sensor producers. For example, the sensors have to provide a constant leakage current I for continuous biasing over several hours. Quantitatively, this long-term stability is defined by the variation of the leakage current ΔI with respect to the mean current I. For the CMS Outer Tracker, the sensors have to fulfill the criterion

$$\left|\frac{\Delta I}{I}\right| < 30\% \tag{5.1}$$

over 48 hours at a bias voltage of 500 V [CMS16]. During such a measurement, the temperature has to be in the range of 22°C±4°C and the humidity level has to be stabilized below 50% relative humidity. These long-term sensor measurements will be performed by the sensor qualification centers in the CMS community for approximately one percent of the sensors used in the Outer Tracker module production [CMS17].

The *Institut für Experimentelle Teilchenphysik* (ETP) at the *Karlsruher Institut für Technologie* is one of the sensor qualification centers in the CMS community. ETP uses a dedicated station to perform the long-term tests, which is presented in this Chapter. This station is henceforth called sensor long-term station. Its experimental setup is discussed

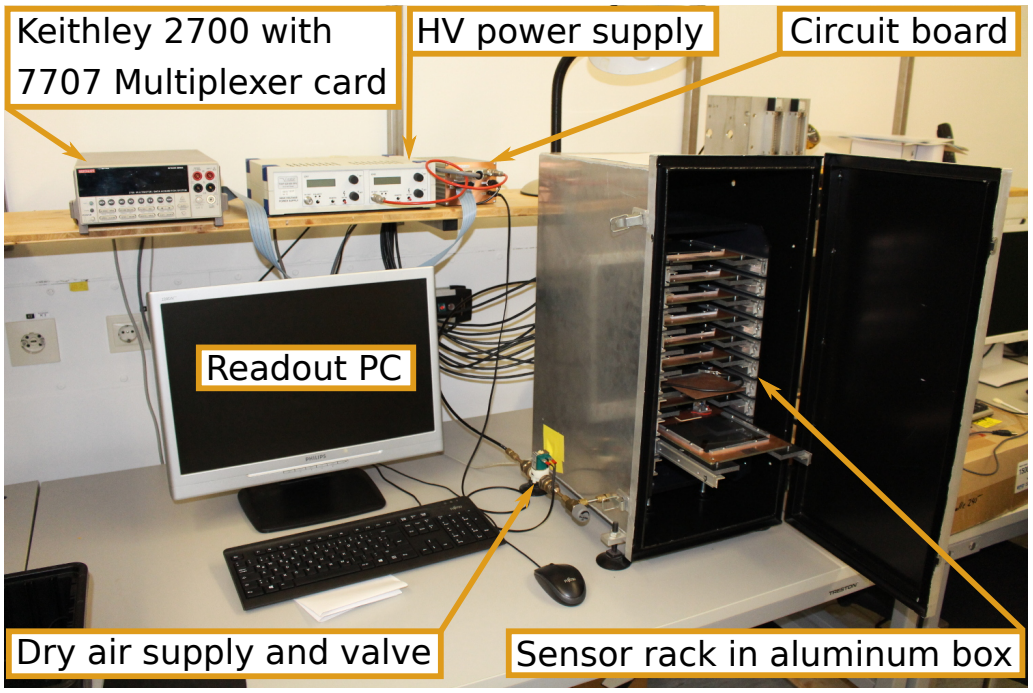

Figure 5.1.: Experimental setup of the sensor long-term station in the laboratory. Ten 2S sensors can be placed on copper plates inside a rack. The leakage current of each sensor is measured with a Keithley 2700 multimeter with an attached 7707 multiplexer card. A specially designed circuit board allows to disconnect each sensor individually from the high voltage. A remotely controllable valve is used to control the dried air flux into the aluminum box surrounding the sensor rack. The temperature and humidity level inside the box is measured via a 1-wire sensor placed on the fifth sensor layer in the rack.

in Chapter 5.1 and a summary of the first measurements performed during the setup of the station is presented in Chapter 5.2.

5.1. Experimental Setup

To verify the long-term stability of the 2S sensors' leakage current, a dedicated station is developed. The main requirements for such a station are:

- **Automated measurements:** An automated and unattended long-term measurement has to be implemented in order to simplify the test procedure during the production of 2S modules. Thus, it is important to continuously monitor the leakage current of all sensors and compare them to a global threshold. If one of the sensors' leakage currents exceeds this limit, the station has to automatically disconnect the affected sensor from the bias voltage. Afterwards, the station has to continue the measurements with the remaining sensors.

- **Control of temperature and humidity level:** As the leakage current of silicon sensors is dependent on temperature and humidity level, both quantities have to be monitored and stabilized during the measurements.

The experimental setup for a sensor long-term station is designed in such a way to fulfill these requirements. Figure 5.1 illustrates all components of the station, which will be further discussed in the Chapters 5.1.1 and 5.1.2.

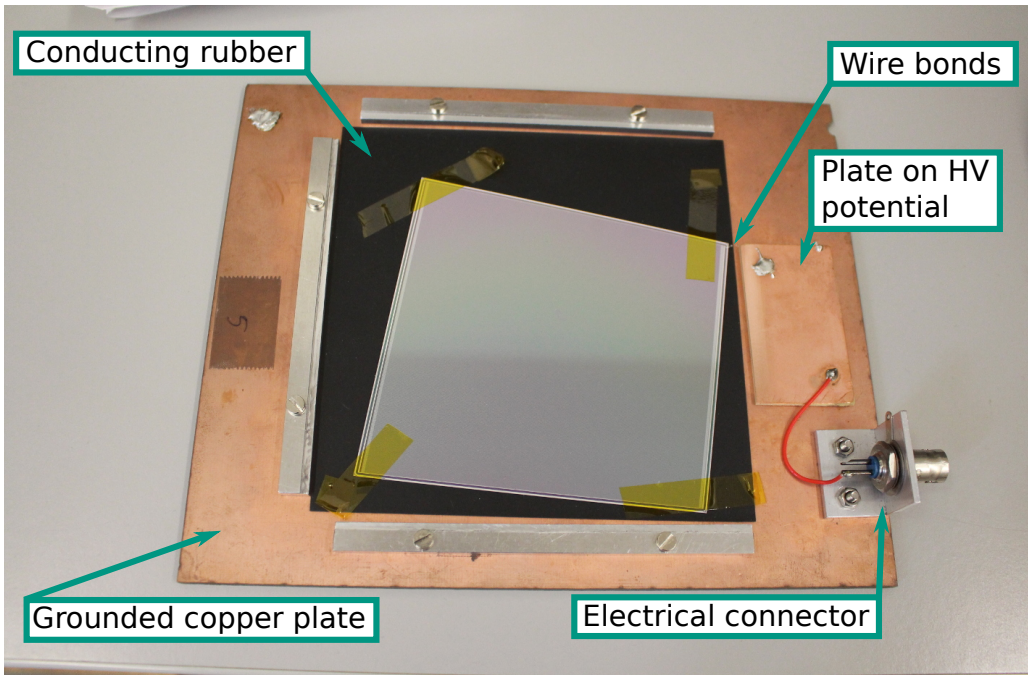

Figure 5.2.: To mount the sensors in the sensor long-term station, they are placed on a conducting rubber layer glued to a grounded copper plate. Wire-bonds are used to connect the sensor's bias ring with the high voltage potential. In preparation for the testing of 2S sensors during the 2S module production, the fixation with Kapton tape as it is depicted here will be replaced by a more suitable alternative which does not leave any residue on the sensor surface, e.g. a clamp surrounded by elastic foam.

5.1.1. Sensor Rack

To test the sensors, they are placed on a conducting rubber layer which is glued to a copper plate, as can be seen in Figure 5.2. In this configuration, the back side of the sensor is grounded via the copper plate. On top of the grounded copper plate, a second, smaller copper plate is mounted. These two plates are electrically insulated from each other. Thus, the high voltage is applied to the sensor's bias rail via wire-bonds between the sensor's topside and the smaller copper plate. In Figure 5.2, a wedge shaped sensor from the first silicon strip detector of the CMS experiment is fixed onto the rubber by Kapton tape. These sensors are used to test the functionality of the sensor long-term station in the context of this thesis. In order to test 2S sensors during the 2S module production, the geometry of the copper plate has to be adapted to the size of the sensors. Additionally, a reversible fixation mechanism has to be designed which prevents the sensor from being damaged and does not leave any residue on the sensor surface. This can, e.g., be realised with a clamp surrounded by elastic foam which is mounted above the sensor and presses it onto the rubber.

After mounting the sensors on the copper plates, each plate can be inserted into a telescopic mounted layer in a rack as depicted in Figure 5.1. In total, there are ten telescopic layers and ten corresponding copper plates. By sliding the layers into the rack, the electrical connectors on each copper plate are plugged into their counterpart, which is mounted at the back side of the rack. A detailed view of the rack and the connectors can be found in Figure B.1 in the appendix.

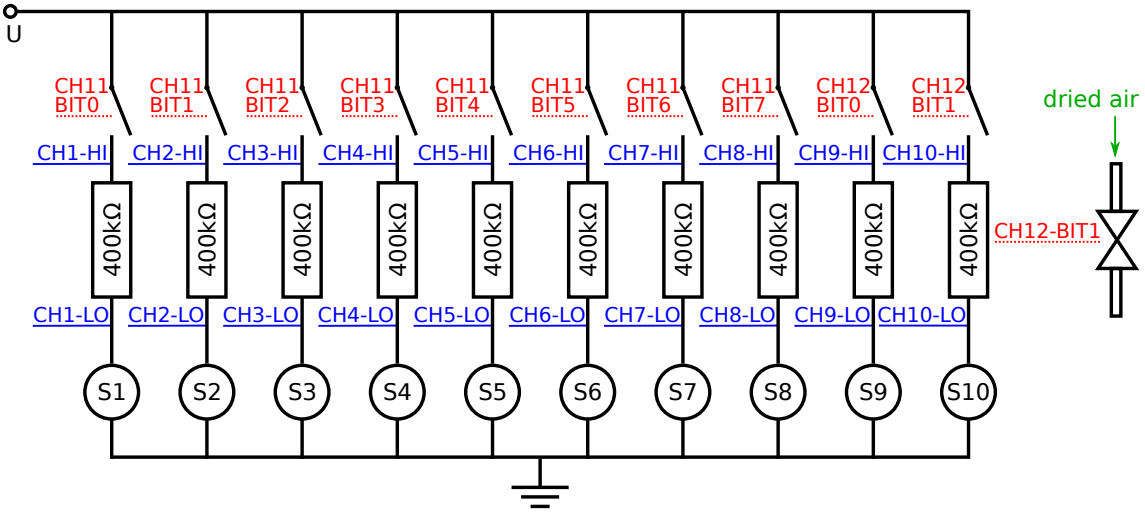

Figure 5.3.: Schematic of the electronic circuit used to operate the sensor long-term station. The ten sensors are biased in a parallel circuit. By measuring the voltage drop at a 400 kΩ resistor, the leakage current of each sensor can be determined. This measurement will be performed by the analog inputs of a *Keithley 7707 Multiplexer Card*. Electrical switches allow disconnecting each sensor from the bias voltage and are controlled by the digital output channels of the card. An additional digital output channel is used to control the dried air flux into the station via a remotely controllable valve.

5.1.2. Electronic Circuit Board

To allow automated measurements as described at the beginning of Chapter 5.1, an electronic circuit board was designed to control the connections between the high voltage power supply, the multimeter and the sensors. The high voltage is delivered by a power supply of the company *Iseg Spezialelektronik GmbH*. To measure the leakage current of each sensor a *Model 2700 Multimeter/Switch System* of the company *Keithley Instruments Inc.* is used. This multimeter can be equipped with a *Model 7707 Multiplexer Card* providing ten analog input channels which can be connected to the multimeter. Additionally, the multiplexer card offers 32 digital configurable input/output (I/O) channels.

Based on this hardware, the electronic circuit presented in Figure 5.3 was developed. The ten sensors are operated in a parallel circuit to allow individual measurements of the leakage current. As the multimeter in combination with the multiplexer card only allows voltage measurements, the leakage current can be determined by measuring the voltage drop at a 400 kΩ resistor (providing an accuracy of ±5%) using the analog inputs of the card. Ten of the 32 digital I/O channels are used to control the status of electrical switches which can each disconnect one sensor from the bias voltage. Another I/O channel controls the status of a valve allowing dried air to enter the setup.

A specially designed electronic circuit board houses the resistors and switches and allows connecting the analog and digital channels with the multiplexer card. An overview of the external connectors of the circuit board can be found in Figure B.2 in the appendix.

5.1.3. Control Framework

To perform the long-term measurements, a command line software framework was developed, which is based on Python 3. A graphical representation of the software modules and their interaction can be found in Figure 5.4. The source code can be accessed by members

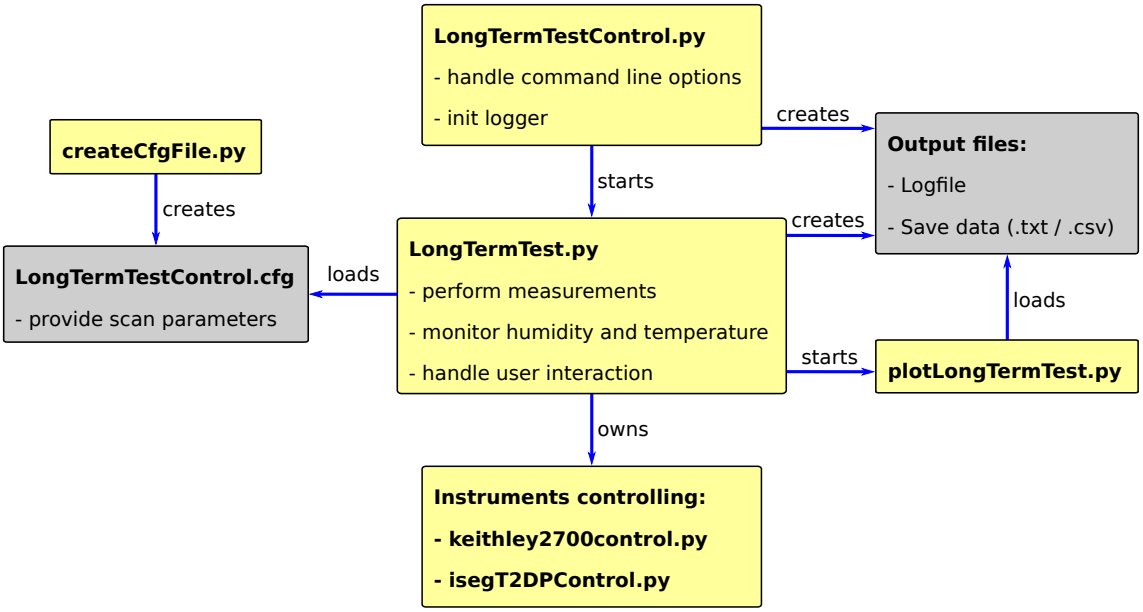

Figure 5.4.: Graphical representation of the software modules used to control the sensor long-term station. The configuration parameters to control a measurement are stored inside a configuration file, which is read out at the start of the main software module *LongTermTest.py*. Due to the multi-threading architecture of the software, it is possible to interact with the program during runtime.

of CERN via GitLab[1].

To start the framework, *LongTermTestControl.py* has to be executed, which accepts command line options and initializes the software logger. The main module *LongTermTest.py* is started internally performing the measurement by controlling the modules for serial communication with the Keithley 2700 multimeter and the Iseg high voltage power supply, monitoring humidity level and temperature inside the aluminum box and handling possible user inputs during the runtime. The control parameters are stored in a separate configuration file, which can be manipulated by the user before starting the framework. An overview of the available parameters is given in Table B.1 in the appendix.

In order to allow user inputs during runtime and monitor the correct functionality of all software modules, the framework operates with four parallel threads. One thread is used to coordinate the measurement progress by triggering the leakage current readout, comparing the measured values with the user defined global threshold and saving the results to a file. When the measured current of one sensor exceeds the allowed threshold, the high voltage of all sensors is ramped down, the corresponding shutter is opened in order to disconnect the sensor from the bias voltage and the scan is continued with the remaining sensors when the bias voltage is established again. In order to avoid these voltage ramps, additional capacitors can be added to a future version of the electronic circuit board. By mounting one capacitor in parallel to each of the ten combinations of resistors and sensors, it is possible to disconnect a sensor from the bias voltage by opening the corresponding shutter. The bias voltage is then ramped down automatically during the discharge of the capacitor. A schematic of this extended electronic circuit board is shown in Figure B.3 in the appendix.

A second thread continuously monitors and logs the humidity level and temperature inside the aluminum box using a 1-wire sensor placed on the fifth layer of the sensor rack. A remotely controllable valve is used to stabilize the relative humidity level around a desired

[1] `https://gitlab.cern.ch/rkoppenh/LongTermControl.git`

value. By opening the valve, the aluminum box is filled with dried air and the humidity level in the station decreases. When the humidity level reaches values below the desired level, the valve is closed and the relative humidity inside the box rises due to leaks in the aluminum housing. The valve gets re-opened when the desired humidity level is exceeded.

A third thread is used to allow user interaction during runtime. Thus, it is possible to stop a long-term measurement or to request a plot of the already measured data. The module *plotLongTermTest.py* is started internally.

A fourth thread is needed to continuously control the correct functionality of the other threads. In case one of the other threads has stopped unexpectedly, the measurement is stopped immediately and the high voltage is ramped down. The software framework additionally allows sending an email notification to a configurable address to inform the user about the premature ending of the measurement.

A common database for the CMS Outer Tracker community is currently under development. As soon as this work is finished, a software module needs to be added to the framework, which can save the results of long-term sensor measurements to this database.

5.2. Results

To characterize the performance of the sensor long-term station, some measurements with resistors and silicon strip sensors are done, which are presented in the following.

5.2.1. Electronic Noise

To determine the noise level induced by the readout electronics, a 10 MΩ resistor is used. This resistor is temporarily soldered on one of the copper plates and connects the high voltage potential with the grounded copper plate. The operating voltage is 7 V in order to produce a current in the range of 1 µA. Thus, the multimeter is operated with the same sensitivity as during measurements with silicon sensors. Figure 5.5 summarizes statistical fluctuations of the current around the global mean during this noise measurement. The data follows a Gaussian distribution with a standard deviation $\sigma = 0.12\,\text{nA}$. This resolution is sufficient to investigate the long-term stability of the leakage current of 2S sensors, which are typically in the order of several hundreds of nanoampere at room temperature.

5.2.2. Long-Term Measurements

The performance of the sensor long-term station is characterized by measurements with silicon strip sensors, which have the same geometry as the ones used in the first silicon tracker of the CMS experiment. To analyze these measurements, it is crucial to monitor the humidity and temperature levels inside the station in order to check for the long-term stability defined in Equation 5.1.

5.2.2.1. Stability of Temperature and Humidity Levels

Figure 5.6 illustrates the dependence of the leakage current on the humidity level. The rise in the relative humidity from approximately 35% to 46% correlates with an increase of the leakage current. To minimize this effect, the humidity level in the station is stabilized using the remotely controllable valve. With this configuration, it is possible to stabilize the relative humidity inside the station in a range of ±2% around a configurable level. The results of a humidity stabilized long-term measurement over 24 hours can be found in Figure B.4 in the appendix.

As the station cannot actively stabilize the temperature, it is important to continuously monitor the temperature values in order to investigate the correlation between possible

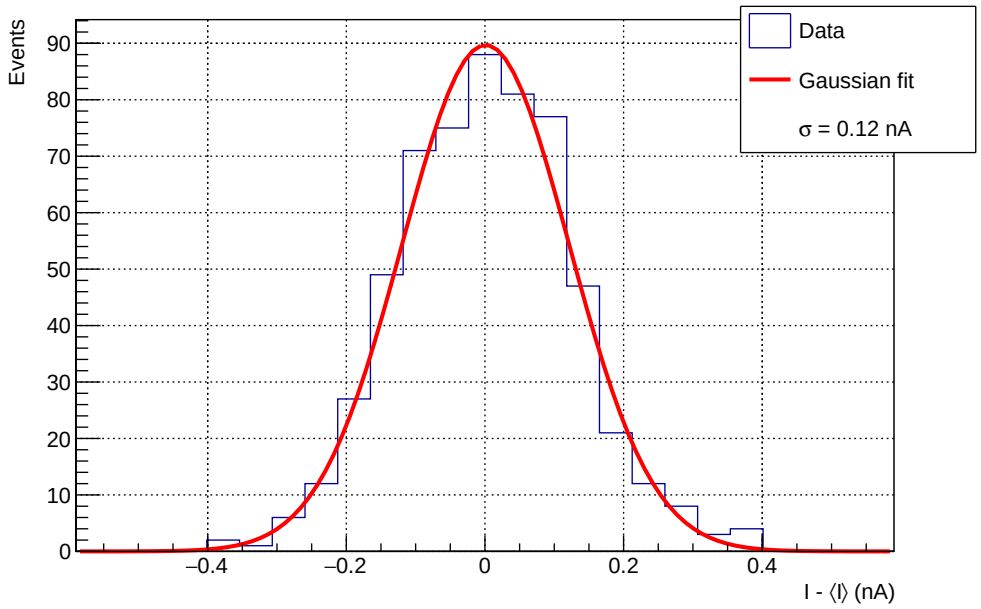

Figure 5.5.: Summary of the current fluctuations around the average value during a long-term measurement with a 10 MΩ resistor to determine the electronic noise of the sensor long-term station. The resulting statistical fluctuations with a standard deviation of $\sigma = 0.12$ nA are sufficiently small to investigate the long-term stability of 2S sensors, which have leakage currents above 500 nA.

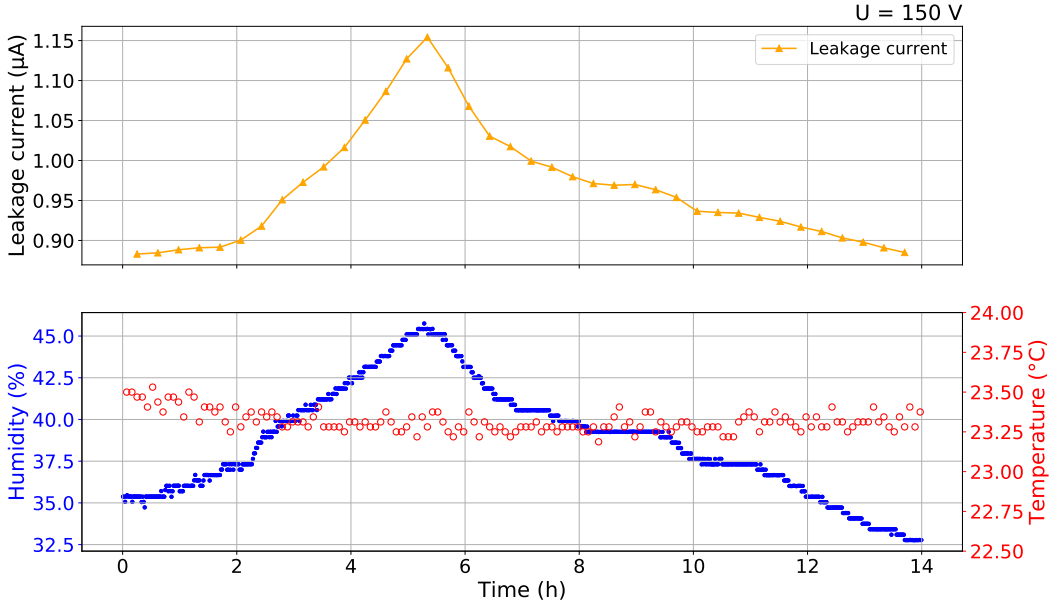

Figure 5.6.: Long-term measurement of the leakage current of a silicon strip sensor compared to the temperature and relative humidity levels inside the sensor long-term station. During this measurement, the temperature stays stable at approximately 23.3°C ± 0.1°C. The changes in the humidity level between approximately 35% and 46% correlate with the leakage current distribution.

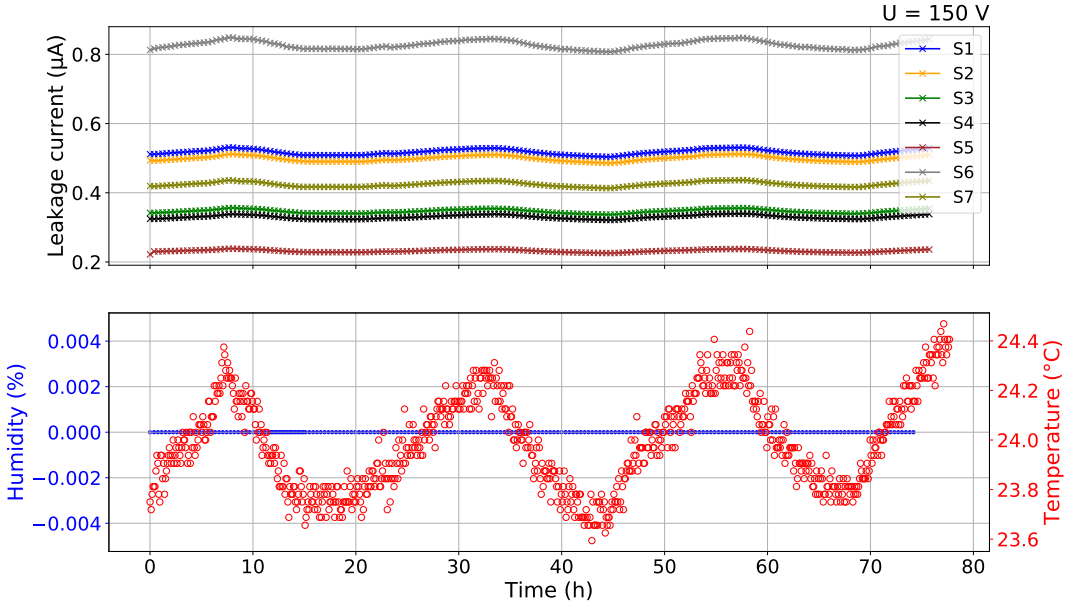

Figure 5.7.: Temperature dependence of the sensors' leakage current at a constant relative humidity level below the resolution limit of the 1-wire sensor, which is, therefore, monitored as 0%. The temperature oscillations follow the day and night fluctuations and are in the order of ±0.5°C.

changes in the leakage currents and temperature variations. Figure 5.7 illustrates a long-term measurement of seven sensors over 72 hours with a bias voltage of 150 V. During this measurement, the dried air supply into the aluminum box stayed opened. This leads to a stable relative humidity level below the resolution limit of the 1-wire sensor, which is monitored as 0%. The recorded air temperature in the station oscillates slightly in an approximate range of ±0.5°C following the day and night fluctuations. These temperature oscillations are correlated with fluctuations in the measured current distributions of all sensors, which can be quantified as relative fluctuations of

$$\frac{\Delta I}{I} \leq 7.5\% \ . \tag{5.2}$$

5.2.2.2. Long-Term Stability

After each long-term measurement, the data has to be analyzed in order to check if the requirements for the long-term stability are reached by each sensor. This analysis is performed for the dataset presented in Figure 5.7. As discussed in the previous section, changes in the air temperature influence the leakage current of the silicon sensors. To perform an analysis of the long-term behavior of the leakage current, these temperature induced current fluctuations have to be excluded. As introduced in Chapter 3.3.2, the temperature dependence of the leakage current can be described by Equation 3.3. Thus, the measured leakage currents of each sensor can be scaled from their measured temperature level T_m to a common temperature level T_c by

$$I(T_c) = I(T_m) \cdot \left(\frac{T_c}{T_m}\right)^2 \cdot \exp\left[\frac{1.21\,\mathrm{eV}}{2k_\mathrm{B}}\left(\frac{1}{T_m} - \frac{1}{T_1}\right)\right] \ , \tag{5.3}$$

where k_B is the Boltzmann constant. To evaluate the long-term criterion following Equation 5.1 the scaled current values are summarized for each sensor in a histogram and the

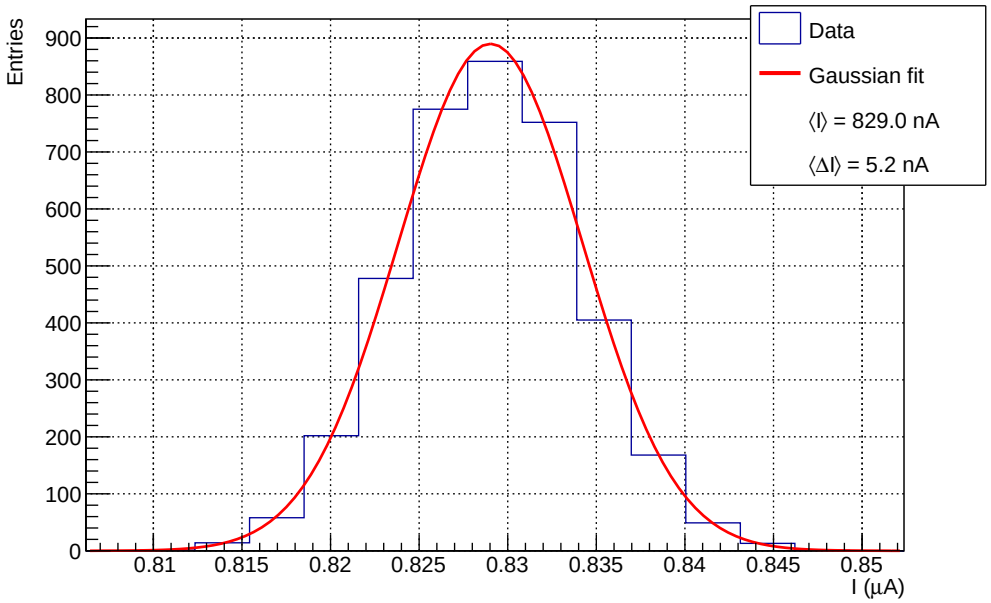

Figure 5.8.: Histogram of the temperature corrected leakage current fluctuations I of sensor *S6* during the long-term measurement presented in Figure 5.7.

average leakage current $\langle I \rangle$ and its standard deviation $\Delta\langle I \rangle$ is determined using a Gaussian fit. The result obtained for the sixth sensor depicted in Figure 5.7 (named *S6* within this thesis) is plotted in Figure 5.8. This sensor shows a current variation of $\langle \Delta I \rangle = 5.2\,\text{nA}$. Table 5.1 summarizes the results for all seven sensors. In addition, the long-term stability criterion is evaluated using Equation 5.1. This fraction is smaller than one percent for all seven sensors. Thus, these sensors fulfill the long-term stability criterion demanded from the sensors for the Phase II Upgrade of the CMS Outer Tracker.

5.2.3. Sensor Biasing via Needles

During the setup of the sensor long-term station, an alternative bias connection for the sensors has been investigated. Instead of wire-bonds, a bias needle is used to provide an electrical contact between high voltage potential and the bias ring. This configuration

Table 5.1.: Summary of the mean leakage current and leakage current variations for the dataset presented in Figure 5.7. All seven sensors fulfill the long-term stability criterion of the CMS experiment for sensors for the Phase II Upgrade, which currently is $|\Delta I/I| > 30\%$.

Sensor	$\langle I \rangle$ (nA)	$\langle \Delta I \rangle$ (nA)	$\lvert\langle \Delta I \rangle / \langle I \rangle\rvert$ (%)
1	518.1	3.1	0.6
2	499.6	3.1	0.6
3	346.9	2.3	0.7
4	330.5	2.2	0.7
5	232.2	1.7	0.7
6	829.0	5.2	0.6
7	425.4	2.4	0.6

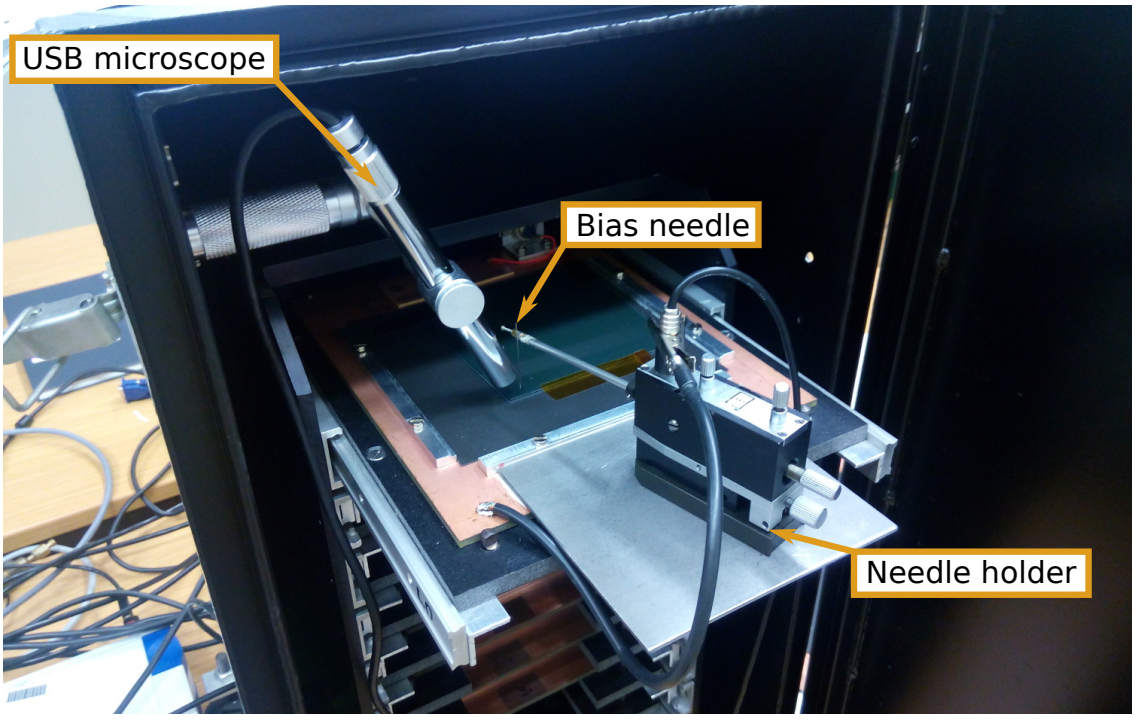

Figure 5.9.: Experimental setup to bias a silicon sensor in the sensor long-term station using a tungsten bias needle. The positioning of the needle fixed in a needle holder can be checked by a microscope above the sensor.

can be used by sensor qualification centers without a bonding machine. The experimental setup is pictured in Figure 5.9. The bias needle is made of tungsten and has a tip radius of 7 µm. It is mounted on the level arm of a needle holder which allows positioning the needle above the bias ring. By lowering the needle onto the sensor surface, the sensor gets biased. The correct positioning of the needle can be controlled using a comparatively inexpensive USB microscope of the company *Shenzhen Andonstar Tech*[2]. Figure B.5 illustrates the view of the microscope after connecting the needle with the sensor.

To compare the the two bias connections, the same sensor is measured repeatedly, first with a bias connection by wire-bonds and then via a needle. The results are summarized in Figure 5.10. As expected, the two distributions reach the same leakage current after approximately ten minutes of biasing. For smaller times, the measurements show a slightly different behavior. This effect is not related to the different biasing methods but can be related to the sensor's history, as old sensor material from the first silicon tracker in the CMS experiment was used for this test, which was stored unused for several years at ETP. Thus, the two different bias connections provide both a sufficient electrical contact to perform long-term measurements.

In order to use the sensor long-term station with bias needles during the production phase of 2S modules, it is necessary to design an appropriate geometry to arrange the copper plates. The sensor rack as presented in Chapter 5.1.1 does not provide enough stability in order to place the bias needles vibration-free and guarantee good electrical contact to the sensors' bias line while moving the rack layers. Additionally, a movable holder for the microscope has to be designed in order to accelerate the placement procedure of the bias needles.

[2]A datasheet can be found in Appendix B.6

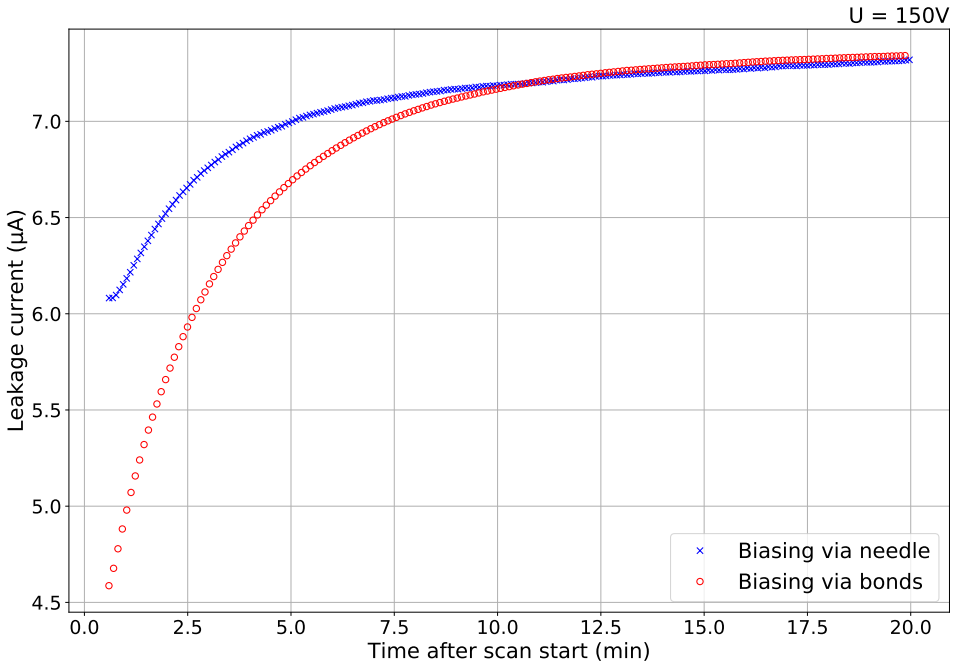

Figure 5.10.: Development of the leakage current as a function of time for two different biasing methods. In a first measurement, the bias voltage is applied via bonds, afterwards a bias needle is connected to the sensors bias ring. Regarding the long-term behavior, both methods result in the same leakage current.

6. Conclusion and Outlook

In order to fully exploit the potential for physics discovery of the Large Hadron Collider, it is planned to upgrade the accelerator and its experiments in the 2020s to prepare them for the High Luminosity LHC. During the CMS Phase II Upgrade, the whole CMS silicon tracker will be replaced. The new CMS Outer Tracker will consist of two types of silicon sensor modules called 2S and PS modules, which will be assembled by institutes of the CMS collaboration. In the course of this thesis, two test stations have been developed and commissioned to be used during the 2S module production: the sensor long-term station and the 2S module readout station. The sensor long-term station will bias 2S sensors over several hours and monitor their leakage current stability before the sensors are used in the module assembly process. At the end of each assembly process, the finalized modules are checked for their functionality using the 2S module readout station.

The 2S module readout station provides a powerful two stage cooling unit to allow tests of the modules under the future thermal conditions in the CMS Outer Tracker. The first cooling stage is formed by a chiller operating a liquid based coolant circuit to stabilize the temperature of a copper block at $-10°C$. Four Peltier devices are mounted on top of this copper block to dynamically control the temperature of two additional copper cooling jigs mounted above the Peltier devices. A PID controller is used to control the electrical power of the Peltier devices in order to stabilize the temperature on the two cooling jigs within a range of less than $\pm 0.5°C$ around the desired temperature. The required thermal power of this cooling system has been determined using thermal simulations and its thermal performance has been successfully proven by measurements with heating resistors inside the station. The minimal reachable temperature on the cooling jigs is $-45°C$. Thus, it is possible to reach the temperatures of the CO_2 coolant in the CMS experiment of $-35°C$ and to investigate the influence of thermal stress on the 2S modules by performing thermal cycles.

In view of its frequent use during module production, the station provides an easy and quick fixation mechanism for the 2S modules, which is based on four springs fixed in a rotatable aluminum frame. During the functional tests it is possible to fix a radioactive source below and above the module. A plastic scintillator mounted below the module can be used for detection efficiency studies. To control and simplify the test procedure during the module production, the *Module Readout and Cooling* (MoReCooling) software framework has been developed. This framework controls the temperature on the cooling jigs, monitors the humidity level inside the station and allows the communication with 2S modules via the *Phase 2 Acquisition and Control Framework* developed by the CMS community. The

MoReCooling framework provides a top level module to simplify automated functional tests during the 2S module production. As soon as a detailed test procedure for the functional tests of 2S modules is defined by the CMS community, the software framework can be finalized for its usage during the 2S module production.

The 2S module readout station has been successfully commissioned by performing basic functional tests with a prototype module. A low noise level of the readout chips of approximately 2.7 V_{CTH} (corresponding to approximately 1000 electrons) was achieved by using appropriate ground connections. The noise level shows no significant temperature dependence. Nevertheless, the unexpected increase in the noise level when the custom designed electronic circuit board to readout the temperature sensors in the 2S module readout station is turned on, needs to be further investigated and eliminated before the module production starts. Using a radioactive source, it is possible to check the functionality of the signal readout chain of all strips on a 2S module.

Before a 2S module can be assembled, the single components have to be checked to guarantee their full functionality. The CMS collaboration has defined electrical specifications for the silicon sensors used during the module production. One of these specifications is the long-term stability of the leakage current. In order to test a fraction of the 2S sensors used in the module production for their long-term stability, an appropriate test station has been commissioned in the course of this thesis. The 2S sensors can be placed on custom designed copper plates, where they can be biased via wire-bonds or bias needles. For the long-term measurement, up to ten sensors are placed inside an aluminum box and their leakage current distribution is measured over up to 72 hours. Meanwhile, the relative humidity level inside the station is stabilized within a range of approximately $\pm 2\%$ around a configurable value. To control the long-term measurement, a command line-based program and a specially designed circuit board is used, which allows disconnecting sensors from the bias voltage during runtime if their leakage currents exceed a global threshold. The station's functionality has been successfully tested using silicon strip sensors with the same geometry as the ones used in the first CMS silicon tracker. To finally commission the sensor long-term station, the geometry of the copper plates needs to be adapted to the size of 2S sensors. Additionally, a software module needs to be added to the command line based program allowing to save results of long-term measurements to a database of the CMS community.

To sum up, the 2S module readout station and the sensor long-term station have been successfully commissioned in the course of this thesis and have proven their functionality to be used during the 2S module production.

Bibliography

[ANS17] ANSYS Inc. *ANSYS® Academic Research, Release 17.2*. 2017.

[Apo+15] G. Apollinari et al. *High-Luminosity Large Hadron Collider (HL-LHC): Preliminary Design Report*. CERN Yellow Reports: Monographs. Geneva: CERN, 2015. URL: https://cds.cern.ch/record/2116337.

[ATL12] ATLAS Collaboration. *Observation of a new particle in the search for the Standard Model Higgs boson with the ATLAS detector at the LHC*. In: Physics Letters B 716.1 (2012), pp. 1–29. ISSN: 0370-2693. DOI: https://doi.org/10.1016/j.physletb.2012.08.020.

[Ben+04] M. Benedikt et al. *LHC Design Report Volume 3: the LHC Injector Chain*. CERN Yellow Reports: Monographs. Geneva: CERN, 2004. URL: https://cds.cern.ch/record/823808.

[Bra13] D. Braga. *CBC2 (CMS Binary Chip 2) User Guide 1.1*. Mar. 2013. URL: http://www.hep.ph.ic.ac.uk/~dmray/CBC_documentation/CBC2_User_Guide_v1.1.doc.

[Brü+04] O. S. Brüning et al. *LHC Design Report Volume 1: the LHC Main Ring*. CERN Yellow Reports: Monographs. Geneva: CERN, 2004. URL: http://cds.cern.ch/record/782076.

[Chi13] A. Chilingarov. *Temperature dependence of the current generated in Si bulk*. In: Journal of Instrumentation 8.10 (2013), P10003. URL: http://stacks.iop.org/1748-0221/8/i=10/a=P10003.

[CMS08] CMS Collaboration. *The CMS experiment at the CERN LHC*. In: Journal of Instrumentation 3.08 (Aug. 14, 2008), S08004. DOI: 10.1088/1748-0221/3/08/S08004.

[CMS12] CMS Collaboration. *Observation of a new boson at a mass of 125 GeV with the CMS experiment at the LHC*. In: Physics Letters B 716.1 (2012), pp. 30–61. ISSN: 0370-2693. DOI: https://doi.org/10.1016/j.physletb.2012.08.021.

[CMS16] CMS Collaboration. *Planar Silicon Sensors for the ATLAS and CMS Outer Tracker Upgrades*. 2016. URL: https://cds.cern.ch/record/2145271 (visited on 08/02/2018).

[CMS17] CMS Collaboration. *The Phase-2 Upgrade of the CMS Tracker*. CERN-LHCC-2017-009. CMS-TDR-014. Geneva: CERN, June 2017. URL: http://cds.cern.ch/record/2272264.

[CMS97a] CMS Collaboration. *The CMS electromagnetic calorimeter project: Technical Design Report*. Technical Design Report CMS. Geneva: CERN, 1997. URL: http://cds.cern.ch/record/349375.

[CMS97b] CMS Collaboration. *The CMS hadron calorimeter project: Technical Design Report*. Technical Design Report CMS. CERN, 1997. URL: http://cds.cern.ch/record/357153.

[Dee17] N. Deelen. *Calibration of a minimodule*. Phase 2 Outer Tracker System Test & DAQ Meeting during Phase2 Days. Mar. 2017. URL: https://indico.cern.ch/event/614309.

[Dem18] W. Demtröder. *Mechanik und Wärme*. 8. Auflage. Berlin, Germany: Springer Spektrum, 2018. ISBN: 978-3-662-54846-2 and 3-662-54846-1.

[Dom+12] A Dominguez et al. *CMS Technical Design Report for the Pixel Detector Upgrade*. CERN-LHCC-2012-016. CMS-TDR-11. Sept. 2012. URL: https://cds.cern.ch/record/1481838.

[Dro18] A. Droll. *Characterization and Performance Study of Prototype Modules equipped with the CMS Binary Chip*. Master thesis. Karlsruher Institute of Technology, 2018. URL: https://ekp-invenio.physik.uni-karlsruhe.de/record/49038.

[Eve] Everredtronics Limited. *Thermoelectric Peltier module TEC1-12705T125*. URL: http://www.everredtronics.com/thermoelectric.TEC1.html (visited on 08/02/2018).

[Fry] Fryka-Kältetechnik GmbH. *Recirculating chiller ULK 2002*. URL: https://www.fryka.de/en/standard-equipment/recirculating-chillers/recirculating-chiller-ulk-2002 (visited on 08/02/2018).

[GM12] R. Gross and A. Marx. *Festkörperphysik*. Gruyter, Walter de GmbH, 2012. ISBN: 9783486714869. URL: http://www.ebook.de/de/product/21612761/rudolf_gross_achim_marx_festkoerperphysik.html.

[Har17] F. Hartmann. *Evolution of Silicon Sensor Technology in Particle Physics*. 2nd ed. Springer, 2017. ISBN: 978-3-319-64434-9. DOI: 10.1007/978-3-319-64436-3.

[HM06] W. Herr and B. Muratori. *Concept of luminosity*. 2006. URL: https://cds.cern.ch/record/941318 (visited on 08/02/2018).

[Hut04] D.V. Hutton. *Fundamentals of Finite Element Analysis*. McGraw-Hill series in mechanical engineering. McGraw-Hill, 2004. URL: https://books.google.de/books?id=QEDDjwEACAAJ.

[LR12] C. Leroy and P.-G. Rancoita, eds. *Principles of radiation interaction in matter and detection*. 3. ed. New Jersey: World Scientific, 2012. ISBN: 978-981-4360-51-7; 981-4360-51-1.

[Mob16] E. Mobs. *The CERN accelerator complex. Complexe des accélérateurs du CERN*. 2016. URL: https://cds.cern.ch/record/2197559 (visited on 08/02/2018).

[Pra17] C. Pralavorio. *Record luminosity: well done LHC*. 2017. URL: http://cds.cern.ch/record/2295027 (visited on 08/02/2018).

[She] Shenzhen Andonstar tech Co. *Digital Microscope A1*. URL: http://www.andonstar.com/e_products/digital-microscope-V1-1.html (visited on 08/02/2018).

[Tan+18] M Tanabashi et al. *Review of Particle Physics*. In: Phys. Rev. D 98 (2018), p. 030001.

[Tay11] L. Taylor. *CMS detector design*. Nov. 23, 2011. URL: http://cms.web.cern.ch/news/cms-detector-design (visited on 08/02/2018).

[Vor15] B. Vormwald. *The CMS inner tracker - transition from LHC Run I to Run II and first experience of Run II*. In: PoS EPS-HEP2015 (2015).

Appendix

A. Appendix to Chapter 4: 2S Module Readout Station

A.1. Handling Procedure for Functional Tests of 2S Modules

In order to test a 2S module with the functional test station, the following steps have to be performed:

1. Every time before opening the aluminum box, it has to be checked that the temperatures on the two cooling stages are higher than the dew point of the air in the laboratory in order to prevent condensation of water on or near the module. This can be done via the MoReCooling framework. If the temperatures inside the box are lower than the dew point in the laboratory, please follow step 9 before continuing with the next step.

2. In order to mount a 2S module in the station, the rotatable aluminum frame has to be opened and the module, mounted on a module carrier, can be placed carefully on the two cooling jigs. There is only one possible orientation to place the carrier on the cooling jigs as there are screws protruding from the bottom side of the carrier.

3. The electrical connections have to be installed carefully before fixing the module on the jigs by closing and locking the aluminum frame.

4. After closing the aluminum box, the station is flushed with dried air by opening the remotely controllable valve. This can be done manually by pushing a provided button on an *Arduino Uno* or via the MoReCooling framework until the dew point inside the aluminum box has reached values below $-40°C$. After closing the remotely controllable valve, only a small flux of dried air continues to enter the box in order to compensate for air losses through openings in the box.

5. To prepare the functional tests of 2S modules under temperature stabilized conditions, the three valves controlling the coolant circuit have to be changed manually. The labeling of the three valves is introduced in Figure A.1. To allow the coolant to enter the setup and operate the precooling, valves 1 and 2 have to be opened. As a next step, valve 3 can be closed.

6. When the precooling block has reached the set temperature of the coolant (usually approximately $-10°C$), the desired temperature level can be set using the MoReCooling framework. By enabling the output of the low voltage power supply, the

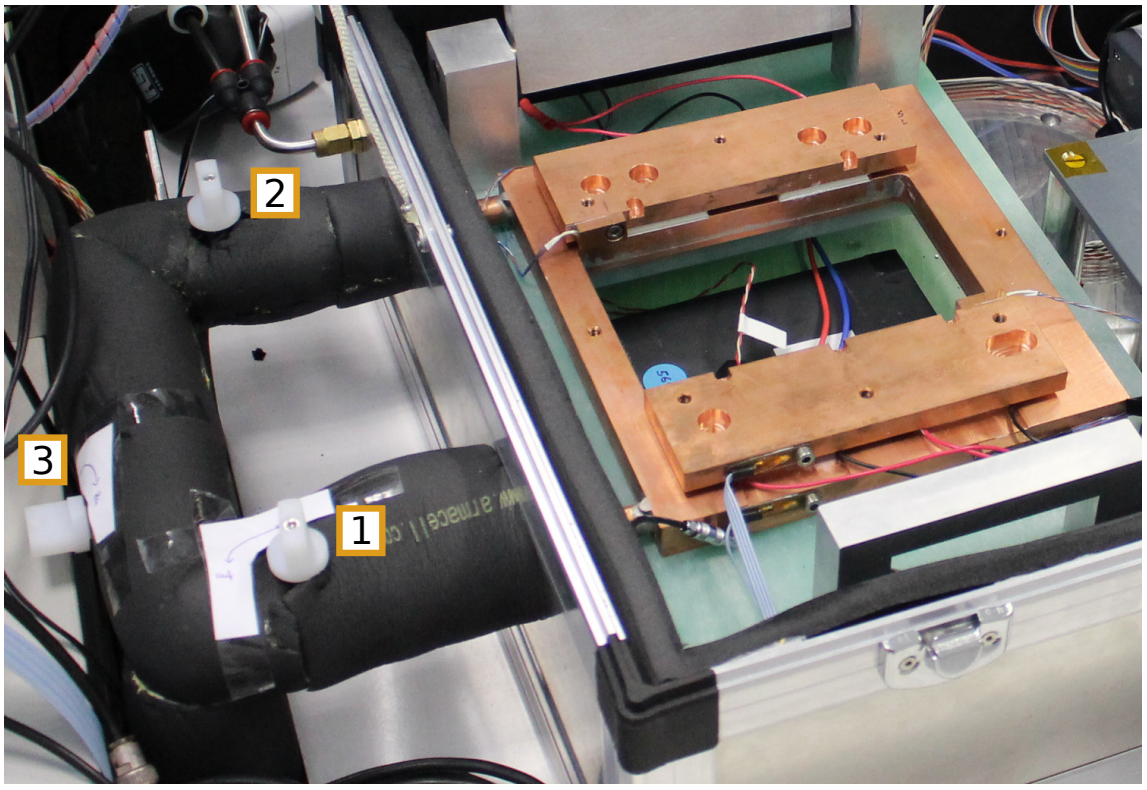

Figure A.1.: Labeling of the three manual valves to control the flux of the coolant in the precooling circuit. By opening valve 1 and 2, the coolant is able to enter the aluminum box and flow through the precooling block. Valve 3 allows to bypass the cooling circuit outside of the aluminum box.

Peltier devices are controlled by the PID algorithm in order to reach the desired temperatures.

7. When the functional tests are finished, the station has to be prepared for opening the lid. To accelerate the heating procedure of the two cooling stages, the cooling jigs are warmed up with the PID controller to approximately 30°C before the voltage output of the low power supply is disabled via the MoReCooling framework.

8. As a next step, the coolant bypass is opened by opening valve 3. Afterwards, valves 2 and 1 can be closed to prevent the coolant from entering the setup.

9. By opening the remotely controllable dried air valve, the aluminum box is flushed with dried air, which accelerates the heating up of the precooling stage to temperatures above the dew point in the laboratory. When the temperatures of both cooling stages are above the dew point in the laboratory, the aluminum box can be opened.

10. After opening the rotatable aluminum frame and disconnecting the electrical connections, the 2S module can be dismounted from the station.

A.2. Thermal Simulations of the 2S Module Functional Test Station

A.2.1. Simulations of the Cooling Jigs

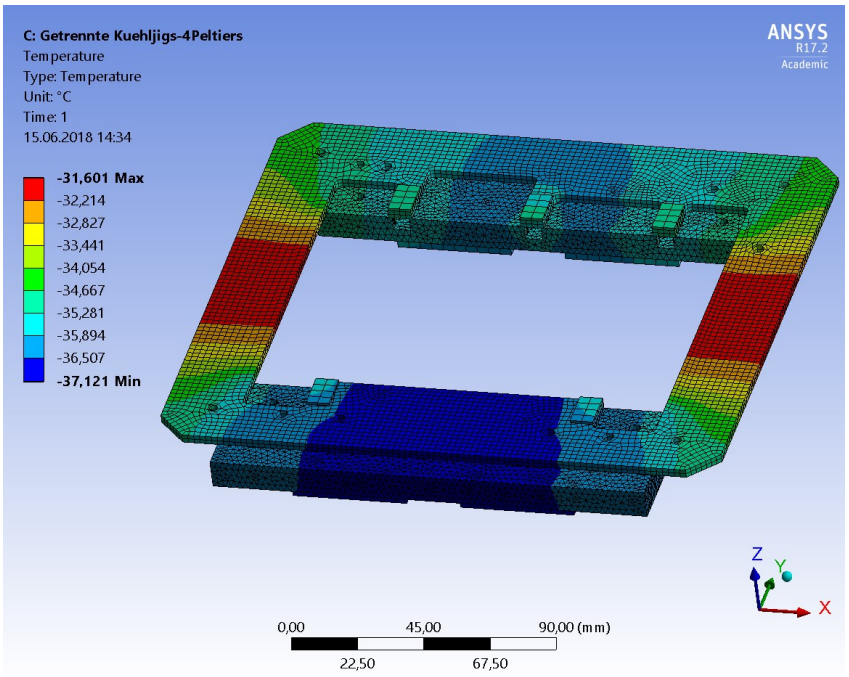

Figure A.2.: Simulated temperature distribution for the geometry with four Peltier devices below the two copper cooling jigs. In order to reach an average temperature of −35°C on the five module mounting points, each Peltier device has to provide a thermal power of approximately 9 W.

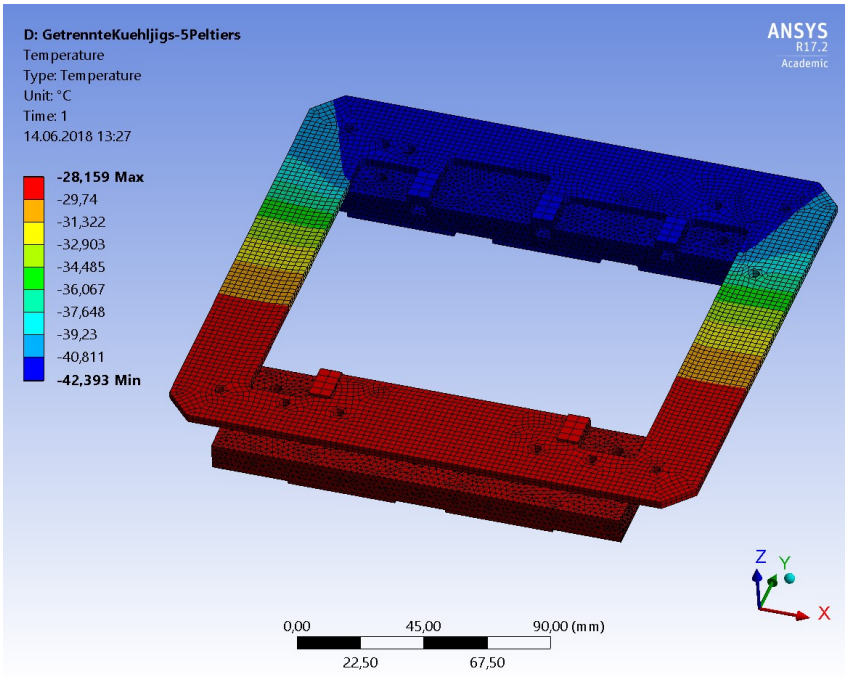

Figure A.3.: Simulated temperature distribution for the geometry with five Peltier devices below the two copper cooling jigs. In order to reach an average temperature of −35°C on the five module mounting points, each Peltier device has to provide a thermal power of approximately 7 W.

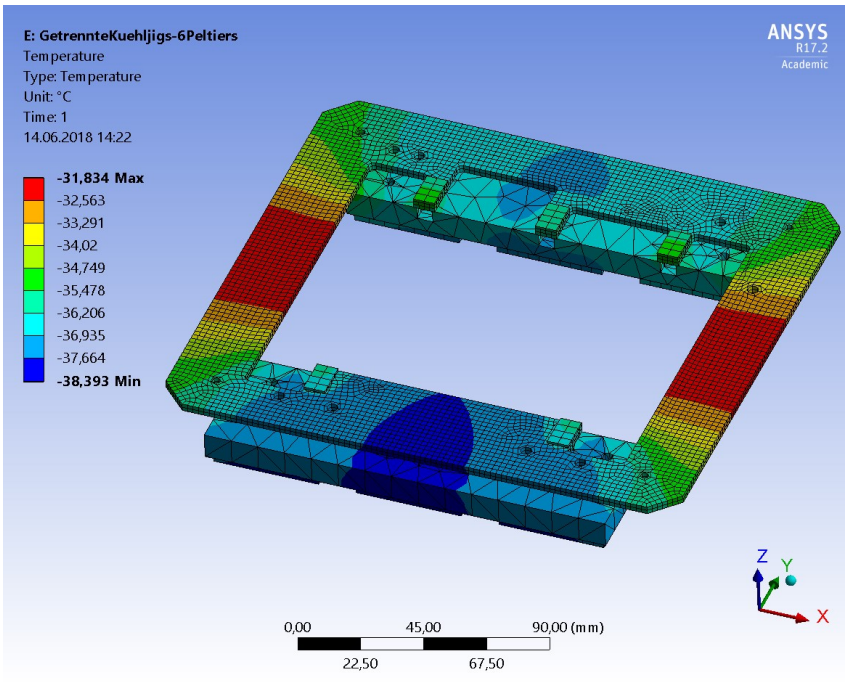

Figure A.4.: Simulated temperature distribution for the geometry with six Peltier devices below the two copper cooling jigs. In order to reach an average temperature of $-35°C$ on the five module mounting points, each Peltier device has to provide a thermal power of approximately 6 W.

A.2.2. Simulations of the Precooling

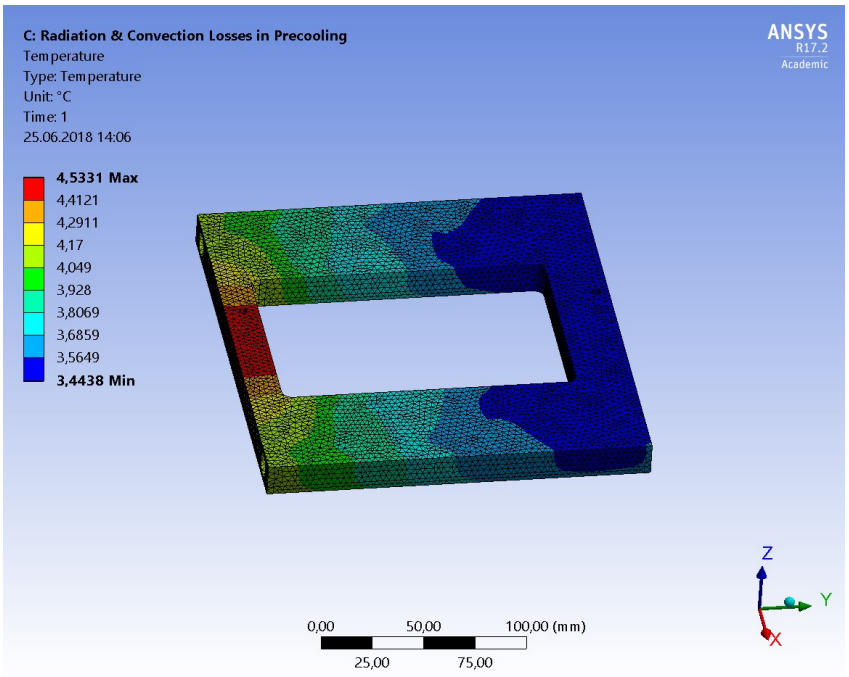

Figure A.5.: Simulated temperature distribution on the precooling copper block for a heat removal of 18.8 W at the top side of the cooling pipe. At all external surfaces, radiative and convective processes are simulated, the environmental temperature is set to 22°C. The average temperature is approximately 4°C.

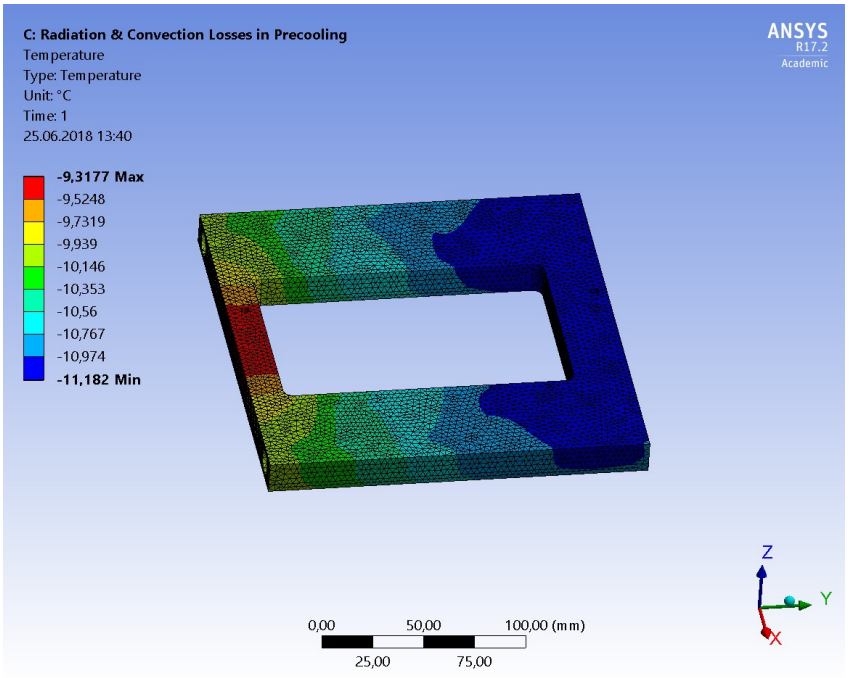

Figure A.6.: Simulated temperature distribution on the precooling copper block for a heat removal of 32 W at the top side of the cooling pipe. At all external surfaces, radiative and convective processes are simulated, the environmental temperature is set to 22°C. The average temperature is approximately −10°C.

A.3. Datasheet Peltier Device *TEC1-12705*

[Eve]

愉進電子科技有限公司
EVERREDTRONICS LIMITED
上海市宝山区菊联路 89 号 201907
No 89 Julian Road, Baoshan, Shanghai 201907 China.
Tel:+86-21-6049 5160 Fax:+86-21-6531 1544
URL: www.everredtronics.com E-mail: sales@everredtronics.com

SPECIFICATIONS

Thermoelectric Module: TEC1-12705T125

1. Dimensions

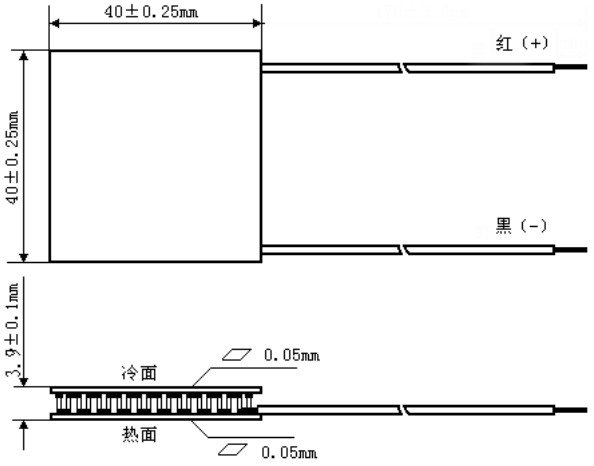

2. **Electrical Parameters**

Specifications		**Conditions**
I_{max}	5.0A	Th=30℃
V_{max}	15.0V	Th=30℃
ΔT_{max}	≥67℃	Qc=0, Th=30℃
Q_{cmax}	42.5W	ΔT=0℃, Th=30℃
T_R	-50~100℃	
Wire	20AWG, Length: 150mm	

愉進電子科技有限公司
EVERREDTRONICS LIMITED
上海市宝山区菊联路 89 号 201907
No 89 Julian Road, Baoshan, Shanghai 201907 China.
Tel:+86-21-6049 5160 Fax:+86-21-6531 1544
URL: www.everredtronics.com E-mail: sales@everredtronics.com

3. Performance Curves

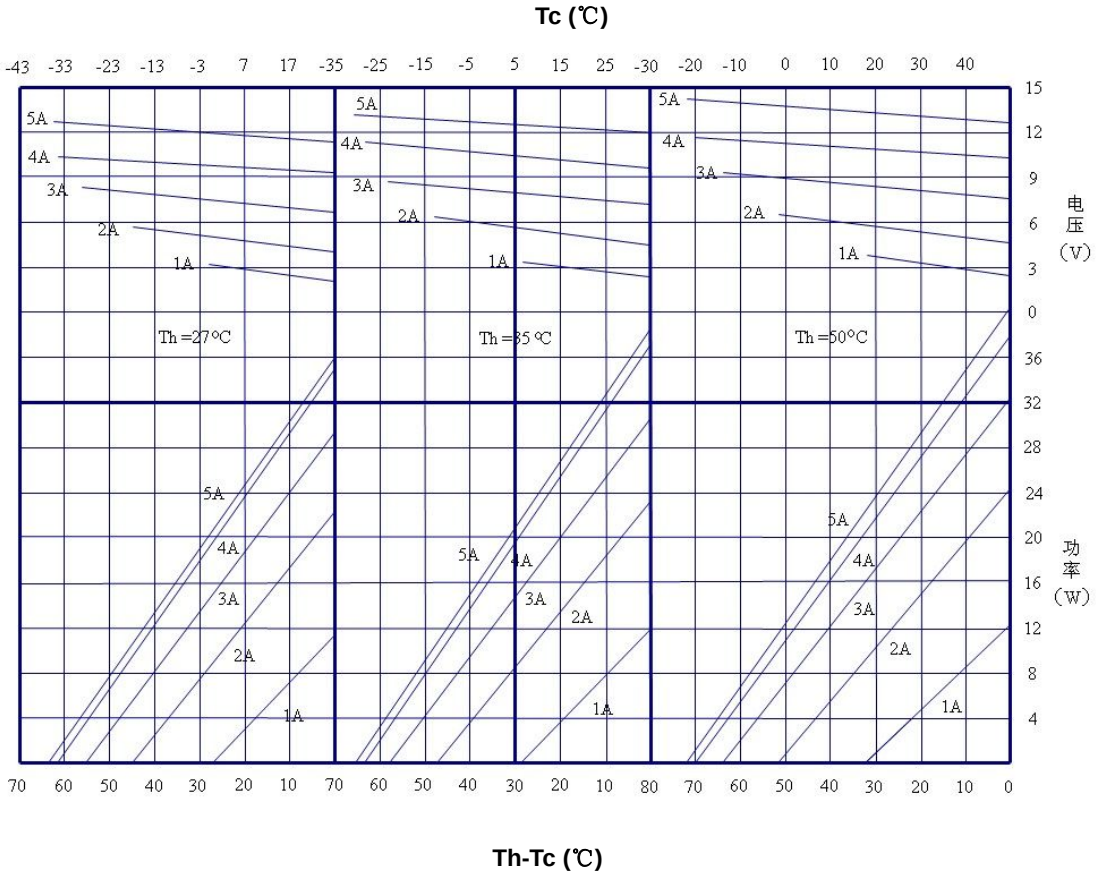

A.4. Datasheet Fryka ULK 2002

[Fry]

FRYKA

CIRCULATING COOLER ULK

ULK 1002:
modern generation of circulating coolers
for professional applications

The ULK circulating cooler serves as a universal cooler for the entire laboratory and industry and is an interesting and economical alternative to tap water cooling.
The unit is characterized by its flexible use in various applications.
On the one hand the 9,5 litre coolant tank can provide high temperature stability or can operate as a cold reservoir to help cushion cooling demand peaks. On the other hand, by minimally filling the device you have a very dynamic system with short cooling times which can quickly react to your cooling demands.

Due in particular to its compact space-saving design with a low-noise cooling unit, the circulating cooler is suitable for direct use in the workplace.

Model	ULK 1002	ULK 2002
Temperature range [min/max]	-10°C / +40°C	-10°C / +40°C
Control accuracy	+/- 0,5 K	+/- 0,5 K
Cooling capacity [at +20°C]	1200 W	2300 W
[at +10°C]	850 W	1600 W
[at -10°C]	400 W	750 W
Pump capacity flow rate	12 l/min	12 l/min
Pump capacity flow pressure	2,9 bar	2,9 bar
External dimensions WxDxH	35x44,5x66cm	35x44,5x94cm
Weight	41 kg	65 kg
Ambient temperature [min/max]	+12°C / +30°C	+12°C / +30°C
Electrical connection	230V / 50 Hz	230V / 50Hz
Current [max.]	3,5 A	8,0 A
Coolant tank	2,0 to 9,5 l	2,0 to 9,5 l

Characteristics:

- **energy-efficient:**
  - fan with EC technology
- **low noise level:**
  - particularly quiet components
  - fan adjusts its speed to the required value
- **user-friendly:**
  - integrated funnel
  - self-sealing hose connector with quick coupling
  - drain cock
- **high-quality components:**
  - touchscreen controller with high-grade glass screen and integrated flow and digital fill level indicators
  - components from renowned manufacturers
  - refrigeration unit: fully hermetically sealed, air-cooled, low maintenance
- **high operational reliability:**
  - freeze-up and thermal overload protection
  - flow control with dry running protection
  - optical and acoustical alarm
  - error messages are displayed in plain text
- **proven standard:**
  - MOD bus interface

Options:

- Operation with natural coolants
- Heating for extended temperature range
- Portable version
- Potential-free alarm contact with connection to an external alarm system
- Voltage input for externally setting the set point
- Voltage output for reading the actual value
- Interface converter/gateway from RS485 to USB or Ethernet
- Optional direct measurement of the application's temperature with an external gauge; by subsequently setting the set point, greater temperature stability can be achieved than with a standard system

FRYKA-Kältetechnik GmbH
Ohmstraße 4 | D-73730 Esslingen
Fon: +49 (0)711 310599- 0
Fax: +49 (0)711 310599-29
E-Mail: info@fryka.de
Web: www.fryka.de

A.5. Test Setup in Aluminum Box

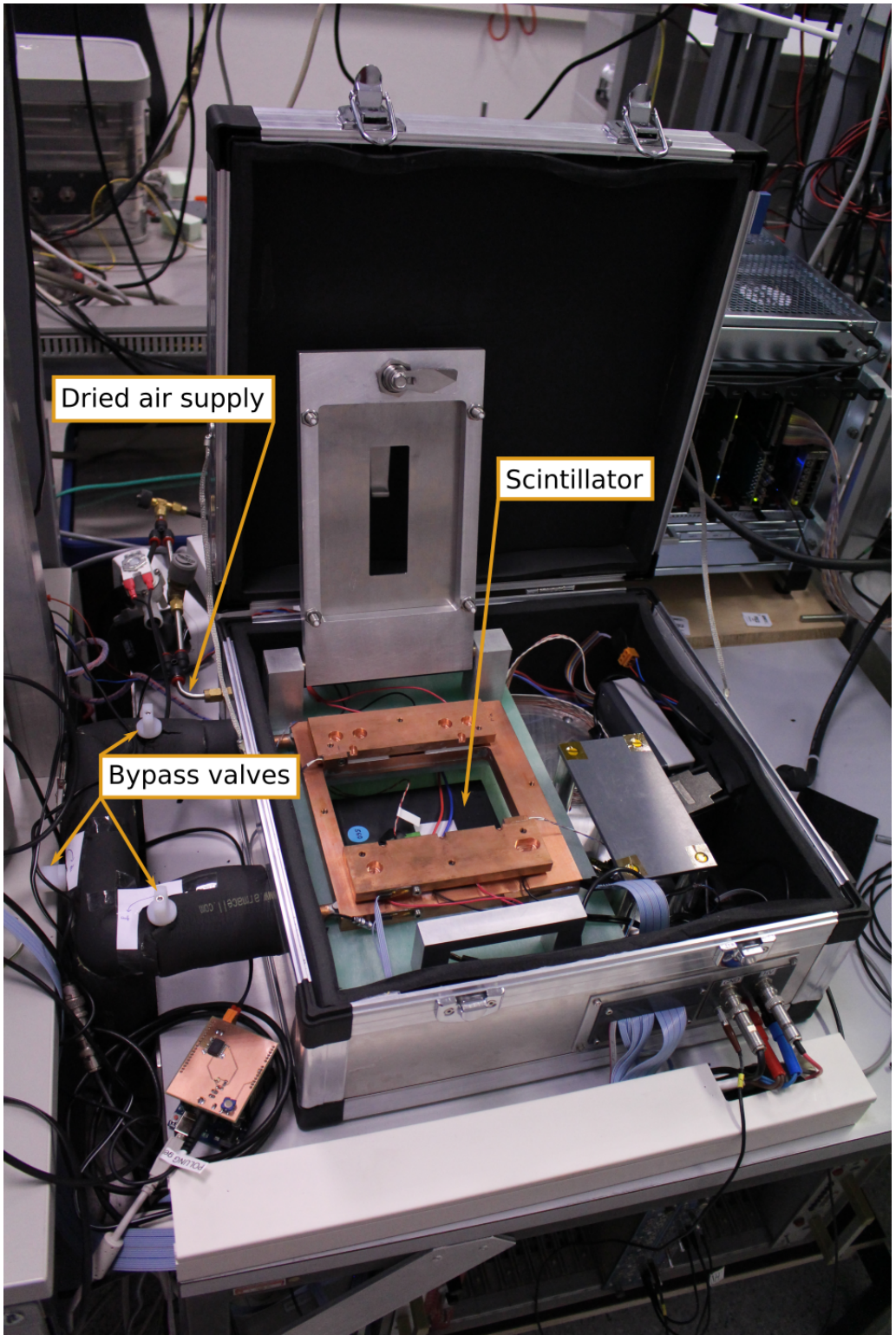

Figure A.7.: Experimental setup of the 2S module readout station inside the aluminum box. Below the two cooling stages, a scintillator with an area of $15 \times 15\,\mathrm{cm}^2$ is installed to perform detection efficiency studies. The box is continuously flushed with a small flux of dried air which can be enlarged by opening a remotely controllable valve. The cooling circuit can be closed outside the aluminum box by opening a bypass using three manually controllable valves.

B. Appendix to Chapter 5: Sensor Long-Term Station

B.1. Sensor Rack

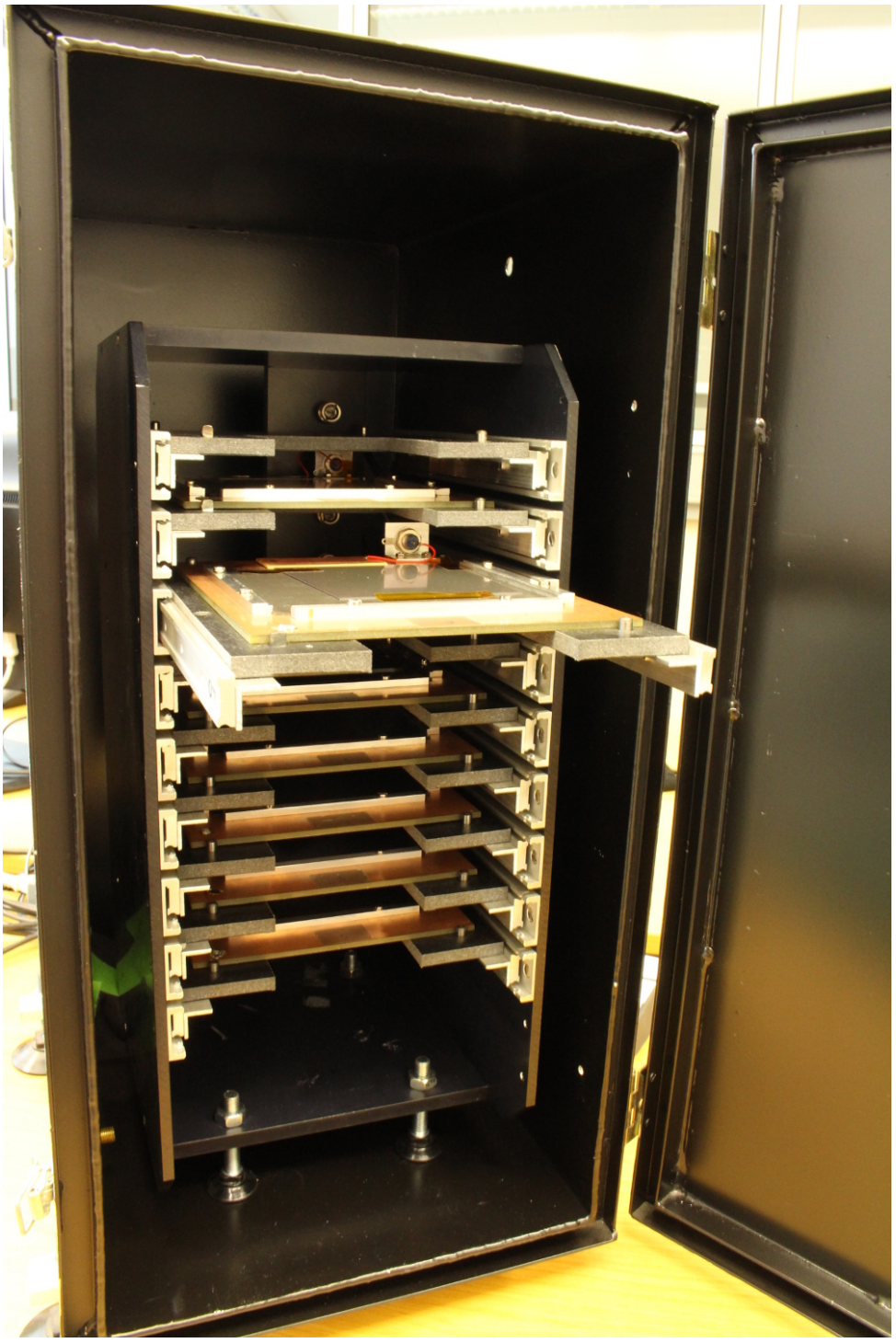

Figure B.1.: Sensor rack used in the sensor long-term station with ten telescopically mounted layers onto which the copper plates with the silicon sensors can be mounted. The rack provides a set of sockets at its back side which corresponds to the plugs on the sensors' copper plates. By sliding each layer into the rack, the plugs are connected with the corresponding sockets and the bias voltage and ground connection are applied to the sensors.

B.2. Electronic Circuit Board

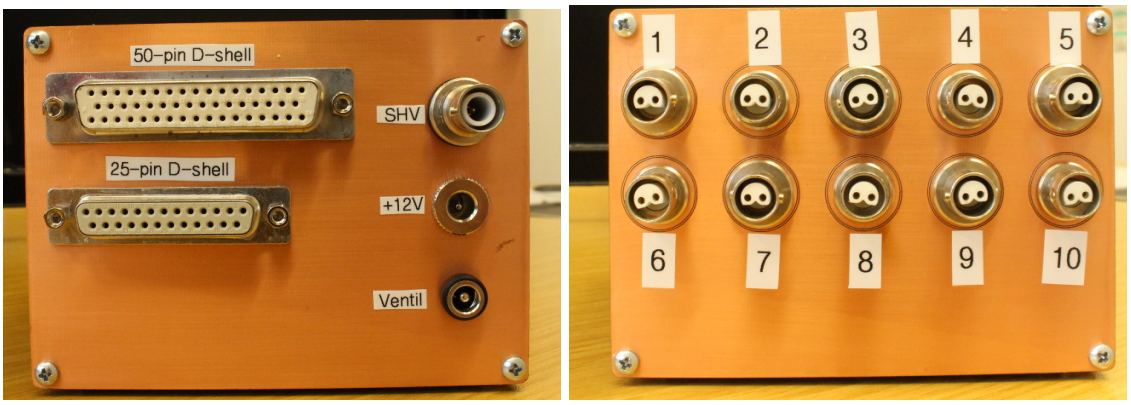

(a) (b)

Figure B.2.: Front (a) and back (b) of the electronic circuit board developed for the sensor long-term station with the connectors for digital output channels (50-pin D-shell), analog channels (25-pin D-shell), high and low voltage, the digital channel to control the status of the dried air valve ("Ventil") and the ten high voltage output lines to be connected to the ten sensors in the sensor rack.

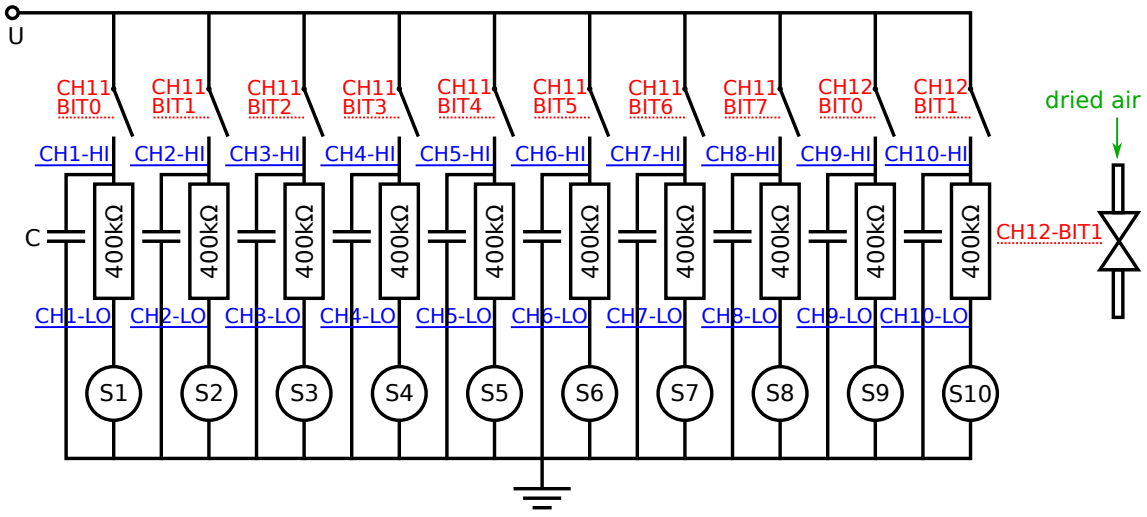

Figure B.3.: Schematic of an extended electronic circuit to operate the sensor long-term station. The additional capacitors allow disconnecting each sensor from the bias voltage without any need for a global voltage ramp down. After opening the corresponding shutter, the capacitor discharges via the resistor and sensor and, thus, the bias voltage is automatically ramped down.

B.3. Software Framework

Table B.1.: Name and description of scan parameters used in the command line-based software framework to control long-term measurements. These parameters are defined in a configuration file, which is loaded at the beginning of each measurement.

Name	Description	Default Values
keithley2700	Address of serial port to Keithley 2700 multimeter	/dev/ttyUSB0
isegt2dp	Address of serial port to Iseg high voltage power supply	/dev/ttyUSB1
limleakcurr	Upper limit for the leakage current in nA	1000
sensorlabelX	Sensor identification for sensor mounted on copper plate X	SX
voltchannel	High voltage channel of Iseg power supply	2
dcvoltage	Bias voltage for the sensors in V	300
polarity	Bias voltage polarity for the sensors	+
scanchannels	List of analog measurement channels	101:110
voltagerange	Voltage range of multimeter Options: 0.1, 1, 10, 100, 1000 or auto	auto
tbm	Time between two consecutive measurements of the leakage current in seconds	60
writeeachtrigger	Rate of writing results to a file	5
maxtime	Total measurement time in hours	72
voltageramp	Maximum voltage step to be changed each second during voltage ramps in V	10
humlevel	Relative humidity level to be stabilized in %	20
mntpath	Path to mounting point of 1-wire sensor	/dev/1-wire/honeywell

B.4. Humidity Stabilisation

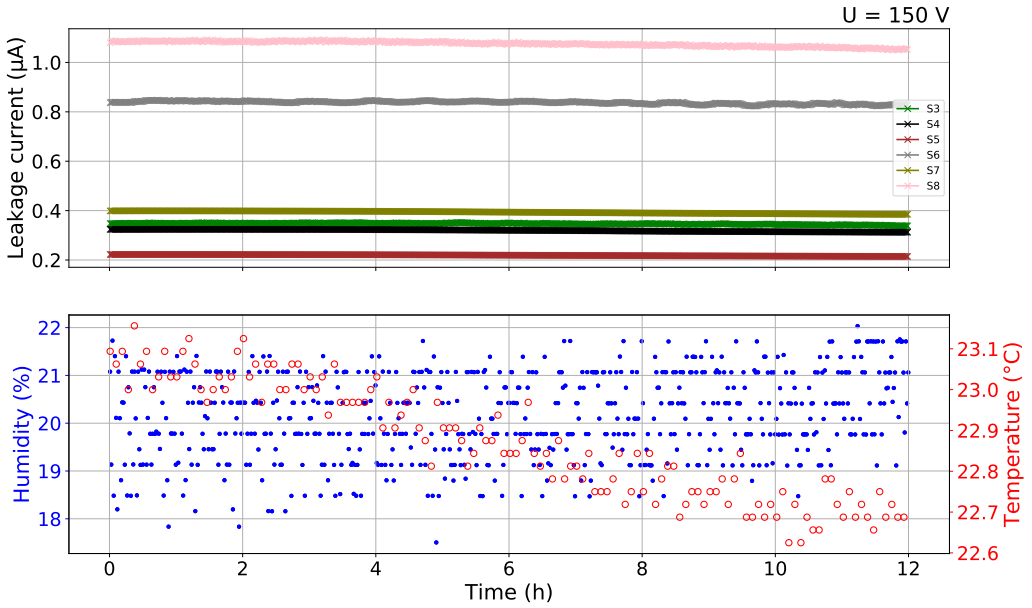

Figure B.4.: Long-term behavior of the leakage current of six silicon strip sensors in comparison with the temperature and relative humidity levels inside the sensor long-term station. The relative humidity level inside the aluminum box surrounding the sensor long-term station can be stabilized within a range of ±2% around a configurable level (for this measurement 20%) by opening and closing a remotely controllable valve allowing dried air to enter the setup. Thus, humidity induced leakage current changes are minimized during each long-term measurement.

B.5. Sensor Biasing via Needles

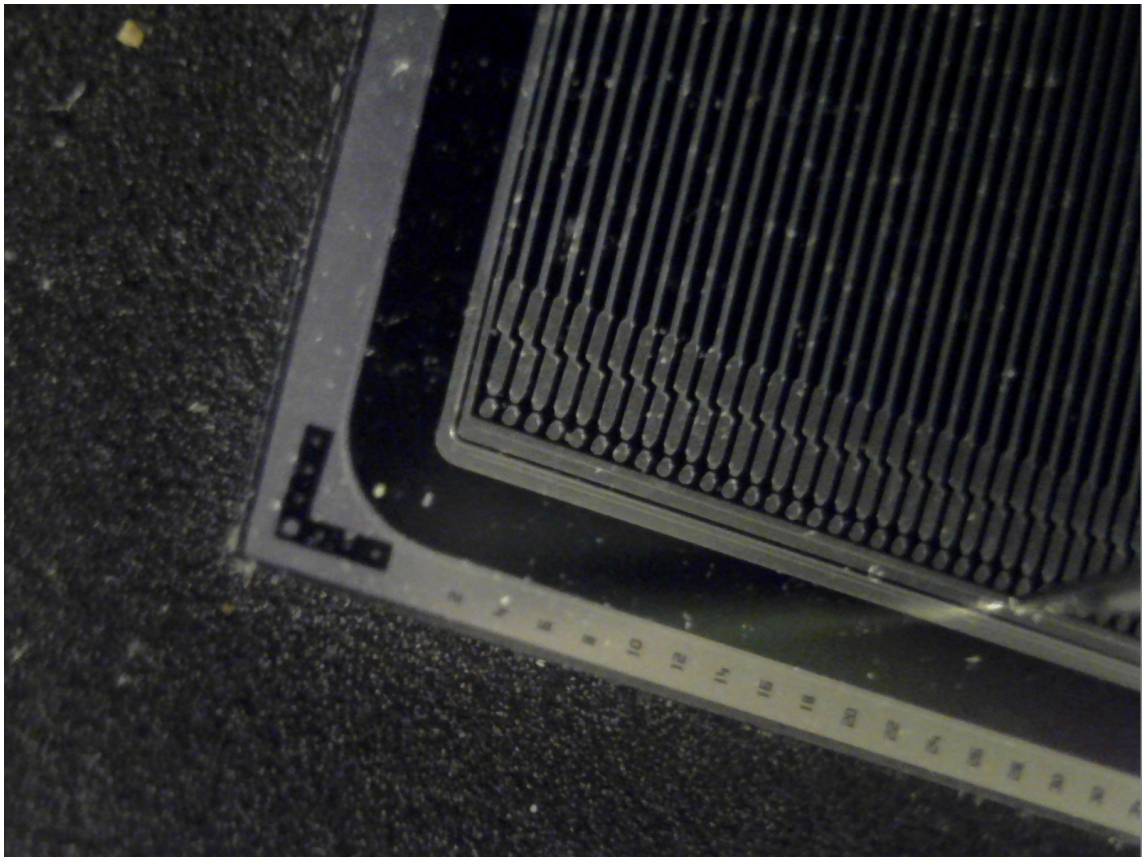

Figure B.5.: View of the USB microscope used to position a bias needle above the sensor's bias rail. By observing the needle tip and its reflection on the silicon surface, it is possible to lower the needle precisely onto the bias rail.

B.6. Datasheet USB Microscope

[She]

Product name : **Digital Microscope A1**

Technical Specifications

Diameter	12mm
Image sensor	High-quality COMS senor,2M pixel(hardware,No Interpolation)
Magnification	1-500 times
Video format	AVI
Photo format	JPEG or BMP
Focus range	Manual focus from 5mm-30mm
Frame rate	30 frames/sec(when resulation at,640×480),1600×1200 5 frames/sec
PC interface	USB 2.0
Operation system	Windows XP/7/8/10
Stand size	15*8*12cm
Light source	8 LED (adjustable by control wheel)
USB cable length	About 165 cm
Certification	CE/FCC/ROHS
Term	FOB Shenzhen
Package contents	microscope×1 Metal stand×1 reflector×1 balck specula×1 transparent×1 transparent speculm×1 Multi-function tube×1
Packaging data	17*11*5cm/410g
Warranty	1 year

1. DSP: High power Digital Image Monarch Processor.
2. Sensor: high-quality CMOS sensor, **2M pixel**(hardware,no Interpolation)
3. Resolution: 640X480,1600 X 1200 (set resolution: menu---options--video capture pin...)
4. Interface: USB1.1/USB2.0.
5. Frame rate: 30 frames/sec (When resolution at 640 X 480),1600 X 1200 5frames /sec
6. Focal distance: 5mm - 30mm (when Focal distance infinity,the microscope as a webcam,can not magnify).
7. Magnification: Please refer to the sample photos and video
8. Diameter: 12mm
9.USB cable Length:about 165cm USB cable color:black or transparent color (random)
10.Lighting:8 X LED around the camera lens

Price 2017: ~ 60 €

Danksagung

Abschließend möchte ich mich bei allen bedanken, die maßgeblich zum Gelingen dieser Arbeit beigetragen haben.

Herrn Prof. Dr. Ulrich Husemann danke ich dafür, dass er mir die Erstellung meiner Abschlussarbeit in seiner Arbeitsgruppe ermöglicht hat und für seine Unterstützung in Rat und Tat während der Umsetzung. Herrn Prof. Dr. Thomas Müller danke ich für seine Bereitschaft, Korreferent dieser Arbeit zu sein.

Bei Herrn Dr. Alexander Dierlamm bedanke ich mich für seine ausgezeichnete Betreuung, die interessanten und gewinnbringenden Diskussionen über die Realisierung meiner Arbeit, sowie die zügigen Verbesserungsvorschläge beim Korrekturlesen.

Ein besonderer Dank gilt Herrn Stefan Maier für seine hervorragende Unterstützung in allen Belangen. Von seinen Kenntnissen in fachlichen und technischen Fragen, sowie von seinen zielgerichteten Verbesserungsvorschläge habe ich außerordentlich profitiert.

Herr Tobias Barvich hat durch seine ausgezeichnete und geduldige Unterstützung in technischen Fragen großen Anteil an der Umsetzung dieser Arbeit, wofür ich ihm herzlich danke. Für seine Hilfe beim Zusammenbau der Stationen bedanke ich mich bei Herrn Marius Neufeld. Frau Pia Steck, Frau Anita Weddingen und Herrn Felix Bögelspacher danke ich für die stets zügige und ausgezeichnete Umsetzung von elektrotechnischen Aufgaben.

Ich danke der Studienstiftung des Deutschen Volkes für ihre Unterstützung während meines Studiums, insbesondere für die Möglichkeit zur Teilnahme an einer Vielzahl an Exkursionen und Akademien.

Meiner Familie und ganz besonders meinen Eltern Ulrike und Wolfgang Koppenhöfer danke ich für ihre liebevolle Unterstützung während meiner gesamten Ausbildung.

Abschließend möchte ich der gesamten CMS-Hardware-Abteilung am Institut für Experimentelle Teilchenphysik für die angenehme Arbeitsatmosphäre und interessanten (auch außerfachlichen) Diskussionen danken.